Summer 6-2-2017

Evaluation of Concrete Constitutive Models for Impact Simulations

Guillermo A. Mata

Guillermo A. Mata

Candidate

Mechanical Engineering

Department

This thesis is approved, and it is acceptable in quality and form for publication:

Approved by the Thesis Committee:

Dr. Tariq Khraishi, Chairperson

Dr. Scott E. Sanborn

Dr. Yu-lin Shen

Evaluation of Concrete Constitutive Models for Impact Simulations

BY

GUILLERMO ADRIAN MATA

B.S., Mechanical Engineering
University of New Mexico, 2015

THESIS

Submitted in Partial Fulfillment of the
Requirements for the Degree of

Master of Science

Mechanical Engineering

The University of New Mexico
Albuquerque, New Mexico

July, 2017

ACKNOWLEDGEMENTS

This work would not have been possible without the available resources provided to me by the Nuclear Regulatory Commission and Sandia National Laboratories. I am extremely grateful to my Sandian advisors for providing me the mentorship, guidance, and experimental data needed to complete my research. I would also like to express my sincere gratitude to my University of New Mexico advisor, Dr. Tariq Khraishi who has managed to teach, advise, and mentor me through most of my years as an undergraduate student and my time as a graduate student. A special thanks is in order to all the professors at the University of New Mexico who helped me get to where I am today.

Evaluation of Concrete Constitutive Models for Impact Simulations

by

Guillermo Adrian Mata

B.S., Mechanical Engineering, University of New Mexico, 2015

M.S., Mechanical Engineering, University of New Mexico, 2017

ABSTRACT

The research documented in this thesis deals with computational analysis of reinforced concrete impacted by both hollow and solid missiles as a continuing effort on the work conducted by the Committee on the Safety of Nuclear Installations (CSNI) and Nuclear Energy Agency (NEA). The analysis focuses on comparing two similar material models and their ability to capture the mechanistic response of a reinforced concrete slab subjected to impact loads. The analysis was performed using the Sandia National Laboratories computing software SIERRA Solid Mechanics to run the finite element model. The two constitutive models studied were the Holmquist-Johnson-Cook and Johnson-Holmquist 2 material models. The two material models were run with identical meshes, element types, and boundary conditions and their results were compared to the experimental test data gathered by the CSNI. Both material models proved to be successful in capturing the global flexural response of the reinforced concrete target impacted. However, the fractured damage pattern produced by both material models in the two simulations (hollow/solid) proved that some degree of uncertainty was present in the modeling approach and the material model itself.

TABLE OF CONTENTS

LIST OF FIGURES

LIST OF TABLES

CHAPTER 1

INTRODUCTION

1.1 Background

Modern day structures are constructed with strict guidelines ensured by standardized codes to meet a variety of requirements. The American Concrete Institute (ACI) 318 is a prime example as it outlines building codes that are implemented on concrete structures (ACI 318 Committee, 2014). While many global standards will account for natural occurring events such as earthquakes, which produce seismic behavior that requires alternative design requirements, design requirements for ballistic events on reinforced concrete (RC) aren't typically considered with the exception of ACI 349 (ACI 349 Committee, 2001). For the past three decades, a growing interest has been shown on the fractural behavior of RC subjected to impact loads.

Accidents that subject RC structures to ballistic events can and have occurred with catastrophic results. Debris from an aviation accident can cause severe damage to RC structures by invoking a strong dynamic response, at the moment of impact, that produces global damage to the structure and localized damage at the site of impact (Riedel et al., 2010). This can also occur during natural disasters where high velocity winds can propel moderately heavy objects towards a structure at high speeds (Stephenson et al., 1978). For these reasons and more, efforts have been made to analyze the damage that high velocity projectiles can produce on a RC structure (Sanji, 2011). In 2010, the Nuclear Energy Agency (NEA) and the Committee on the Safety of Nuclear Installations (CSNI) proposed

a round robin challenge problem to study modeling approaches for reinforced concrete impacted by missiles and gathered a group of analysts from 20 different institutions to work on Improving Robustness assessment of structures Impacted by missiles (IRIS).

When studying the behavior of RC structures under large dynamic loads, it is impractical to conduct a series of large scale experiments because the associated costs are so high in some cases. Finite Element Modeling (FEM) is one method that is commonly used to capture the phenomena related to high velocity projectile impacts on RC structures. As with all numerical simulations, a fundamental understanding of both the physical reality and computational mechanics is required in order to obtain the correct material responses within a simulation. This becomes more evident when modeling RC because of the issues that arise from the composite behavior the complex nature of concrete and embedded steel rebar produce.

1.2 Problem Statement

Reinforced concrete is the most widely used construction material in the world. However, even though RC is one of the most common composites used to build structures, modelling impacts on RC structures has been proven to still be a difficult feat (Nordendale, 2013). In order to build more sophisticated simulations that can accurately capture the behavior of RC during impacting conditions, more studies need to be conducted to quantify the difficulties in modeling and the uncertainties generated from constitutive models to create and improve constitutive concrete models.

The primary objective of this study is to develop a comparison of different constitutive concrete models using the phase II IRIS project and the Johnson-Holmquist series material models, which has yet to be done (OECD-NEA, 2014). The comparison of

the two suitable material models for concrete will also be compared to the results of other constitutive concrete models that have been previously employed. While a number of experimental and numerical studies have been conducted that investigate the behavior of RC subjected to impact loads, there is still a need to further compare concrete models and analyze simulations at a spectrum that encompasses impact loads. These spectrums should include simulations that subject RC to low velocity projectiles that are deformable and higher velocity rigid projectiles that are more penalizing to a structure. This analysis includes two major simulations. The first simulation will look at the flexural response of a thin RC slab impacted by a hollow stainless steel missile, while the second simulation will involve a short steel-covered concrete missile to look at the damage profile produced on a thicker concrete slab. Both simulations are representative of the IRIS experiments conducted at the Valton Teknillinen Tutkimuskeskus (VTT) research facility in Finland.

1.3 Scope of Study

The goals and objectives of this study are to:

1. Conduct an investigation to determine the governing parameters that control the simulation.
2. Develop a Finite Element Model to accurately represent the phase II IRIS project with simplified boundary conditions and accurate material properties for the RC slab and projectiles used in the experiment.
3. Utilize SIERRA Solid Mechanics (SM) as the primary computational tool to run the numerical simulation.
4. Calibrate all material models for the materials they represent and thoroughly investigate the accuracy and precision of the different constitutive concrete model's

ability to represent the actual experiment for each simulation (VTT-Flexural and VTT-Punching).

1.4 Comparison of Results

In order to validate the results that are acquired from the numerical simulations, a two stage comparison is made. First, the results obtained from the simulation will be compared to the IRIS experimental results provided by the Institute for Radiological Protection and Nuclear Safety (IRSN). The results provided by IRSN include:

1. A uni-axial compression test and four tri-axial compression tests on cylindrical concrete specimens with confining pressures ranging from zero to 100 MPa.
2. A VTT-IRSN-Flexural test where a RC slab was impacted by a soft missile (hollow) at 110 m/s with data acquisition for:
    a. RC slab displacement at various locations.
    b. Concrete crack patterns.
    c. Rebar strain at various locations.
    d. Missile damage.
3. A VTT-IRSN-Punching test where a RC slab was impacted by a hard missile (concrete filled) at 136 m/s with data acquisition for:
    a. RC slab damage profile.
    b. Missile damage.

The second part of the comparison is done by evaluating the results obtained from the numerical simulation to the results obtained from other institutions involved with the IRIS program.

1.5 Thesis Overview

The research is organized into several chapters. Chapter 1 provides a brief background and preliminary introduction into the research tasks and needs of simulating impact loads onto RC structures. Chapter 2 includes the literature review which discusses the composite RC, theory on concrete impact, simulating concrete penetration, and constitutive concrete models. Chapter 3 introduces the test schematic for both VTT-IRSN experiments (Flexural and Punching), as well as the material data for materials used in the experiment (concrete, steel missile, steel rebar). Chapter 4 includes the Finite Element model constructed for each simulation along with boundary conditions, simplifying assumptions made, elements, and material models used. Chapter 5 compares the results obtained by implementing a two stage comparison of the numerical simulation results to test data and previous simulations conducted by other institutions using different constitutive concrete models, computational codes, boundary conditions, and meshes.

CHAPTER 2

LITERATURE REVIEW

2.1 Concrete

Concrete is a composite widely used across the world to form components to build structures. It is a conglomerate formed through the solidification of water, cement/lime, and coarse/fine aggregates (granite, slag, crushed stone, etc.) which makes up the majority of the mixture (Panasyuk et al., 2013). Depending on the type of filler (aggregates) used in the formation of concrete, different classifications can be given to the grade of concrete. When water is added to cement, the crystals of cement begin to hydrate and harden, which lock the aggregates tightly together (Bensted, 1983). Before concrete begins solidifying, it is easy to work with as it acts like a viscous fluid before hardening to a stiff solid with high compressive strength. This, along with the relatively low cost to acquire all the necessary and readily available constituents, is what makes concrete an ideal material to use in construction.

Concrete's material properties are dependent on a number of different variables. Some of the influencing factors include the type of cement and amount used: aggregate type and size, the strength of the aggregate in the mixture and surface condition, amount of water utilized during solidification, ageing time, aggregate roughness and adhesion to the cement mortar (Shishkin, 2001). Since concrete has such a unique structure and complexity to its mechanistic behavior, concrete is studied at the macroscopic, mesoscopic and microscopic levels (Wriggers-Hain, 2007). At the macroscopic level, concrete is considered homogenous and focus is solely aimed on the large scale phenomenon that is

observed in concrete. The mesoscopic level targets the mechanical properties typically associated with the random size and distribution of aggregates found in concrete structures (Wriggers-Moftah, 2006). The microscopic level generally deals with the crystal structure matrix and contact zone between binder and aggregate, also known as the interfacial transition zone. For impact load conditions that produce a pressure shock front, the meso/microscopic properties are not investigated. Since the dynamic response of an impact load will affect the entirety of the structure while producing localized damage at the point of impact, only the macroscopic behavior of concrete is typically studied when dealing with impact loads.

2.1.1 Concrete Material Properties

Although concrete is distinguishable by its microstructure heterogeneity, at the macroscopic level, an elastic homogenous continuum can be assumed, allowing material properties such as Young's modulus of elasticity (E), Posisson's Ratio (v), specific fracture energy (γ), and ultimate compressive/tensile strength (fc/ft) to be implemented in models. Through experimental testing, concrete can be subjected to mechanical testing to acquire the aforementioned material properties.

During compression testing, a specimen will encounter a uniaxial compression load that will begin to deform the specimen. The stress strain relationship for concrete under compression can be split into two categories, ascending branch (pre peak strength) and descending branch (post peak strength). During initial loading, concrete begins to deform elastically. As concrete approaches its peak compressive strength, the influence of viscous flow of unhardened cement paste and the increasing formation/propagation of micro cracks decreases the slope of stress-strain. Before compressive strength is reached, strain energy

is stored and micro cracks propagation speed up and link to initiate failure in the material (Gu et al., 2016). This phenomenon can be seen in Figure 2.1.

Figure 2.1: Stress-strain curve for concrete in compression

Once peak stress is achieved, development of cracks continue as well as the linking of preexisting cracks causing the prismatic specimen's capacity to carry a compressive load to progressively diminish. Concrete is exceptionally stronger in compression than in tension due to the tensile weakness of the cement material that holds the aggregates in place. While in compression, the interfacial transition zone transfers the compressive load from one aggregate to another, which does not require a lot of strength to accomplish (Wriggers-Moftah, 2006).

During tension, the interfacial transition zone no longer acts as just a medium to transfer loads from aggregate to aggregate, but also tries to hold the aggregates from separating in tension. For this reason, the tensile strength of concrete is heavily dependent on the cementitious material used and less dependent on the adhesion of the cementitious

material to the aggregates added in the concrete mixture (Alexander-Wardlaw, 1960). During tensile loading, concrete will not reproduce the crushing behavior that is generally observed during compression; consequently, the yield and tensile strength in concrete can be regarded as equivalent and occur at the onset of damage. Figure 2.2 depicts the stress strain response of concrete during tensile loading.

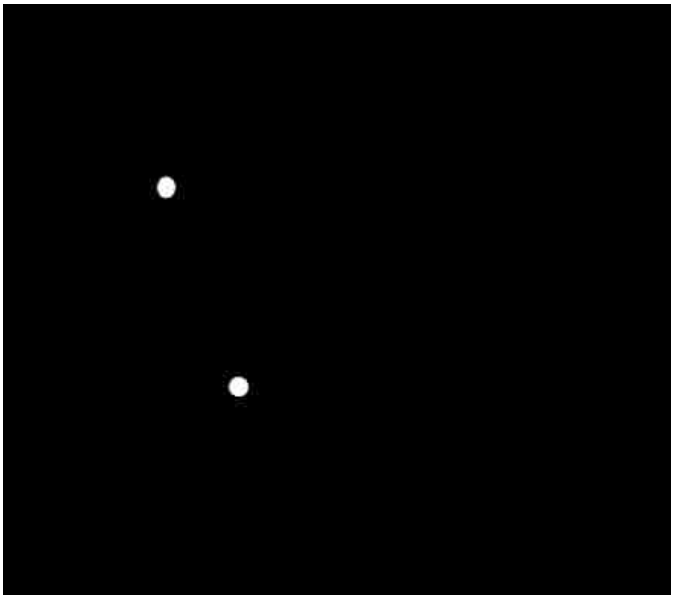

Figure 2.2: Stress-strain curve for concrete in tension

During Triaxial compression tests, a confining pressure is introduced onto a concrete prismatic specimen with a fluid, which allows the specimen to carry a higher axial compressive load. With the presence of a confining pressure, the formation of cracks and their propagation is mitigated because the lateral deformation of the concrete cylinder is suppressed by the confining pressure. Figure 2.3 shows how loads are applied on a triaxial test.

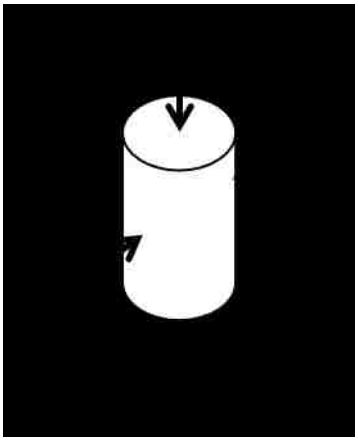

Figure 2.3: Triaxial compression loading

As shown in Figure 2.3, σ_2 and σ_3 are equivalent confining pressures that are regulated by a fluid that surrounds the prismatic concrete specimen. σ_1 is the axial compression load applied to the specimen. The concrete specimen's axial strength will increase and be more ductile when a confining fluid pressure is applied. The increase in amplitude is correlated to the confining fluid pressure applied. Figure 2.4 depicts the ascending trend of increasing axial strength and strain, ε_1, with increasing confinement.

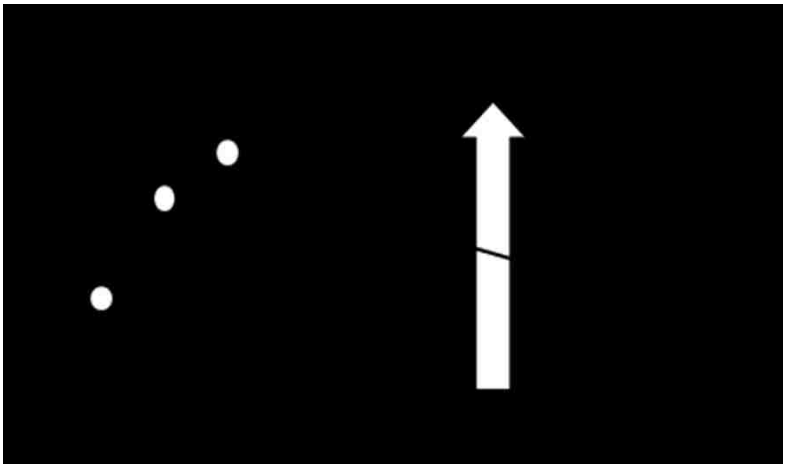

Figure 2.4: Strength to confinement relationship

The implementation of concrete confinement can typically be seen in concrete columns that are subjected to compression loads. These columns can have a dense arrangement of

circular hoops that help restrain the lateral deformation of internal concrete which provides confinement (Gu et al. 2016).

2.1.2 Reinforced Concrete

Unfortunately concrete has some major drawbacks since it is significantly weaker in tension and has very low ductility. This led to the development of reinforced concrete (RC), where wet concrete is cast around high tensile strength steel rebar in a matrix or lattice form to produce a new composite with a higher tensile load carrying capacity and greater ductility.

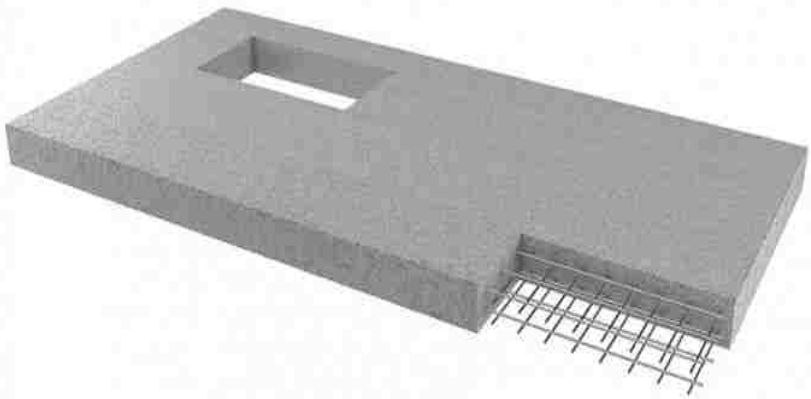

Figure 2.5: Reinforced concrete (Ancon, 2017)

RC can be typically classified as precast, cast in a reusable mold in a controlled environment to be later transported, or cast in-place where the concrete is cast at the construction site. The concrete in RC provides resistance to compression while the steel

rebar provides resistance to bending or stretching. The inclusion of steel helps to improve the tensile carrying capacity and ductility that would be lacking in a pure concrete structure. Steel and concrete also have a good thermal compatibility which mitigates unacceptable stresses from forming with changing temperature (Lamond, 2006). When concrete adheres to steel reinforcement, the cement paste conforms to the contours of steel, whether it is flat or grooved, acting as a protective layer against corrosion on steel in a passive state (Jones, 1996). The benefits derived from the new composite of concrete and steel make RC one the most important assets in constructing structures.

The required reinforcement for RC is proportional to the loadings that will be present during the structure's operational lifecycle. The classification of steel reinforcement can be categorized by the size of steel used, manufacturing process the steel undergoes (hot rolled/cold-drawn), surface relief which alters concrete adhesion (ribbed, dented, ledges), etc. Stiff reinforcement also exists to help form and bear the self-weight of structures and allow structural members to possess higher loading capacities. Stiff reinforcement refers to steels with shapes like steel I-beams, channel steel, and angle steel (Panasyuk et al., 2013). Although there are different versions of steel reinforcement, some of most common types found in structures are steel bars.

Like most materials, monotonic tensile testing is conducted on steel specimens in order to obtain experimental results for how steel bars behave under loads. The stress strain curve for low carbon alloys can be segmented into several different regions. The first being the ascending branch which is dominated by pure elastic deformation that is recoverable. The second region is denoted as the yield plateau or Luders strain (Gu et al., 2016). In this region, stress fluctuates near the yield stress, f_y, which corresponds to an area of

nonhomogeneous deformation. Following the plateau, another ascending segment is encountered with a less gradual nonlinear slope for stress which is related to the work hardening that is produced from uniform plastic deformation. The last region is denoted as the damaged region where necking occurs succeeding the ultimate strength of the alloy. For low carbon steel alloys such as mild steel, the hardening behavior is very minimal. A diagram of the stress strain curve can be seen in Figure 2.6.

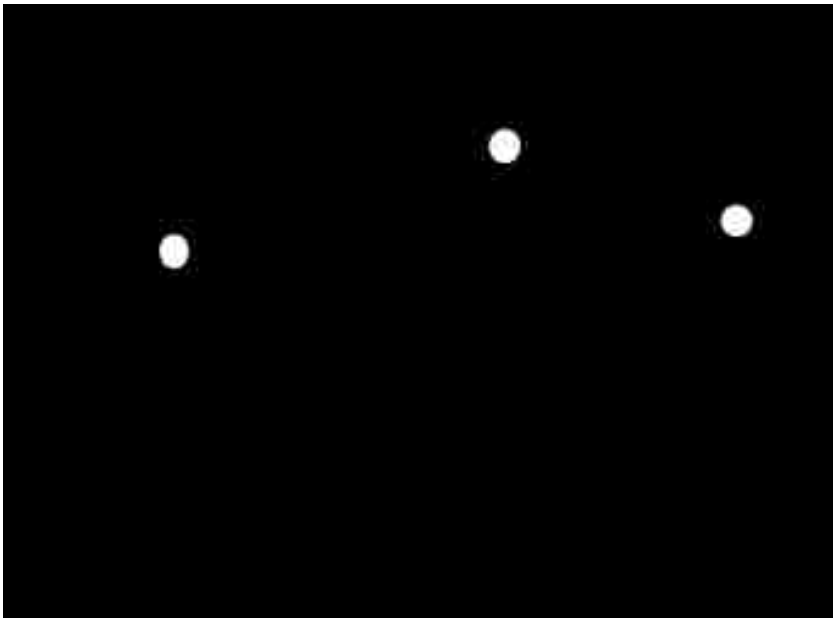

Figure 2.6: Stress-strain curve of low carbon alloy

2.2 Concrete Behavior under Impact Loads

The nature of cementitious materials under strong dynamic loads, that introduce high-rate loading conditions, are dependent on a variety of factors.

1. The materials involved in the experiment (high/low strength properties for concrete and reinforced concrete).

2. The concrete target geometry and its reinforcement ratio/location/orientation if reinforcement is included.
3. The structure designed to support and contain the system that will be subjected to impact loads.
4. The energy produced and transferred onto the concrete structure by the projectile is governed by the size, speed, mass and material characteristics (soft/deformable or hard/rigid) of the projectile used.

A matrix of the aforementioned variability factors ultimately yields a wide spectrum of damage on concrete targets. Since a growing interest from both the military and nuclear industry has developed over the decades to uncover the phenomenological response of concrete structures impacted by missiles, significant advancements have been made in experimental characterization of concrete.

2.2.1 Dynamic Response of Ballistic Impacts

For a projectile that impacts a solid target, a pressurized shock wave capable of treating a solid material as a compressible fluid in the early stages of impact, travels through the medium and propagates through the solid target (Zukas, 2004). The impulse loading response produced onto the structure is very complex. If a structure is stressed by a ballistic impact, it is important to quantify the material behavior being impacted before and after the propagating shockwave. William John Macquorn Rankine's and Pierre Henri Hugoniot's work paved the way for a set of conditions to be developed that describe the relationship of the state of a material on either side of a shock front (Salas, 2006). These conditions do not define specific properties of a material; rather, it describes the relation

between response variables across a shock front and how they change. The governing equations for the bodies involved are:

1. Conservation of mass
2. Conservation of momentum
3. Conservation of energy

These governing equations express the Rankine-Hugoniot conditions and can be depicted by Eqs. (2.1)-(2.3) (Nordendale, 2013).

$$\rho_1 u_s = \rho_2 (u_s - u_2) \tag{2.1}$$

$$p_2 - p_1 = \rho_2 u_2 (u_s - u_2) = \rho_1 u_s u_2 \tag{2.2}$$

$$\rho_2 u_2 = \rho_1 u_s (\frac{1}{2} u_2^2 + e_2 - e_1) \tag{2.3}$$

The application of a shock front can be described by a uniform pressure suddenly being applied to one end of a compressible continuum. The pressure produces a shock wave which propagates through the material with a speed u_s. As the shock wave travels through the material, it pressurizes the material in front of the wave to a new density ρ_2. While the traveling wave compresses the material located in front of the wave, it also begins to accelerate the material to a new velocity u_2. As the shock front continues to travel it will continue to compress and accelerate the material it passes through creating two distinct regions separated by the moving wave. The first region is denoted as the material the shock front has passed through while the second region is classified as the material that is currently being affected by the passing wave. Figure 2.7 is a visual representation of an

impact induced shockwave propagating through a medium which produces two regions separated by the shock front.

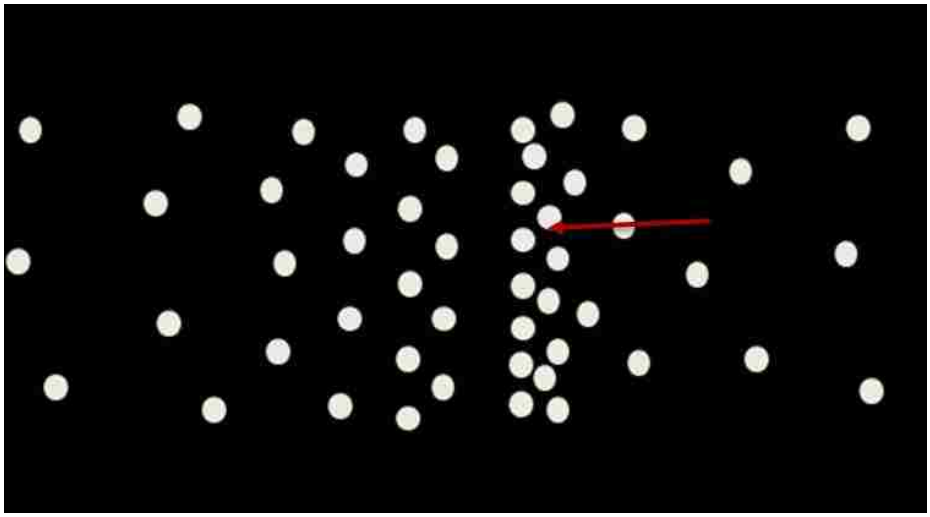

Figure 2.7: Propagating shockwave caused by ballistic impact

2.2.2 Localized Concrete Damage

Many researchers and engineers have carried out experimental studies to uncover the effects that are attributed from projectile impacts onto reinforced concrete structures. As the nuclear reactor industry became more prominent, the need to quantify accident scenarios that could potentially cause breach in the containment structure, which is comprised of reinforced concrete, began to rise (Sanji, 2011). A containment structure is designed with the mindset that accidental impact loads to the structure ranging from aviation crashes to tornado produced missiles can occur (Hughes, 1984). This led to a more systematic attempt to discover the damaging behaviors missile impacts can impose on a reinforced concrete structure.

When testing missile impacts on reinforced concrete targets, the type of missile greatly influences the nature of damage that is created on the target. A missile is classified by its rigidity and categorized as being either a soft or hard missile. A soft missile has the

capability of undergoing a significant amount of deformation while employing subtle damage to a reinforced concrete target. A hard missile tends to develop little to no deformation while applying a significant amount of damage to a reinforced concrete target. Both types of missiles will produce a global and local effect on the overall structure.

Global damage is defined as the damage that is sustained by the entire structure which is generally observed as the overall bending and deformation of the reinforced concrete structure. Local damage is denoted by the damage sustained in a control volume that encompasses the region where energy is dissipated around the impact zone. Different forms of local damage can be defined by the damage pattern created by an impacting missile. In 2005, Li et al. conducted a comprehensive review for concrete impacts and the variations of local damage effects that can be produced from missile impacts. The different physical responses of concrete targets impacted by missiles are defined by Li et al. (2005) as:

1. Penetration: The formation of a crater on the target being impacted at the interface between concrete and missile.
2. Cone cracking and plugging: The development of a cone shaped crack radiating from the missile impact and the ensuing plug punching caused from the shear force produced onto the structure.
3. Spalling: The process in which the impacted surface begins to break down and form fragments.
4. Radial cracking: Propagating cracks that originate at the impact interface and develop radially outwards. This can occur on the proximal surface of impact, the

distal surface of impact, or both if cracks propagate through the thickness of the target being impacted.

5. Scabbing: Fragments are formed on the distal surface of impact are ejected outwards.
6. Perforation: The process in which a projectile can completely pass through a concrete target.

Figure 2.8 shows the local damage response that Li et al. defined.

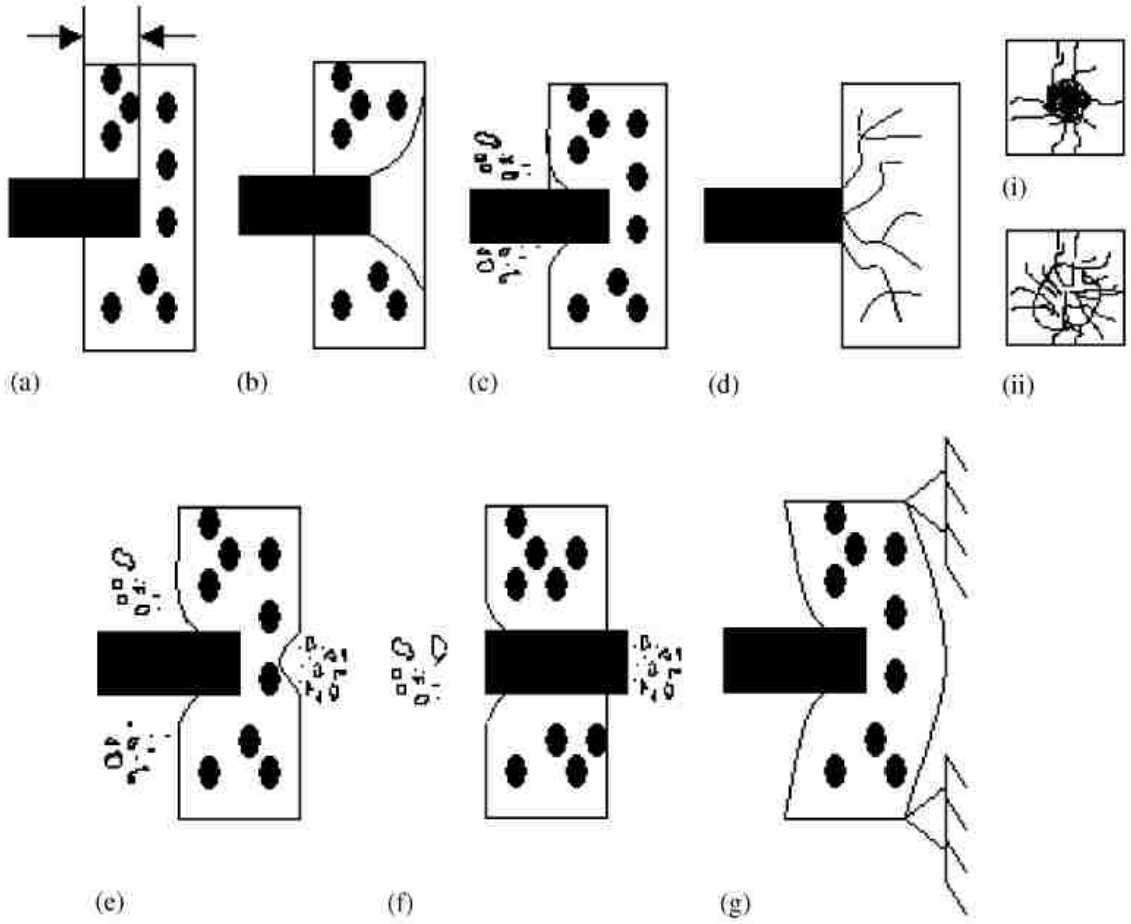

Figure 2.8: Missile impact effects on concrete target, (a) Penetration, (b) Cone cracking, (c) Spalling, (d) Cracks on (i) proximal face and (ii) distal face, (e) Scabbing, (f) Perforation, and (g) Overall target response. (Li et al., 2005)

Investigations into the various localizing damage patterns generated from ballistic impacts have been documented since the early 1900's. The measurable characteristics commonly associated with localized damage have been, to some extent, quantified using empirical formulas from many different researchers and research institutions. The four measurements commonly known to be utilized in these calculations and are also defined by Li et al. (2005) are:

1. Penetration depth (x): The depth to which a projectile penetrates into a massive concrete target without perforation.
2. Scabbing limit (h_s): The minimum thickness of the target required to prevent scabbing.
3. Perforation limit (e): The minimum thickness of the target required to prevent perforation.
4. Ballistic limit (V_{BL}): The minimum initial impact velocity required to perforate the target.

The empirical formulas used to calculate penetration, scabbing, and perforation are dependent on a number of different parameters. Formulas that capture the penetration depth of a ballistic impact onto concrete have been constructed over the decades since the early 1900's. Different equations that quantify the phenomenological behavior of localized damage use a subset of the common parameters listed in Table 2.1.

Table 2.1: Parameters used in empirical formulas

Symbol	Parameter	SI	Imperial
x	Penetration depth	M	Inch
e	Perforation limit	M	Inch
h_s	Scabbing limit	M	Inch
V_{BL}	Ballistic limit	M/s	Ft/s
H_c	Concrete target thickness	M	Inch
d	Missile diameter	M	Inch
D	Calibre density of missile	N/M^3	$Lbf/Inch^2$
N	Nose shape factor	-	-
a	Aggregate diameter	M	Inch
M	Mass of projectile	kg	lb
E	Elasticity of projectile	Pa	psi
V	Missile velocity	M/s	Ft/s
f_c	Compressive strength of concrete	Pa	psi
f_t	Tensile strength of concrete	Pa	psi

Many of these formulas include revisions or introduce new dependencies to preexisting equations. One of the earliest available formulas, which was developed in 1910, is the Petry equation for penetration and is given by Eq. (2.4) (Kennedy, 1976):

$$\frac{x}{d} = 0.06KDlog(1 + \frac{V}{200000}) \quad (2.4)$$

Where K is defined as the penetrability of concrete which is dependent on the strength of the concrete and level of reinforcement in the target. For normal concrete with no reinforcement, K = 0.00799, while K = 0.00426 and K = 0.00284 for normally reinforced and heavily reinforced concrete, respectively.

Research facilities like the Ballistic Research Laboratory (BRL), Army Corps of Engineers (ACE), and the US National Defense Research Committee (NDRC) all contributed to the formulation of empirical equations that predict localized damage for penetration, scabbing and perforation. During World War II, more than 900 projectiles with varying diameters were propelled to concrete targets with varying compressive strengths to aid in the development of these formulas. The empirical formulas developed were known to be accurate yet contingent on the validity range of certain parameters such as the projectile velocity. The equation for penetration created by the BRL in 1941 is given by Eq. (2.5) (Kennedy, 1976):

$$\frac{x}{d} = \frac{427}{f_c} D d^{0.2} \left(\frac{V}{1000}\right)^{1.33} \tag{2.5}$$

The modified equation for scabbing based on the scabbing BRL formula is given by Eq. (2.6) (Kennedy, 1976 and other):

$$\frac{h_s}{d} = 2\frac{x}{d} \tag{2.6}$$

Chelapati et al. introduced the limit of perforation that was based on the penetration depth formula developed by BRL and is given by Eq. (2.7) (Chelapati-Kennedy, 1972):

$$\frac{e}{d} = 1.3\frac{x}{d} \tag{2.7}$$

As a continuing effort, empirical equations were also developed by ACE and were based on the results obtained by the BRL. The ACE equations for penetration, scabbing, and perforation are given respectively by Eq. (2.8)-(2.10) (ACE, 1946):

$$\frac{x}{d} = \frac{282.6}{f_c} D d^{0.215} \left(\frac{V}{1000}\right)^{1.5} + 0.5 \tag{2.8}$$

$$\frac{h_s}{d} = 2.28 + 1.13\frac{x}{d} \tag{2.9}$$

$$\frac{e}{d} = 1.23 + 1.07\frac{x}{d} \tag{2.10}$$

The equations for scabbing and perforation developed by the ACE are based on modified regression analysis of ballistic test data for varying steel cylindrical missiles to include bullet calibres of 0.5 which induced a slight effect on the original equations. In 1946, the NDRC put forward another empirical formula that was a continuing effort based on the ACE formulas and included further testing of solid missiles with a much more analytical approach. The NDRC included some variables such as the shape factor of the missile and concrete penetrability, which was first introduced by Petry in 1910, to calculate the penetration. After fitting to experimental data, Kennedy found a relationship between the compressive strength of concrete and the concrete penetrability factor. The modified formulas of NDRC for penetration, scabbing, and perforation are given by Eq. (2.11)-(2.13) (Kennedy, 1966):

$$\frac{x}{d} = 1 + \frac{180 N d^{0.2} D}{f_c^{0.5}} \left(\frac{V}{1000}\right)^{1.8} ; \frac{x}{d} > 2 \tag{2.11}$$

$$\frac{h_s}{d} = 2.12\frac{x}{d} + 1.36\frac{x}{d}; 0.65 < \frac{x}{d} \leq 11.7 \quad (2.12)$$

$$\frac{e}{d} = 1.32\frac{x}{d} + 1.24\frac{x}{d}; 1.35 < \frac{x}{d} \leq 13.5 \quad (2.13)$$

Most empirical equations used to calculate localized damage share similarities between each other. Some of the most common parameters seen in the majority of equations developed are missile diameter, missile velocity, and material dependency.

2.3 Concrete Material Models

The development of numerical modeling and the processing power of modern day computers has allowed simulations to gradually be able to capture the mechanistic behavior of cementitious materials more accurately. Since the nature of concrete is complex, this led to the development of a fairly large amount of constitutive models. These models can be categorized by what their formulation encompasses. The rudimentary models, on the lower end of the spectrum for complexity, are only suitable for the elastic regime when simulating cementitious materials. Further developed models tend to include the plastic regime of a cementitious material's behavior. The most sophisticated concrete models are able to capture the phenomenological response of cementitious materials in their elastic, plastic, and damage/fractured state where the material's strength degrades with increasing strain. These models can also include strain rate dependence, pressure dependence, and display anisotropic properties. While most complex constitutive concrete models are reliable for quasi-static simulations, there is still a need to further study, enhance, and develop models to accurately capture the behavior of concrete during impulse loading conditions.

Many concrete material models have been studied extensively with impact simulations to observe the fracture response of cementitious material models. Reinforced concrete needs to be studied more extensively since the complexity embedded rebar adds to a simulation is sometimes difficult to quantify. The common approach to analyze a material model, subjected to impulse loading, is to first calibrate the model to standardized experimental tests and implement the calibrated parameters to high-rate loading/dynamic simulations. Some constitutive models that have been produced in recent years that are particularly noteworthy are the Holmquist-Johnson series; more specifically the Holmquist-Johnson-Cook (HJC) concrete model and the Johnson-Holmquist II (JH2) model. The aforementioned material models are suitable for the behavior of concrete and other brittle materials that are subjected to impact conditions that produce large strains, high strain rates, and high pressures.

2.3.1 Holmquist-Johnson-Cook (HJC) Concrete Model

The HJC and JH2 material models contain the same three basic elements:

1. Pressure dependent yield surface that represents the deviatoric strength of the material at an intact and fractured/damaged state.
2. Induced damage that transitions a material from its intact non-damaged state to a fractured/damaged state.
3. Pressure-volume relationship that is governed by an equation of state and captures nonlinear effects attributed by compaction in the material.

2.3.1.1 Strength

The HJC model describes the formulation for strength as a pressure and strain rate dependent equation (Holmquist et al., 1993) which is expressed in Eq. (2.14).

$$\sigma^* = (A(1-D) + BP^{*N})(1 + C \times \ln(\frac{\dot{\varepsilon}}{\dot{\varepsilon_o}})) \tag{2.14}$$

Equation (2.14) states that as a material experiences higher confining pressures and increasing strain rates, the material's yield strength will also increase. The material constants A (cohesive strength coefficient), B (pressure coefficient), C (strain rate coefficient), and N are determined by fitting the model to experimental data. The parameter D is a scalar damage variable, described in greater detail in the following section, where damage can span a value from 0 to 1 and relates to the damage state of a material. When D = 0, the material is undamaged and its strength corresponds to the strength of the material fully intact. While D = 1, the material is damaged and its strength corresponds to the strength of the material at a fully fractured state which only retains the least confined shear strength. The normalized pressure is given as the pressure divided by the unconfined compressive strength ($P^* = P / f_c{}'$), which is derived from unconfined axial compressive mechanical test data while $\dot{\varepsilon}$ and $\dot{\varepsilon_o}$ are defined as the equivalent plastic strain rate and reference strain rate respectively. A Mises flow surface is followed and plastic flow is assumed to be isochoric. The pressure-dependent strength behaviors of materials for the HJC material model can be obtained by loading unconfined and confined cylindrical samples. By loading cylindrical samples in an axial direction with no confinement and hydrostatic confinement radially at varying pressures, a correlation between stress-strain and pressure-strength data can be acquired from the experimental test data and used to derive parameters for the HJC model.

2.3.1.2 Damage

Damage variables accumulate and can be defined by the accumulation of volumetric plastic strain ($\Delta\mu_{pl}$) and equivalent plastic strain which ($\Delta\varepsilon_{pl}$) which are caused by the volumetric compaction and deformation/fracture respectively. Damage is calculated by dividing the summation of plastic volumetric strain and equivalent plastic strain by the plastic strain to fracture at constant pressure (ε_f). The equation for damage accumulation and plastic strain to fracture are given by the Eqn. (2.15) and (2.16) respectively.

$$D = \sum \frac{\Delta\varepsilon_{pl} + \Delta\mu_{pl}}{\varepsilon_f} \tag{2.15}$$

$$\varepsilon_f = D1(P^* + T^*)^{D2} \tag{2.16}$$

The plastic strain to fracture is determined by using the normalized pressure and normalized tensile strength (T^*) which is normalized with the unconfined tensile strength obtained from experimental tensile test data. The damage parameters D1 and D2 are chosen from unconfined experimental compressive data. In most cases, D2 is chosen to be 1.0 in order to have a linear relationship between the plastic strain to fracture and normalized pressure. Therefore as the normalized pressure increases, the plastic strain to fracture will linearly increase. Typically, the majority of damage that is accumulated is obtained by fracturing the material while a small portion is attributed to the volumetric compaction. The HJC material model also includes the addition of a minimum plastic strain to fracture variable (EFMIN) which provides a lower limit of plastic strain a material will fracture at. As seen in equation (2.14), the damage variable solely affects the cohesive strength parameter (A), which is directly related to a loss of shear strength.

2.3.1.3 Pressure

A material's hydrostatic pressure response to volumetric strain is described by Homlquist as having three distinct regions in compression. The first region is a linear section governed by the materials elastic properties from zero to predetermined crush values for pressure and volumetric strain acquired from experimental data. Any deformation acquired in this region is recoverable since it's all elastic. The second region starts from the crush values of pressure and volumetric strain (μ_{crush}, P_{crush}), which occurs from the onset of concrete crush to its locking region. This section is the transition region that relates to concrete plasticity and produces a modified unloading path that is interpolated from adjacent regions. The third region starts from the corresponding point (μ_{lock}, P_{lock}) and is associated with a material that is fully dense (air voids in material are completely compressed). The three distinct regions showing the hydrostatic pressure and volumetric relationship for HJC is shown schematically in Figure 2.9.

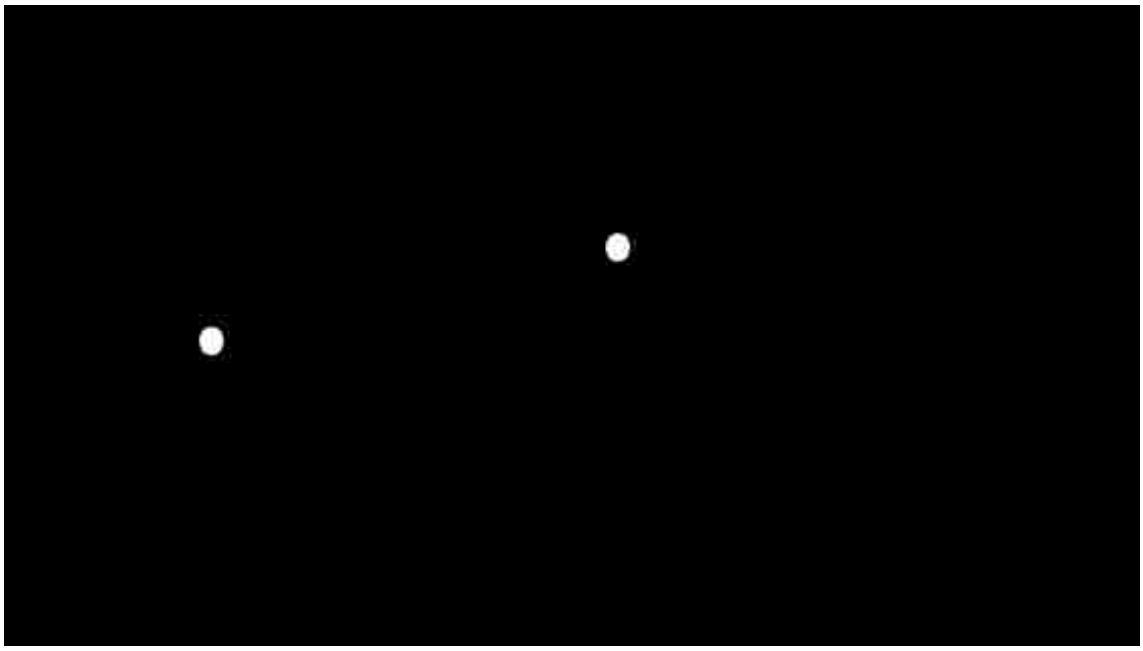

Figure 2.9: HJC hydrostatic pressure and volumetric strain relationship

The volumetric strain is defined as being a function of the current density (ρ) and reference density (ρ_o). The equation for volumetric strain is given in Eq. (2.17).

$$\mu = \frac{\rho}{\rho_o} - 1 \tag{2.17}$$

The formulation for the linear elastic and cubic locking region is given in Eq. (2.18) and (2.19) respectively. The elastic and crushing region have similar linear relationships while the locking region introduces a nonlinear relationship between the hydrostatic pressure and volumetric strain.

$$P = K_e \mu \tag{2.18}$$

$$P = K_1 \mu + K_2 \mu^2 + K_3 \mu^3 \tag{2.19}$$

The different variations of K in the previous equation are all material constants that relate to the bulk modulus (K_e).

2.3.2 Johnson-Holmquist (JH2) Ceramic Model

The JH2 model is the second iteration of the Johnson-Holmquist ceramic model that can accurately describe the phenomenological behavior of brittle materials such as strain-rate effects, pressure-strength dependence, and dilatation induced by damage (Johnson-Holmquist, 1993). The second iteration model was developed in 1993 to encompass the capabilities of the previous JH1 ceramic model (Johnson-Holmquist, 1992), along with a new feature that captures the gradual-softening behavior of ceramics impacted by flyer-plates. The new JH2 also continuously degrades the yield strength as damage accumulates whereas the JH1 ceramic model would only degrade the yield strength once critical damage was reached in the model.

2.3.2.1 Strength

The JH2 model expresses strength in terms of normalized equivalent stress given by the state of the material, and the equations associated with each state. When a material is undamaged (D = 0), the model follows the equation of strength for a material that is intact and is expressed as

$$\sigma_i^* = A(P^* + T^*)^N(1 + Cln\ \dot{\varepsilon}^*) \tag{2.20}$$

When a material is fully damaged (D = 1), the model follows the equation of strength for a material that is fractured and is expressed as

$$\sigma_f^* = B(P^*)^M(1 + Cln\ \dot{\varepsilon}^*) \tag{2.21}$$

If a material's damage state lies between intact and fractured (0 < D < 1), then the governing equation for strength can be expressed as

$$\sigma^* = \sigma_i^* - D(\sigma_i^* - \sigma_f^*) \tag{2.22}$$

All of the coefficients and power variables (A, B, C, M, and N) are material parameters that can be derived through experimental data and $\dot{\varepsilon}^*$ is the strain rate normalized by a reference strain rate. The equations for strength are made dimensionless by normalizing them to the equivalent stress at the Hugoniot Elastic Limit (HEL), which corresponds to a uniaxial strain shock wave that exceeds the elastic limit. The strength equations are normalized through

$$\sigma^* = \frac{\sigma}{\sigma_{HEL}} \tag{2.23}$$

The normalized pressure (P^*) is given as the actual pressure divided by the pressure at the HEL. The maximum tensile hydrostatic pressure (T^*) is given as the maximum tensile pressure divided by the pressure at the HEL.

2.3.2.2 Damage

Similar to the HJC concrete model, the JH2 ceramic model also accumulates damage through the summation of the equivalent plastic strain, but not through volumetric compaction, all divided by the plastic strain to fracture at constant pressure. The equation for damage is given by the following equation

$$D = \sum \frac{\Delta \varepsilon_{pl}}{\varepsilon_f} \tag{2.24}$$

The equation for plastic strain to fracture for the JH2 model is equivalent to the equation for plastic strain to fracture for the HJC model with the only exception being what the normalized pressure (P^*) and maximum hydrostatic tensile strength (T^*) are being normalized by. Similarly, D1 and D2 are obtained through unconfined experimental compression test data and the plastic strain, ε_{pl}, and fracture strain, ε_f, are used to obtain damage.

$$\varepsilon_f = D1(P^* + T^*)^{D2} \tag{2.25}$$

2.3.2.3 Pressure

For dynamic loads, the equation of state that provides a pressure-volume relationship for brittle materials can be given as

$$P = \begin{cases} K_1\mu + K_2\mu^2 + K_3\mu^3 & (Compression) \\ K_1\mu & (Tension) \end{cases} \quad (2.26)$$

The different variations of the material constant K in the JH2 model can be obtained from plate impact or diamond anvil experiments. The JH2 model also contains an increment pressure term that compensates for elastic energy loss when a material experiences plastic deformation. This equation is expressed by

$$P = K_1\mu + K_2\mu^2 + K_3\mu^3 + \Delta P \quad (2.27)$$

Figure 2.10 presents the pressure and volumetric strain relationship for the JH2 model in compression.

Figure 2.10: Pressure-Volumetric strain relationship for JH2

When a material transitions from an undamaged state to a damaged one and the commencement of material softening occurs, a decrease in the deviatoric elastic energy (ΔU) is produced. To conserve the internal energy that would be lost by this process, the

incremental pressure term is added to mitigate the loss of elastic energy by converting it to potential hydrostatic energy. An approximation of the aforementioned procedure is given by the following equation

$$\Delta P_{t+\Delta t} = -K_1 \mu_t + \sqrt{(K_1 \mu_t + \Delta P)^2 + 2\beta K_1 \Delta U} \qquad (2.28)$$

where β is defined as the fraction of elastic energy that is converted to potential energy and μ_t is the dilatation of the current time step.

2.4 Summary

The discussed literature review is a precursor in understanding the nature of complex ballistic simulations for cementitious materials. It is vital to know mechanistic behavior of materials, the dynamic effects that induce damage upon a structure, and applying correct theoretical models whose constitutive equations capture the response of the material being studied. It is clear from the literature review that modeling reinforced concrete subjected to impact loads is fairly complex. For the aforementioned reason, more analytical studies need to be conducted in order to further develop theoretical models to more accurately predict concrete response, subjected to ballistic impacts, in numerical simulations.

CHAPTER 3

OVERVIEW OF VTT MISSILE IMPACTS FOR IRIS PHASE II

3.1 Introduction

In support of the Committee on the Safety of Nuclear Installations (CSNI), the IRIS series was approved and organized by the working sub group of the CSNI, the Integrity and Ageing of Components and Structures (IAGE) group. The project was a round-robin exercise that would help promote better guidance for conducting impact analysis on structures, further develop the modeling methods and to improve analysis techniques. The phase II of the IRIS round robin revolved around modeling a flexural and punching impact test conducted in the VTT facility in Finland. The flexural experiment was conducted by impacting a thin slab of reinforced concrete with a thin walled stainless steel hollow missile. Similarly, the punching experiment impacted a reinforced concrete slab that was much thicker with a steel covered concrete solid missile. Along with the missile impact tests, material and experimental data was collected and provided to the analysts working on modeling the benchmark exercise for phase II. The material data provided included stress-strain relationship for all metallic elements in the impact tests (6mm diameter rebar,

10mm diameter rebar, steel missile), as well as compression data for high strength concrete at various confinement pressures. The experimental data collected for the flexural impacts consisted of displacements, concrete damage, and rebar strains acquired from transducers, photographs, strain gauges respectively. The punching impact included a solid missile that completely perforated the concrete target which left damage profiles that were also obtained with photographs (OECD-NEA, 2014).

3.2 Concrete

The high strength concrete utilized in the impact experiments was tested on standard 70 mm diameter by 140 mm long concrete specimens. The cylindrical concrete specimens were subjected to both uniaxial and triaxial compression testing to obtain a stress-strain relationship for the concrete that would be casted to make the impact targets. The triaxial tests conducted were run with varying confinement pressures from 15.5 MPa to 100 MPa. Deformation was captured using strain gauges in two different directions, vertical and horizontal. As all triaxial tests that are conducted, a confining fluid is pressurized in order to introduce a confining pressure around the concrete specimen. A latex membrane is placed around the concrete to prevent confinement fluid from penetrating cracks in the specimen during testing. All experimental compression test data collected from CSNI can be seen overlaid for all specimens tested in Figure 3.1.

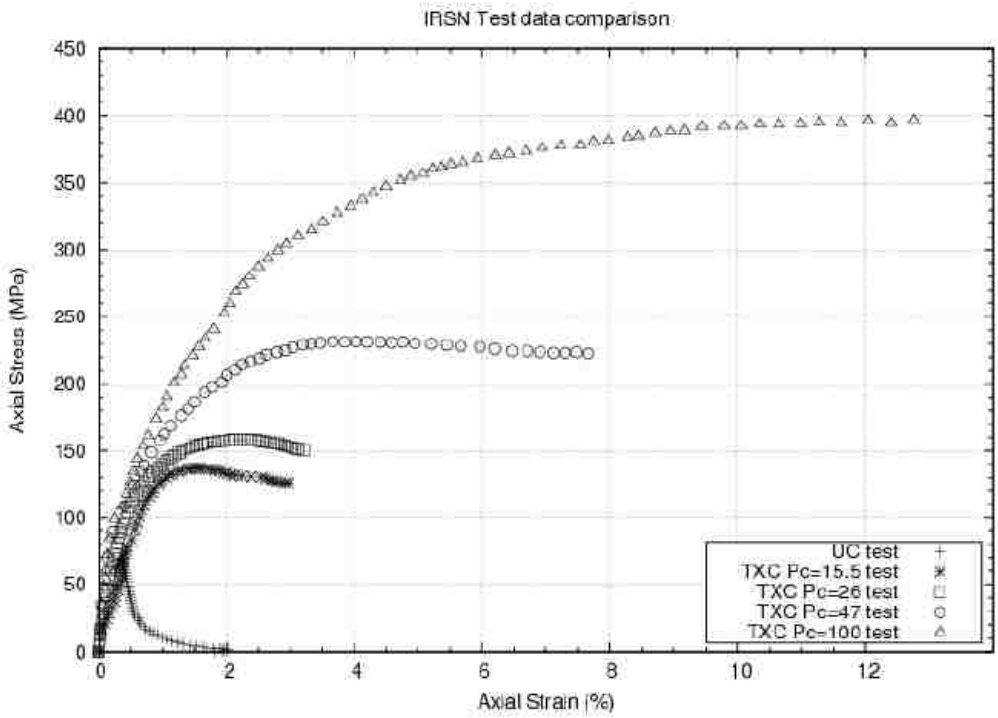

Figure 3.1: 2012 ISRN Axial stress-strain data for unconfined (UC) and Triaxial Compression (TXC) concrete specimens at varying confinment pressures

3.3 Rebar

For both major experiments (flexural and punching), the same rebar material was used for the reinforcement of the concrete target with two different sizes. The flexural experiment contained 6mm diameter A500HW steel rebar while the punching experiment contained 10mm diameter A500HW steel rebar. The experimental data for tensile tests on the two different sizes of rebar can be seen in Figure 3.2 and Figure 3.3 for 6 mm and 10 mm diameter respectively.

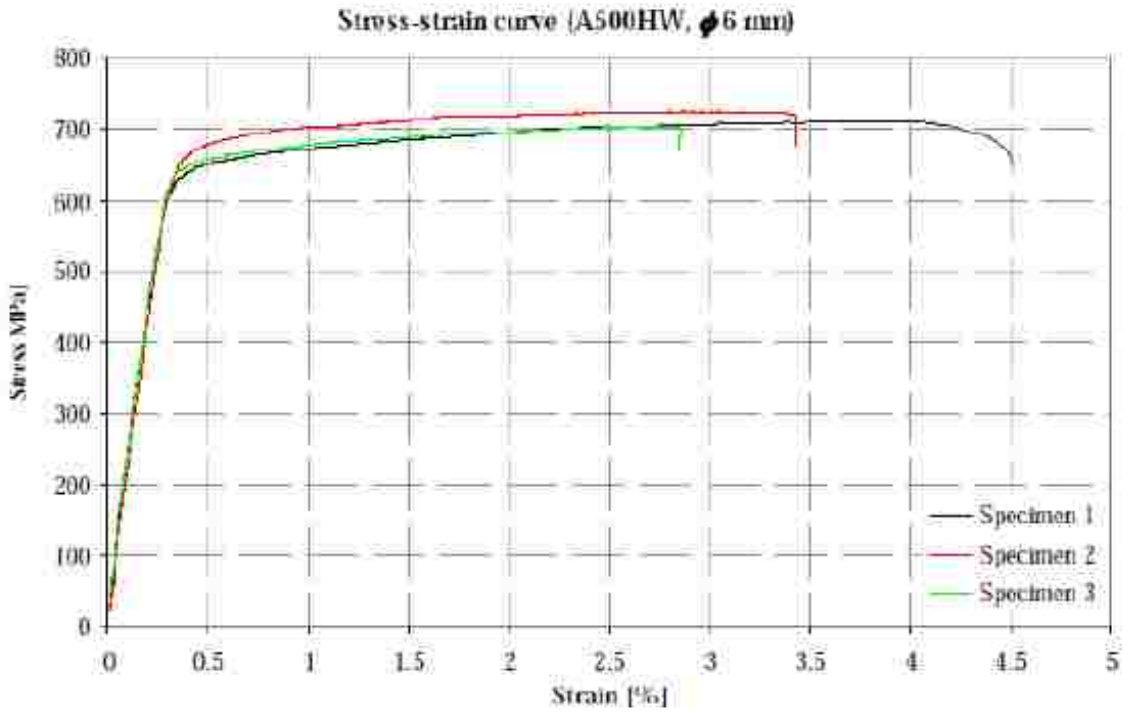

Figure 3.2: Stress-strain curve for A500HW 6mm steel rebar

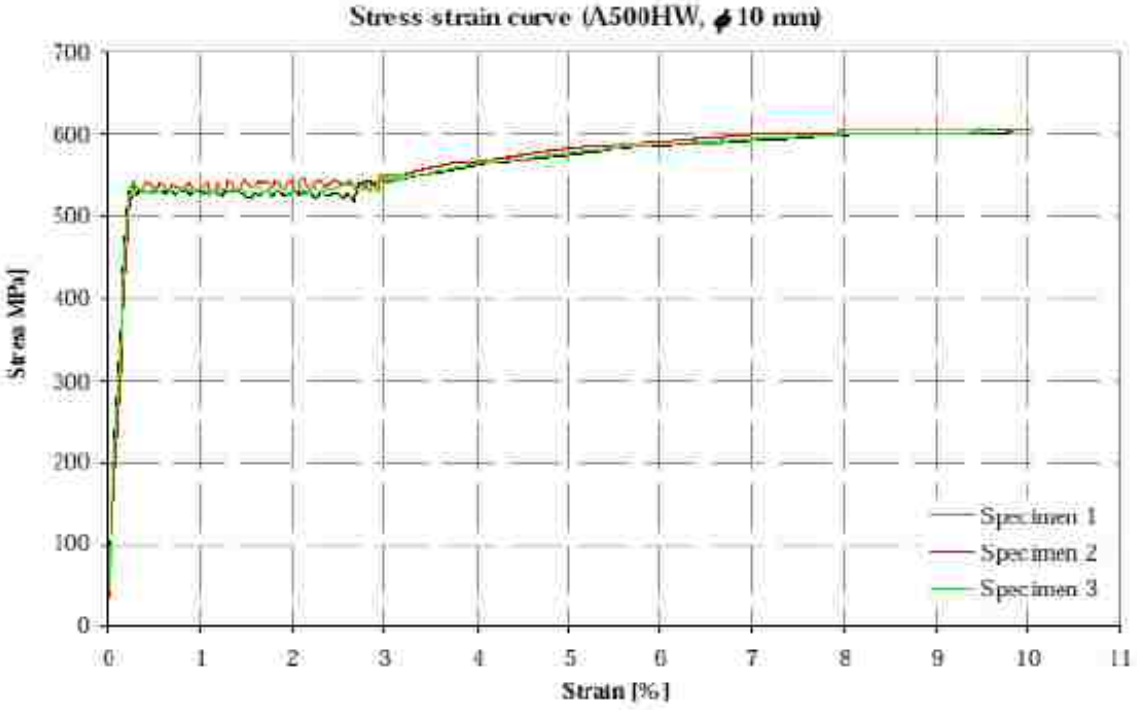

Figure 3.3: Stress-strain curve for A500HW 10mm steel rebar

The rebar data provided for the IRIS phase II is slightly misleading as Luders strain effects can be seen in the larger diameter rebar test and not the smaller diameter rebar. This is primarily attributed to the non-uniform deformation of the larger tensile specimen that results in localized yielding that does not occur uniformly throughout the entirety of the larger specimen. Also, the minimum required elongation for fracture of 12% was not achieved for either rebar for unknown reasons. It is important to note that the 6mm steel rebar tested produced much stronger results than expected for the 500 MPa Finish standards for steel rebar.

3.4 VTT Flexural

The flexural test conducted at the VTT test facility in Finland involved a soft impact from a thin shelled steel missile hitting a reinforced concrete slab held in a steel structure. The impact occurred at 110 m/s with a missile mass, length, and diameter of 50 kg, 2.111 m and 0.254 m, respectively. Figure 3.4 and Figure 3.5 shows the missile drawing and material data for the majority of the missile, respectively.

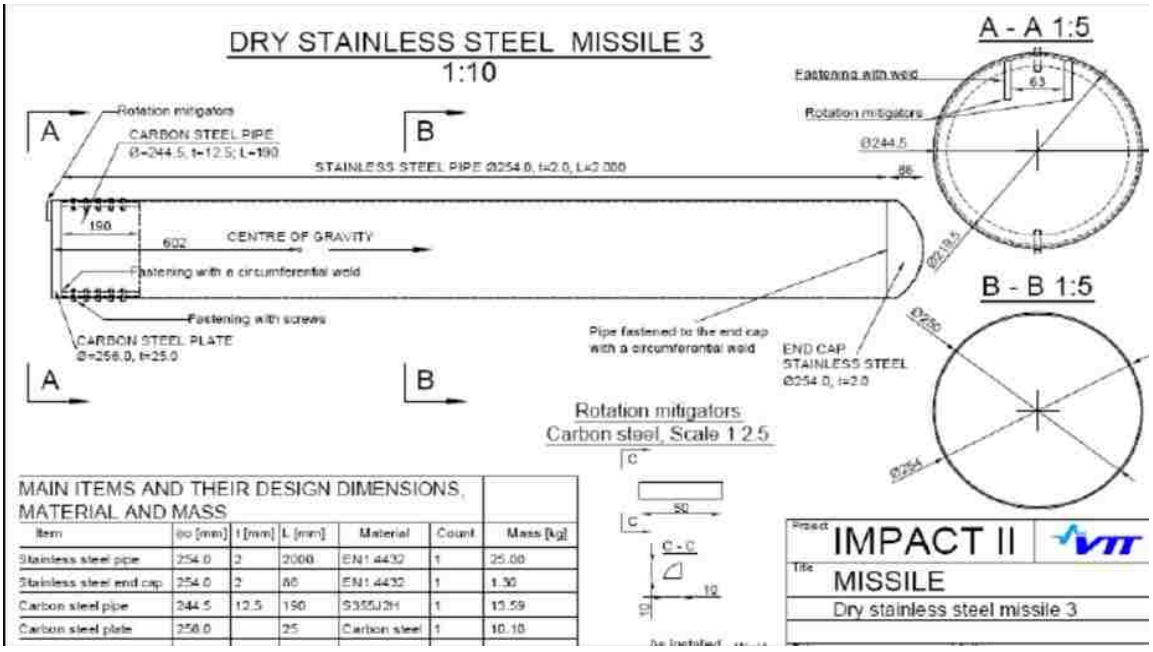

Figure 3.4: ISRN VTT flexural steel missile engineering drawing

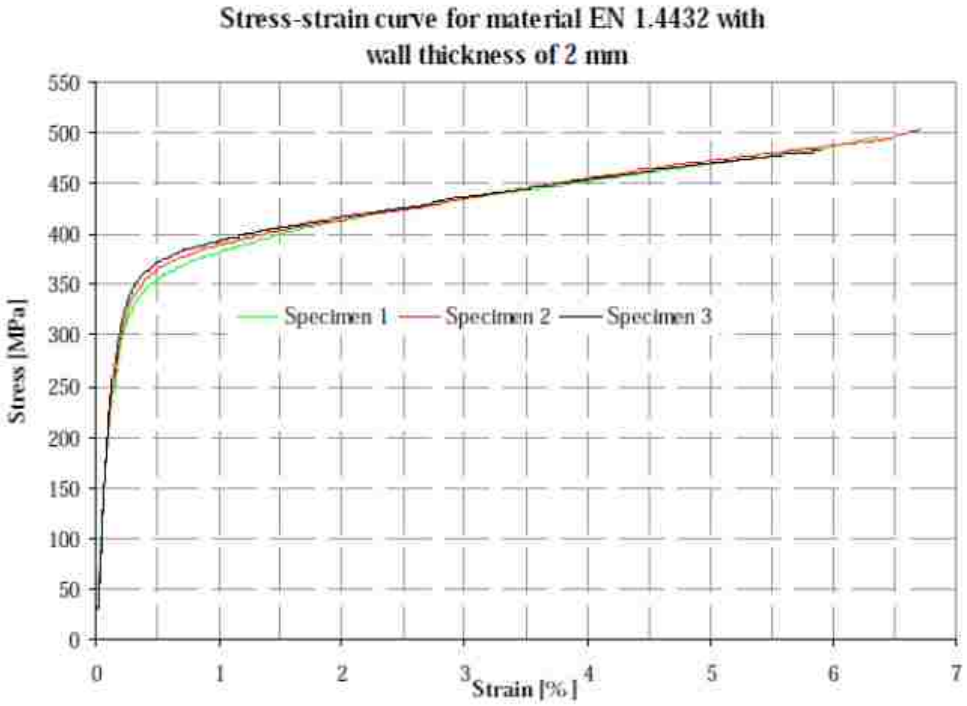

Figure 3.5: Stress-strain curve for flexural missile material EN 1.4432

The flexural engineering drawing, simply supported mounting fixture schematic and supporting frame structure can be seen in Figure 3.6, Figure 3.7, and Figure 3.8 respectively.

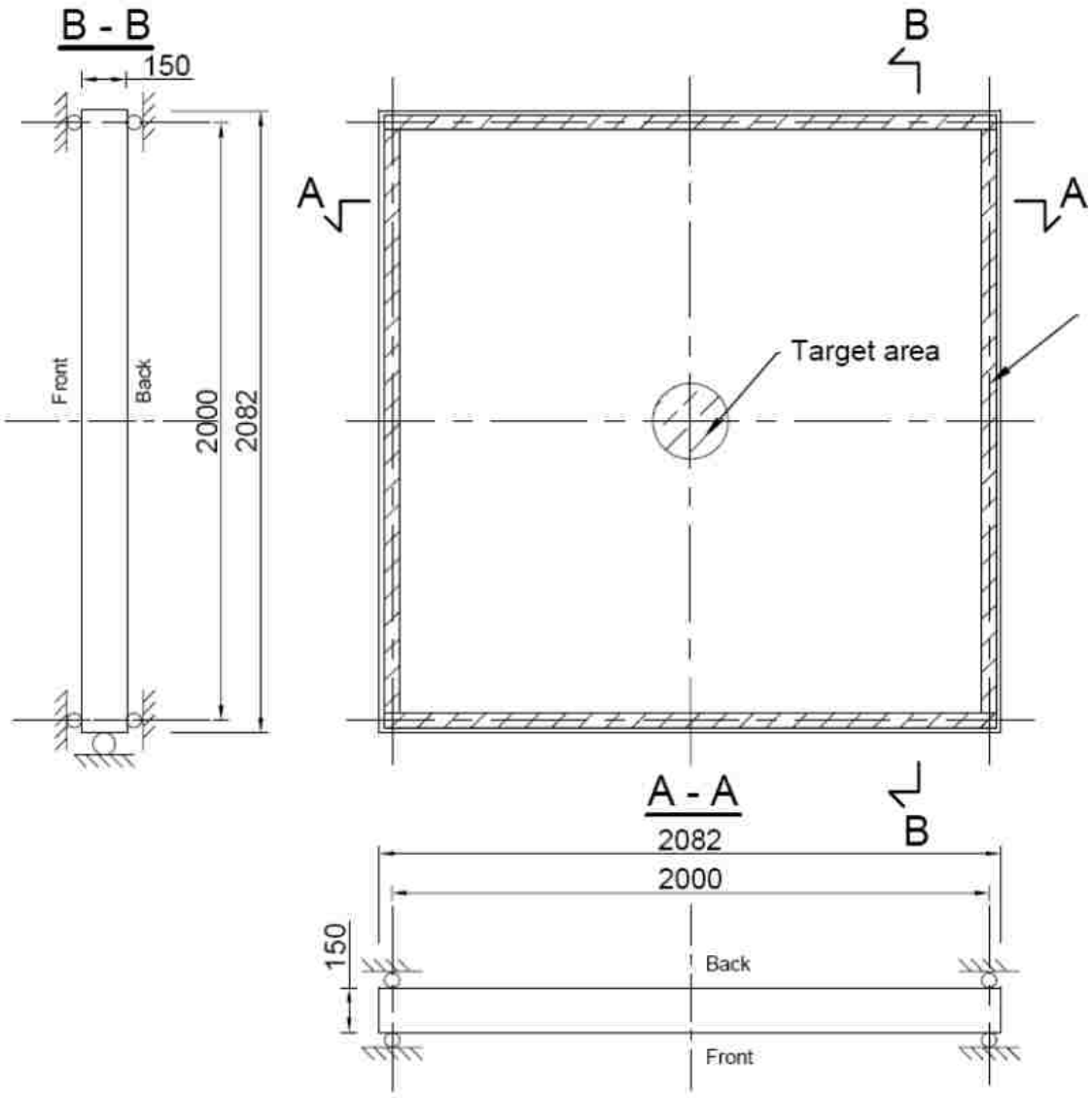

Figure 3.6: IRSN VTT Flexural engineering drawing

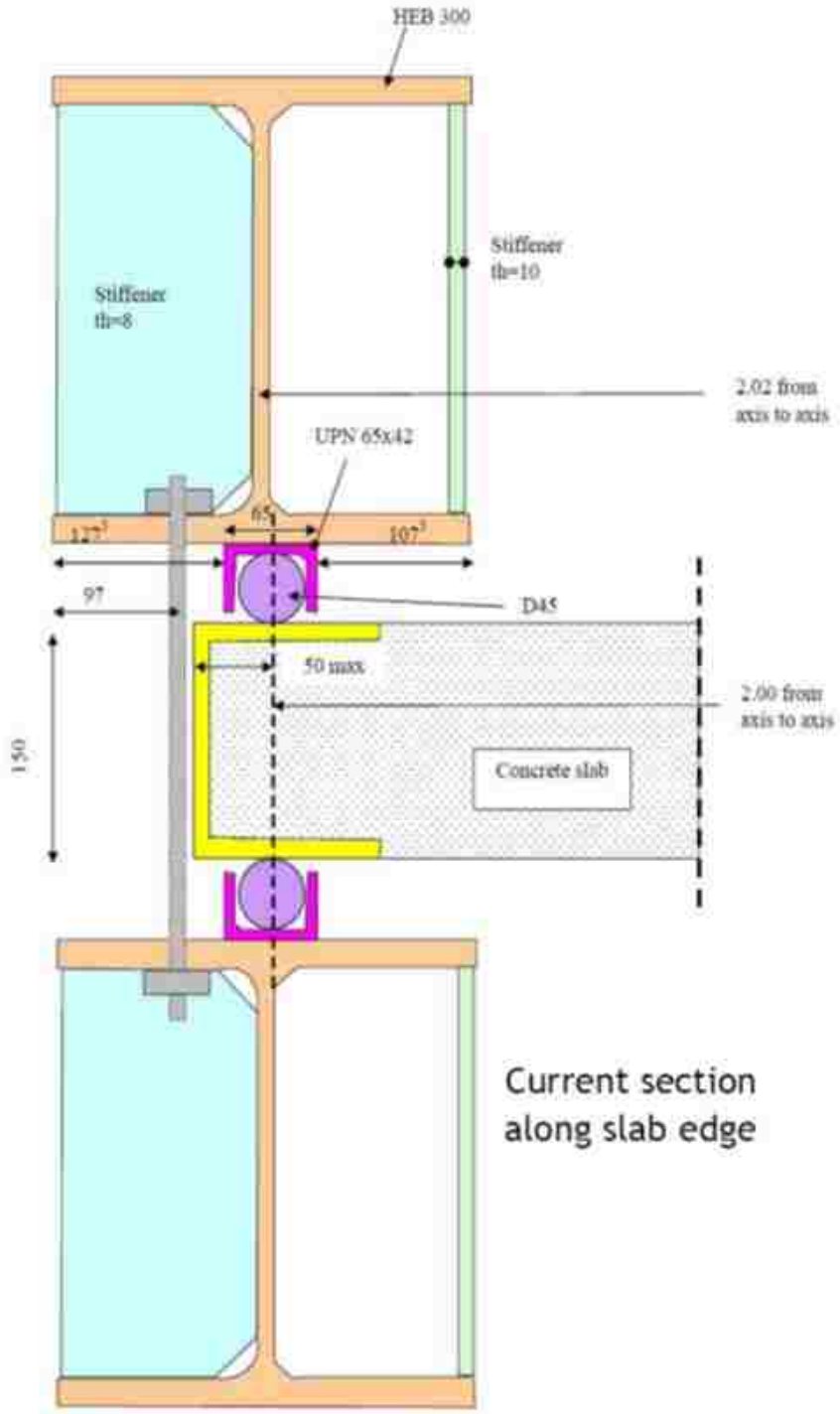

Figure 3.7: IRSN VTT Flexural mounting fixture schematic

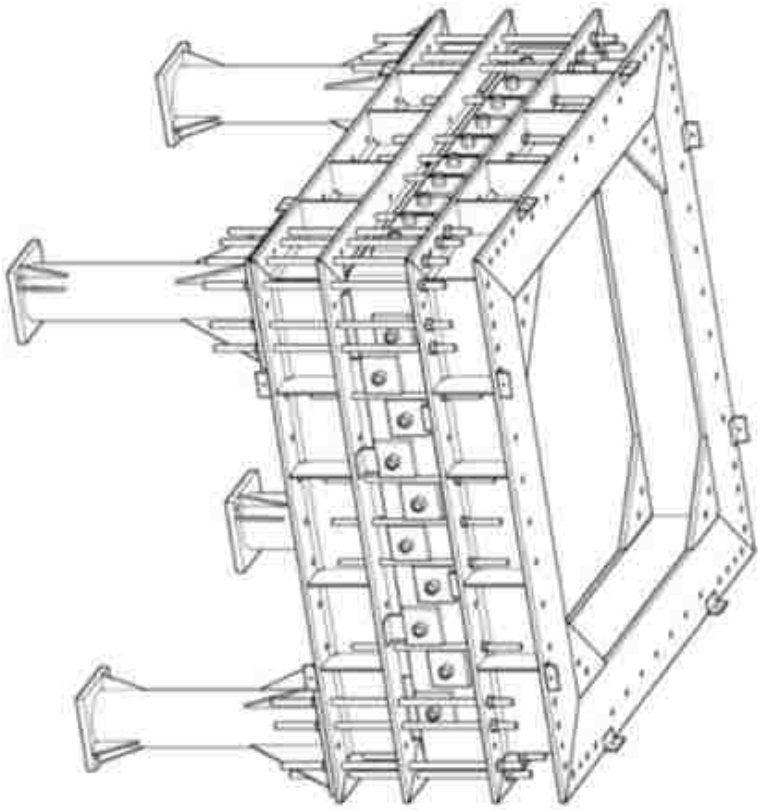

Figure 3.8: IRSN VTT supporting structure

For the reinforcing steel, rebar was placed in two different longitudinal directions and through the target in the transverse direction. The rebar running in the longitudinal direction was given a 55 mm spacing between rebar, 15 mm concrete cover, and an overall rebar density of 5 $\frac{cm^2}{m}$ for each direction. The rebar in the transverse direction was given the same concrete cover with a larger spacing of 75 mm and a rebar density of 50 $\frac{cm^2}{m^2}$.

As previously mentioned, data was collected for the flexural impact test using displacement transducers and strain gauges. Figure 3.9 and Figure 3.10 display the monitoring locations for out of plane displacements on the rear wall of the slab and axial rebar strains within the concrete target, respectively.

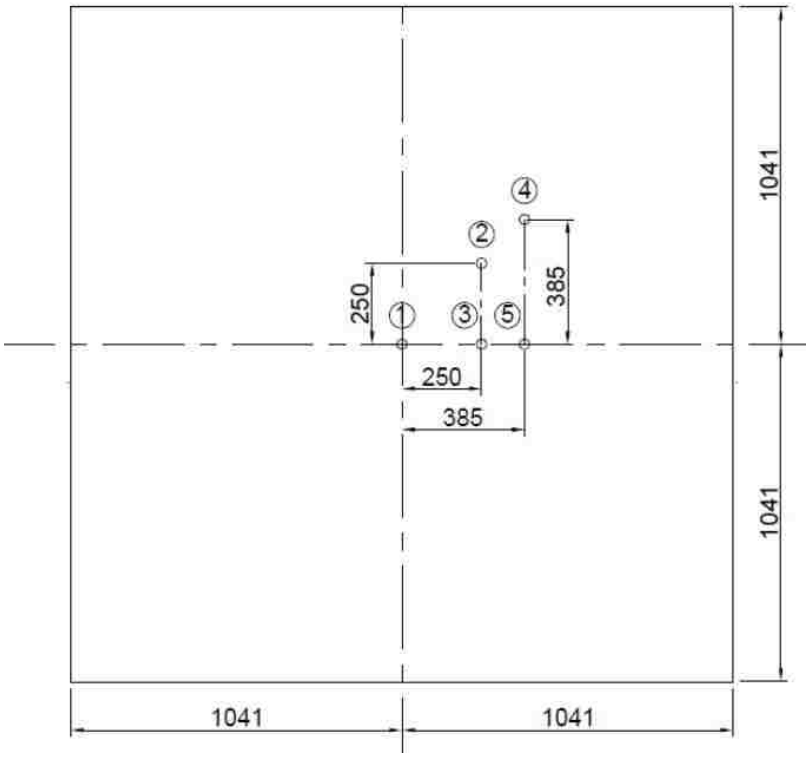

Figure 3.9: IRSN VTT Flexural displacement transducer locations on rear surface

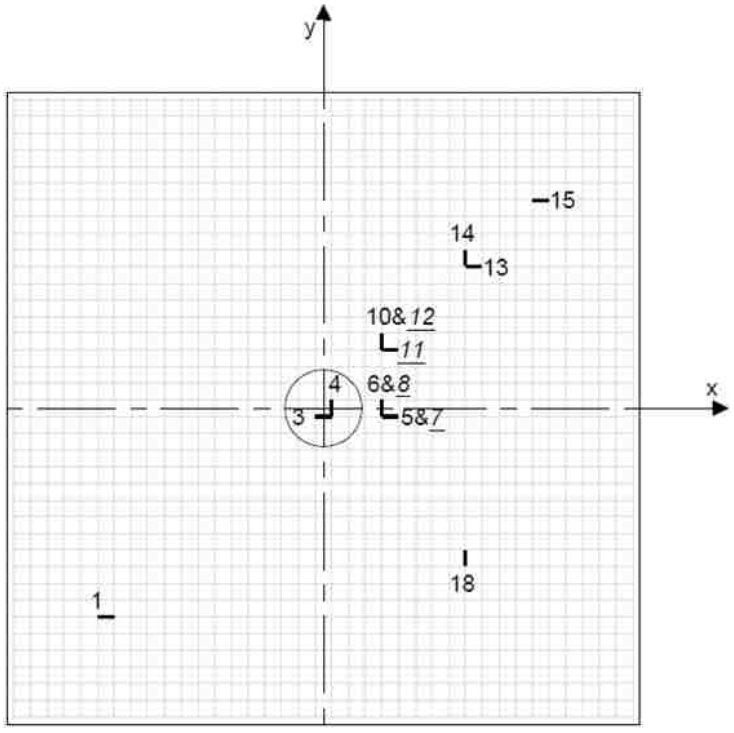

Figure 3.10: IRSN VTT Flexural rebar strain gauge locations

All experimental data recorded from the flexural impact test consisted of time history responses for displacement and deformation at the specified locations from the previous figures.

3.5 VTT Punching

The Punching test conducted at the VTT test facility in Finland involved a hard impact from a steel covered concrete missile hitting a reinforced concrete slab held in the same structure as the Flexural test. The punching slab contains slightly larger dimensions than the flexural slab; thickness being the most significant difference between the two slabs. The solid missile impacted the concrete slab at a velocity of 136 m/s, which generated a hard impact that perforated the concrete slab. Along with the aforementioned differences, larger rebar (10mm) was used to produce a rebar density of 8.7 $\frac{cm^2}{m}$ for each longitudinal direction with a 90mm rebar spacing and no transverse rebar was included. Figure 3.11, Figure 3.12, Figure 3.13, and Figure 3.14 display the solid missile engineering drawing, punching engineering drawing, reinforcing steel rebar cross-section and mounting schematic for the punching test, respectively.

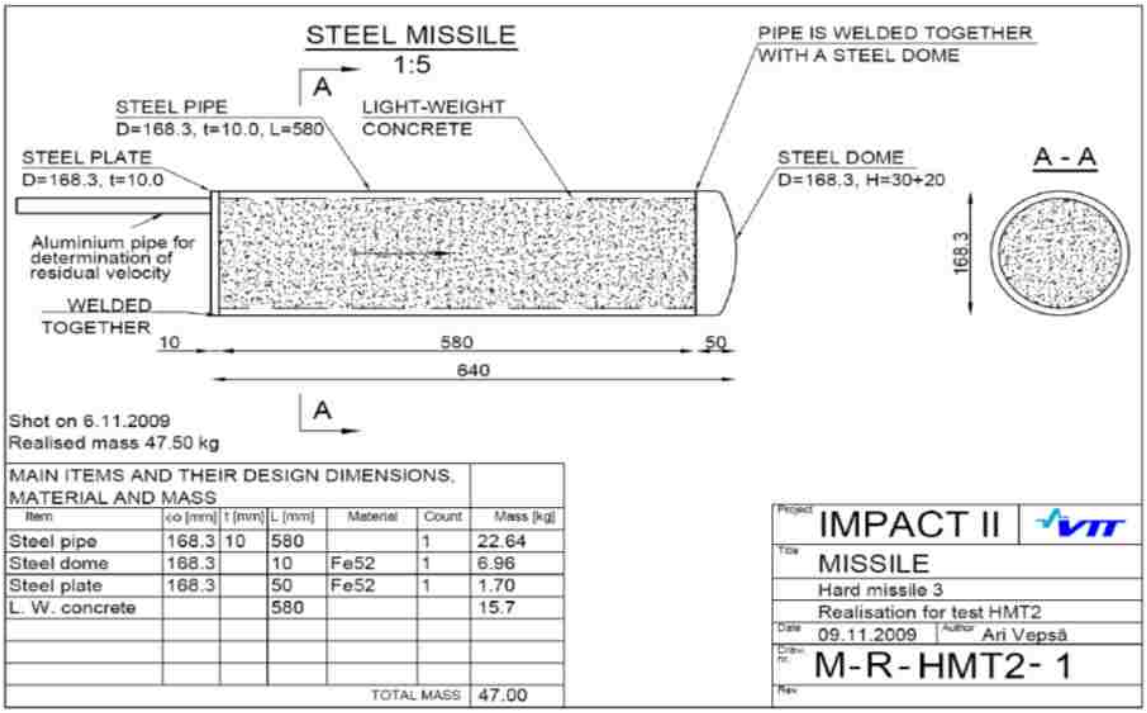

Figure 3.11: IRSN VTT Punching solid missile engineering drawing

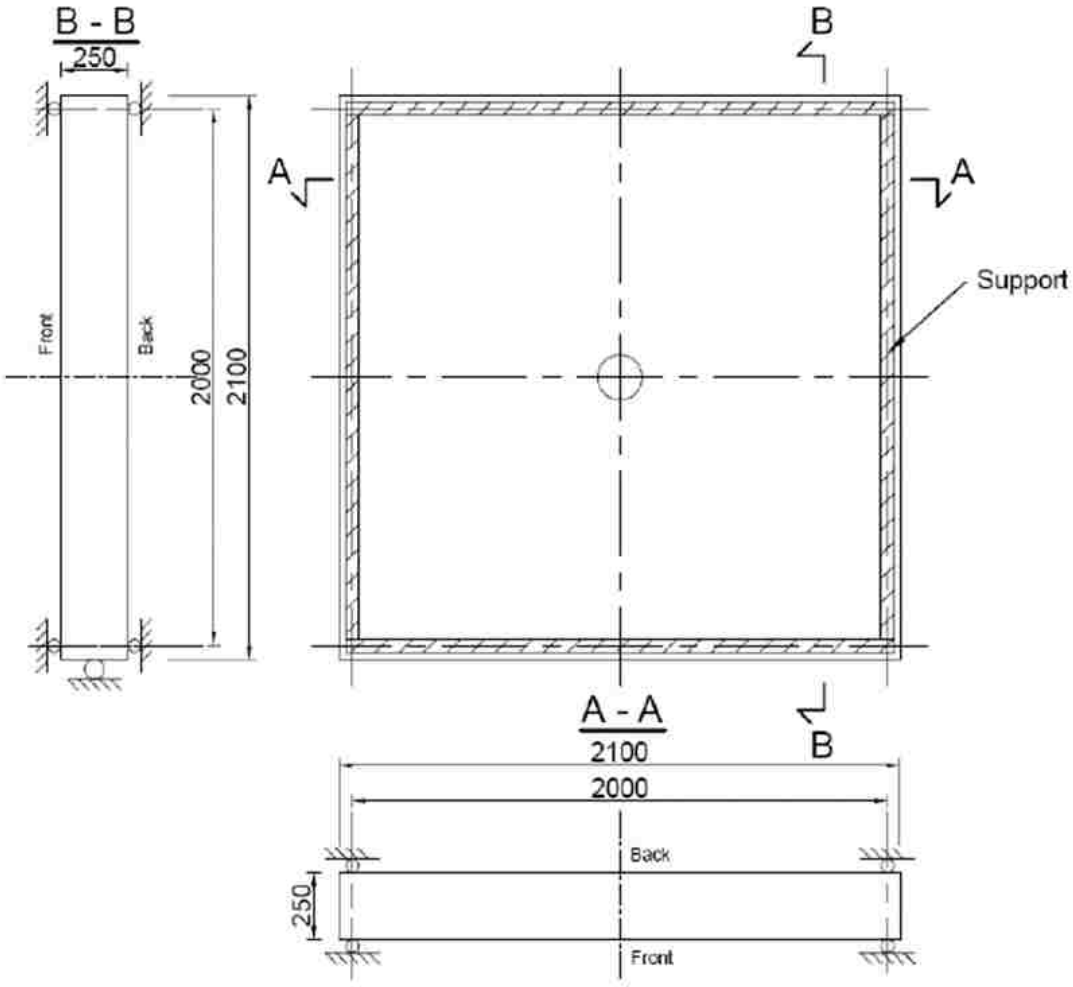

Figure 3.12: IRSN VTT Punching engineering drawing

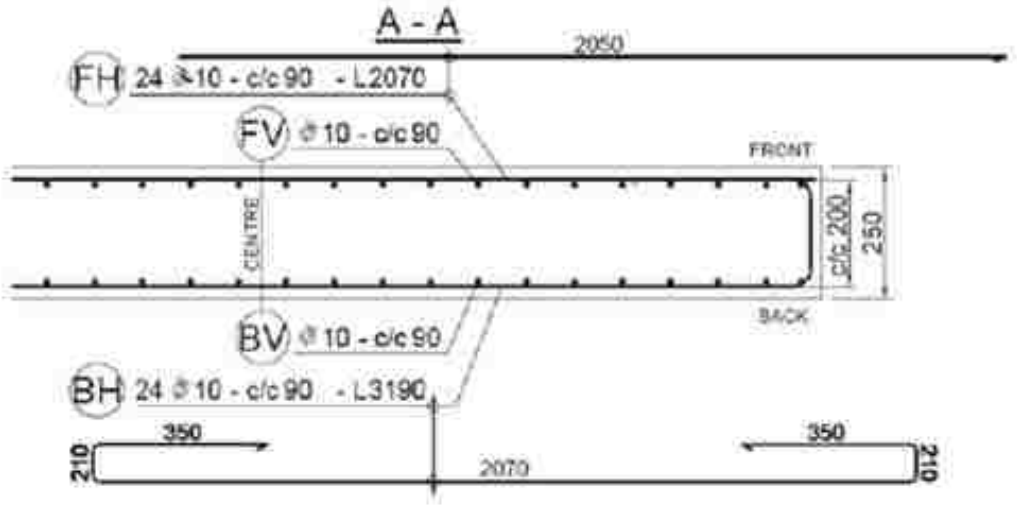

Horizontal cross section A-A of the wall.

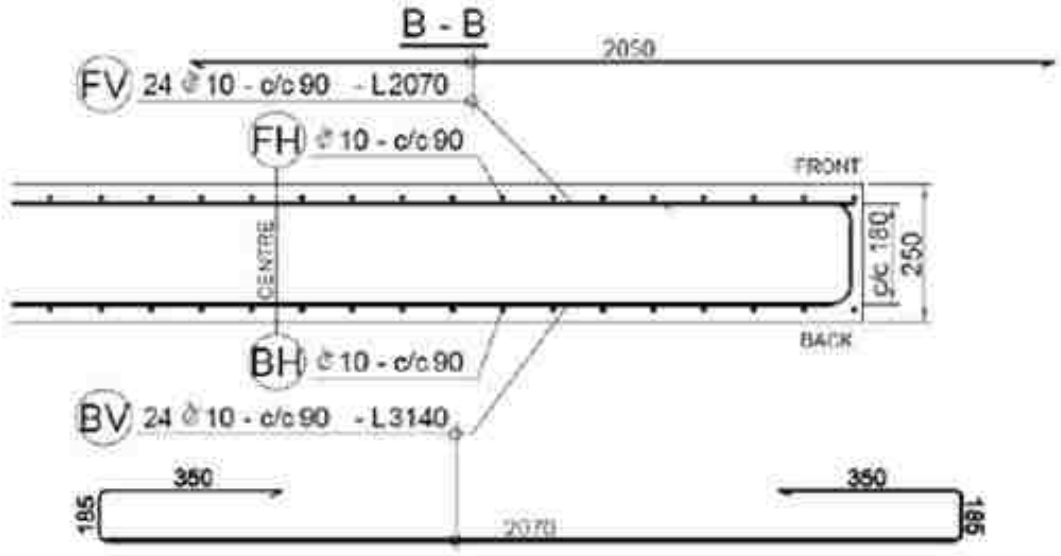

Vertical cross section B-B of the wall.

Figure 3.13: IRSN VTT Punching target cross-section rebar placement

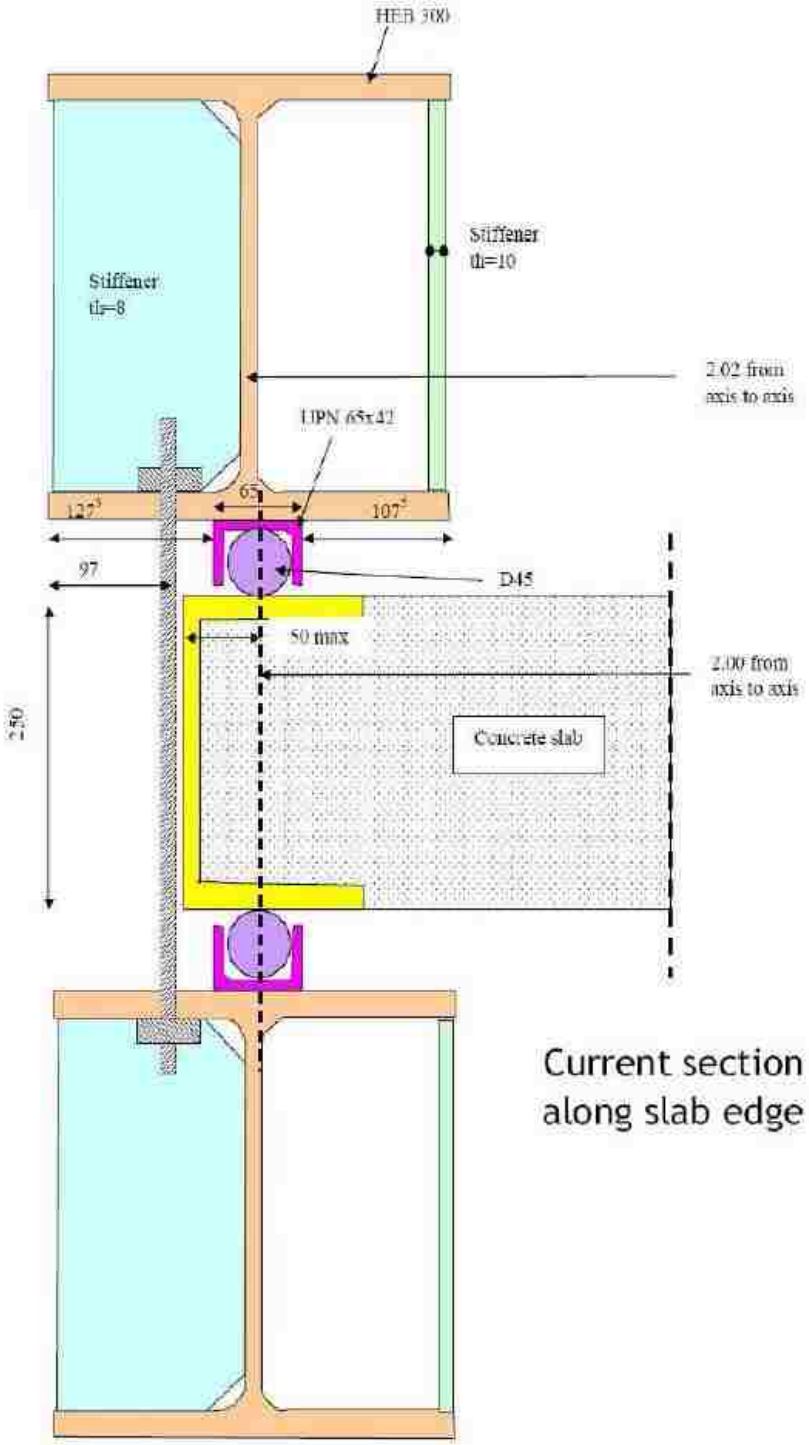

Figure 3.14: IRSN VTT Punching mounting fixture schematic

CAHPTER 4

DEVELOPMENT OF FEM FOR IRSN VTT TESTS

4.1 Introduction

The numerical models that were crafted to recreate the IRIS phase II material data and impact experiments were constructed by selecting adequate material models, designing a mesh and incorporating boundary conditions to produce numerical data that is comparable to the experimental results provided by CSNI. The major simulations explicitly modeled for comparison were the standard concrete cylinder compression tests subjected to varying confinement pressures, IRSN VTT Flexural test and the IRSN VTT Punching test.

4.2 Concrete FEM

Numerous studies conducted on the accuracy of solid continuum elements concluded that tetrahedron elements produce higher stiffness matrix eigenvalues then those produced by hexahedron elements. This demonstrates the superior accuracy of hexahedron elements and their capability to generally deform in a lower strain energy state (Sjaardama et al., 1995). For this reason, all concrete was modeled using hexahedron elements. The first finite element model developed was the standard concrete cylinder that was devised with 8 noded hexahedral elements containing 4 integration points. Two meshes were generated; one to be defined as the coarse mesh and the other defined as the fine mesh, to check for mesh sensitivity between the two constitutive concrete models being investigated. The coarse mesh contained 432 hex elements while the fine mesh contained 27648 elements. A visual comparison between the two meshes can be seen in Figure 4.1. The models were geometrically identical to the standard concrete specimens tested and were also subjected

to the same confining pressures. In order to replicate the testing procedure, boundary conditions were applied to the model including pressurizing the entire element set containing the concrete material model, restricting movement of the bottom surface nodes parallel to the axial direction (z-direction), and applying a negative velocity to the top surface nodes parallel to the axial direction (z-direction). As the top surface begins to move towards the bottom surface, the material begins to see compressive loads with an assigned confinement pressure. The time history response for strain in the axial direction is compared to the reaction force of the bottom surface to generate a uniaxial relationship between the stress and strain of the material models at different confining pressures.

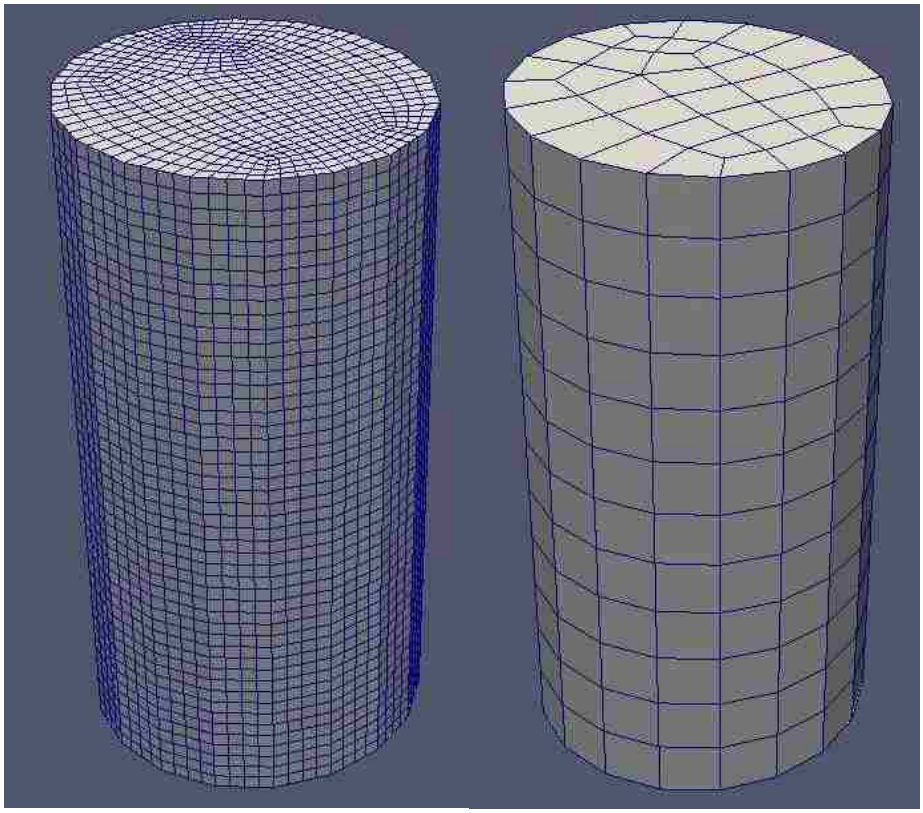

Figure 4.1: Concrete cylinder coarse mesh (right) and fine mesh (left)

4.3 VTT Flexural FEM

The VTT Flexural finite element model incorporated several different material models for every different component in the numerical simulation. The concrete target consisted of 8 noded hexahedral elements containing 4 integration points while the hollow missile was modeled with both hex elements (carbon steel plate) and 4 noded Belytschko-Tsay (BT) shell elements with a 5 point trapezoid integration scheme through the shell thickness (missile tube). BT shells with full integration are capable of mitigating excessive warping generally found with under integrated quad elements, as well as having the ability to generate accurate results with high computational efficiency versus solid elements. This was observed in a finite element study of shells and solid elements used in a crash-box simulation where solid elements displayed higher internal energy compared to shells during deformation. The computational times also differentiate drastically for the fully integrated element types used in the simulation. A fully integrated hexahedron element simulation, with proper resolution through the thickness, took 30 times longer to complete and yielded stiffer results than its shell counterpart (Bari, 2015). For this reason the missile was modeled with shells as opposed to hex elements. The hollow stainless steel tube of the projectile is attached to the carbon steel plate at the tail end with a multipoint contact where the nodes of the carbon steel plate are fixed to the face of the elements of the hollow missile base. Figure 4.2 and Figure 4.3 displays the mesh of the concrete target and soft missile respectively.

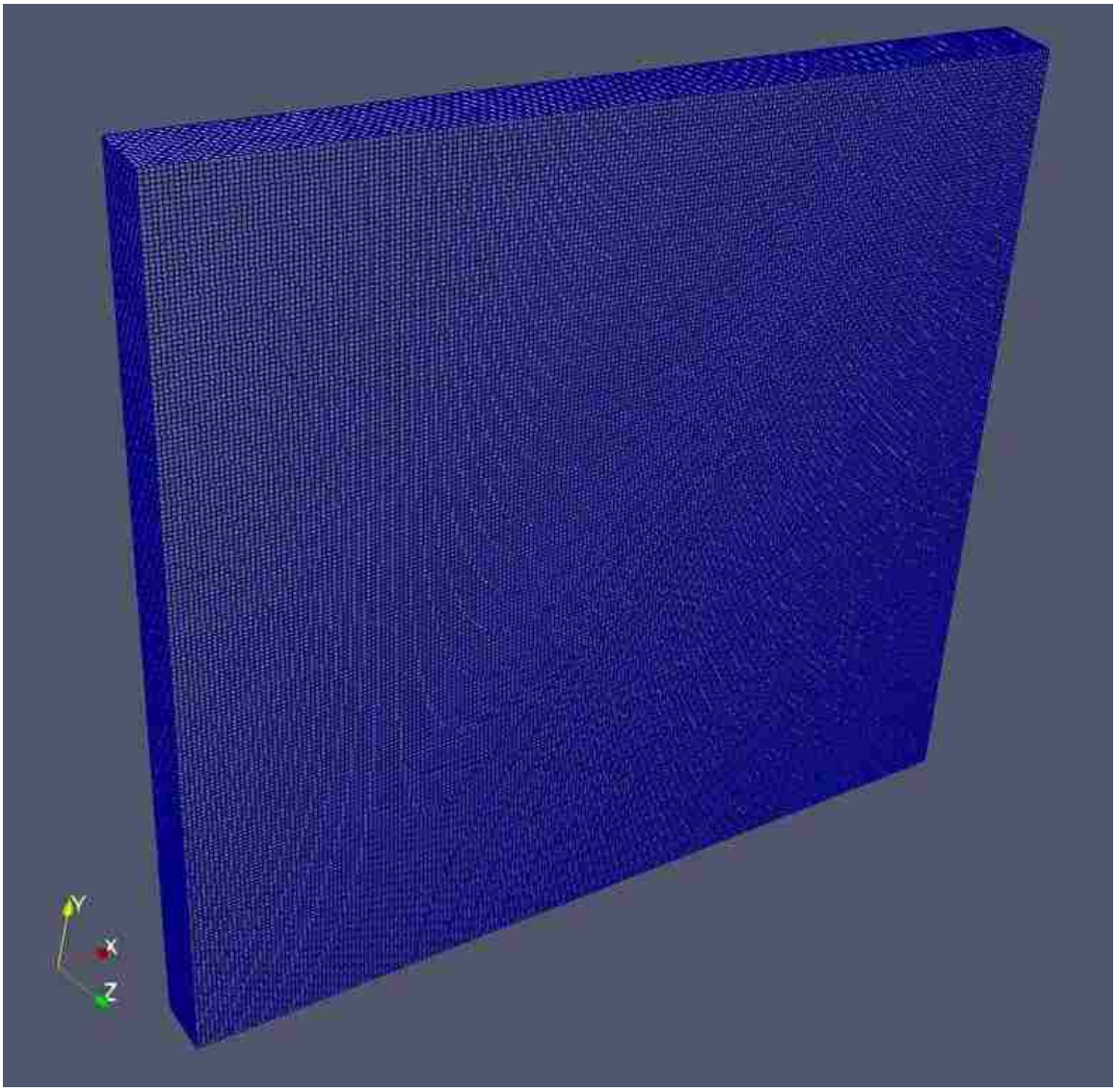

Figure 4.2: VTT Flexural concrete target mesh

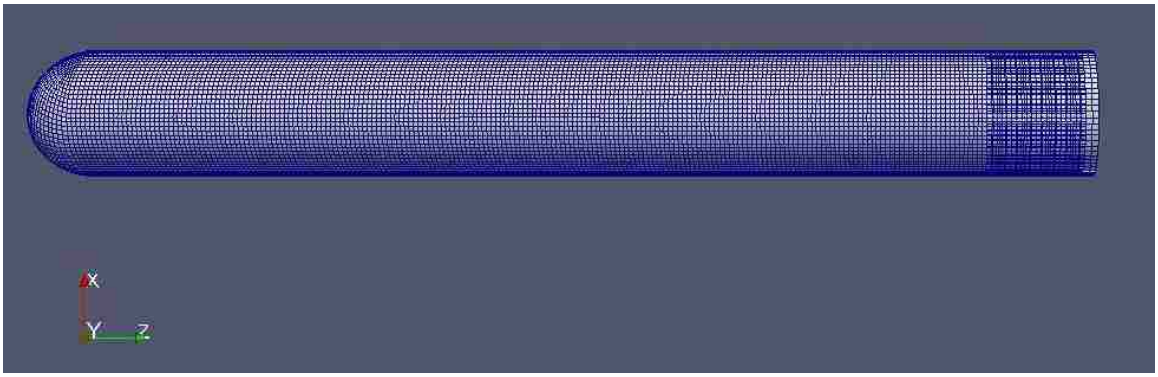

Figure 4.3: VTT Flexural hollow missile mesh

In addition to the concrete target and hollow missile, the reinforcement rebar in the VTT Flexural simulation was modeled using beam elements to minimize computing time. This method allows the rebar to be discretized with linear beam elements capable of capturing axial and bending responses in the simulation accurately. This approach also requires an embedded modeling technique to be utilized. The embedded model acknowledges two different element sets and constrains the nodes of one element set to the elements of the other. In this case, the nodes of the beam elements are attached to the hex elements of the concrete target. This modeling technique doesn't account for mass differences in the coupled section where rebar beam elements and concrete hex elements coincide, therefore an adjustment to the concrete density must be made in order to obtain the correct transfer of energy between the missile and concrete target. Including the reinforcement as an embedded sub model allows for a simpler simulation that mitigates problematic issues that arise when explicitly modeling small rebar reinforcement. When the small rebar is explicitly modeled, contact definitions must be assigned to determine the correct delamination behavior that occurs between the coincident nodes of rebar and concrete. If the size of the rebar is much smaller than the concrete target, significantly smaller elements must be used to capture the bending behavior of the rebar than what is used for the concrete. This discontinuity between elements makes meshing with a high aspect ratio nearly impossible when reinforcement traverses in multiple directions with little spacing between rebar. Figure 4.4 depicts the curves that are representative of the reinforcement in the VTT Flexural simulation.

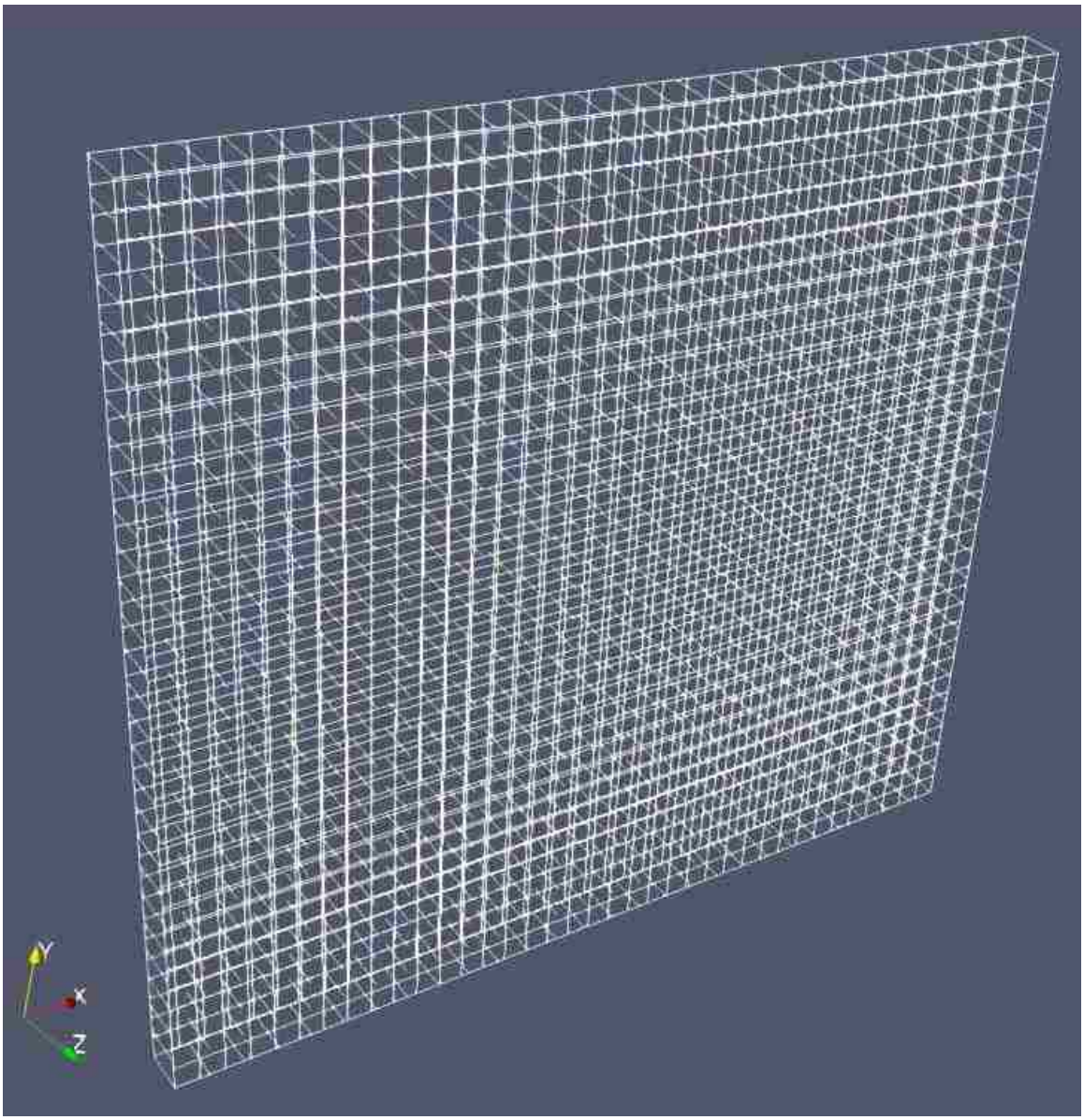

Figure 4.4: VTT Flexural reinforcement

Every component modeled in the VTT Flexural simulation was designated a proper material model. Limitations in the accuracy of the material models were present for the rebar since the software used to run the simulations (SIERRA Solid Mechanics) only supports a bilinear elastic plastic material model. The hollow missile used a multilinear elastic plastic material model which enables the user the ability to prescribe an isotropic hardening behavior that is similar to experimental data. More specifically, the multilinear

elastic plastic material model takes true stress and true strain inputs to determine the hardening behavior of the model. Table 4.1 gives the material models associated with every component in the VTT Flexural simulation and Table 4.2 gives the number of elements used for every component.

Table 4.1: VTT Flexural component material models

VTT Flexural Component	Material Model
Concrete Target	HJC/JH2
Missile T. (Tube)	Multilinear Elastic Plastic
Missile P. (Plate)	Bilinear Elastic Plastic
Rebar	Bilinear Elastic Plastic

Table 4.2: VTT Flexural component elements

VTT Flexural Component	Element Count
Concrete Target (8-noded Hex Elements)	640000
Missile T. (4-noded Shell Elements)	20608
Missile P. (8-noded Hex Elements)	2544
Rebar (2-noded Beam Elements)	19424

During the creation and calibration process of the VTT Flexural model, the two underlying parameters that truly governed the behavior of the flexural response of the target were the boundary conditions set on the concrete target and the formulation of the missile. Boundary conditions were applied to best represent the experimental conditions of the VTT Flexural test. The element set that composes the entire hollow missile was given an initial

velocity boundary condition of 110 m/s. As previously mentioned, the rebar was embedded in the concrete structure using beam elements while the concrete structure was given a modified simply supported boundary condition. The boundary condition applied on the concrete was determined after several model iterations which are fully explained in the calibration results in the following chapter. Several model iterations for the hollow missile were also made since the buckling and folding effects of thin walled steel tubes are mesh sensitive.

4.4 VTT Punching FEM

Similar to the VTT flexural finite element model, the punching model consisted of different material models for every component in the numerical simulation. The thick concrete slab consisted of 8 noded hexahedral elements containing 4 integration points as did the majority of the solid missile. The steel lined concrete missile was modeled using primarily hexahedral elements with the exception of the 20mm front domed portion of the missile which was modeled using tetrahedral elements due to poor mesh quality. For unique geometries that incorporate oblique shapes, chamfers, or small rounded features, generating a hexahedral based mesh can be difficult or impossible to acquire. While the VTT punching model was being developed, negative Jacobians were being produced on the front domed portion of the solid missile during the meshing process. Since an element's Jacobian matrix relates to the mesh quality of an element, a negative Jacobian identifies an inverted element and will prevent simulations to run. For this reason tetrahedral elements were substituted in the poor mesh quality region of the solid missile to refine the mesh quality to a suitable standard capable of running. An embedded model approach was also

taken for the punching simulation in order to model the rebar reinforcement with beam elements.

The concrete slab for the VTT punching model was given the same boundary condition as the flexural model with a node set representing a simply supported BC. The solid missile element set was prescribed an initial velocity of 136m/s for the hard impact. Figure 4.5, Figure 4.6, and Figure 4.7 displays the mesh of the concrete slab, mesh of the solid missile, and the rebar reinforcement orientation.

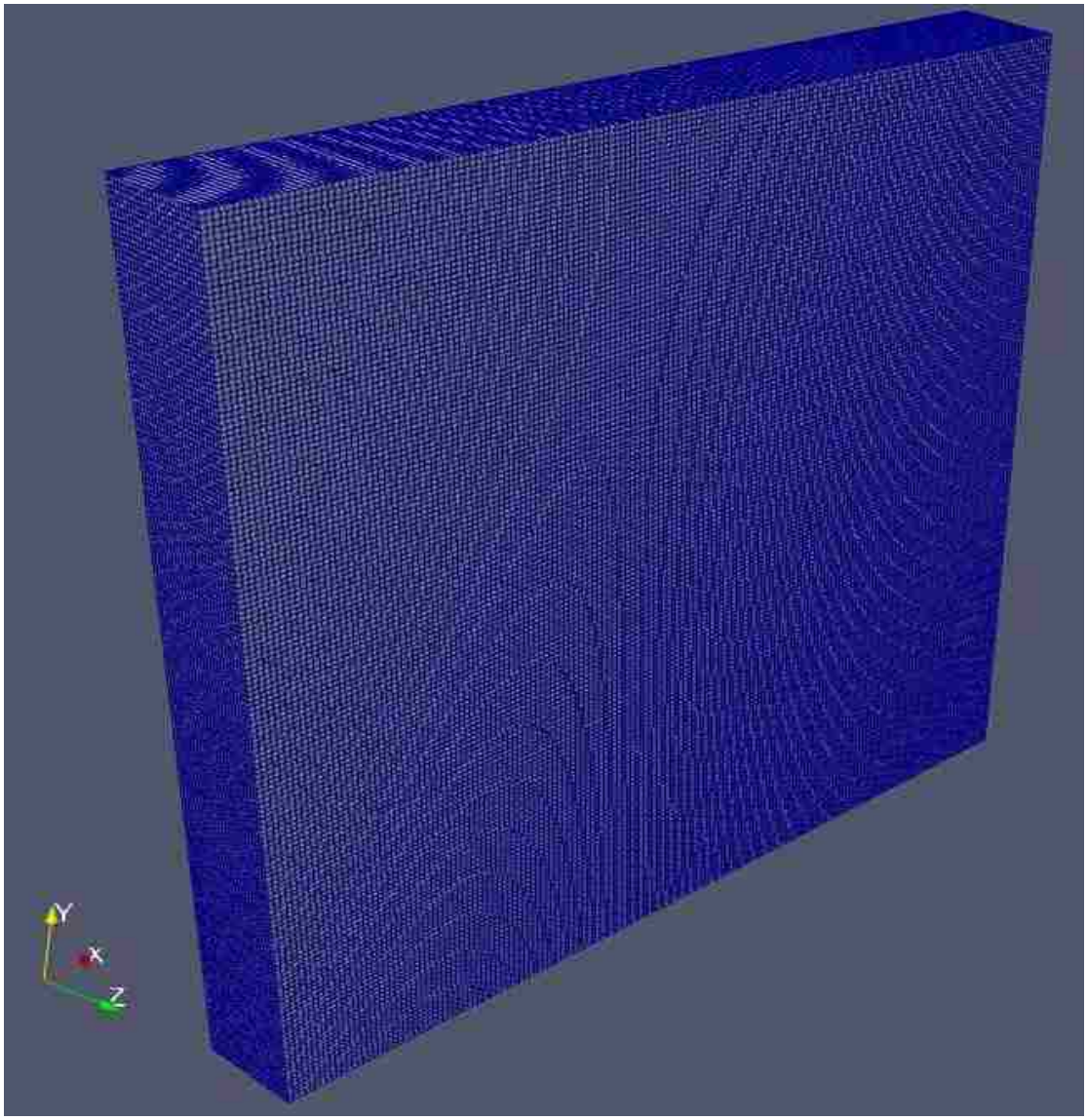

Figure 4.5: VTT Flexural concrete target mesh

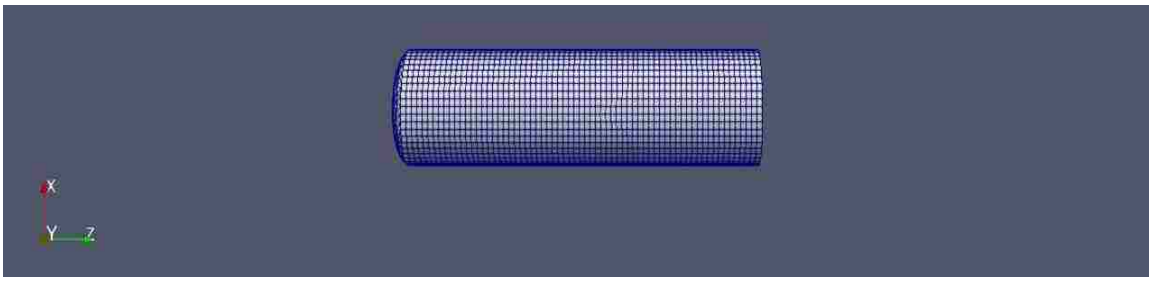

Figure 4.6: VTT Punching solid missile mesh

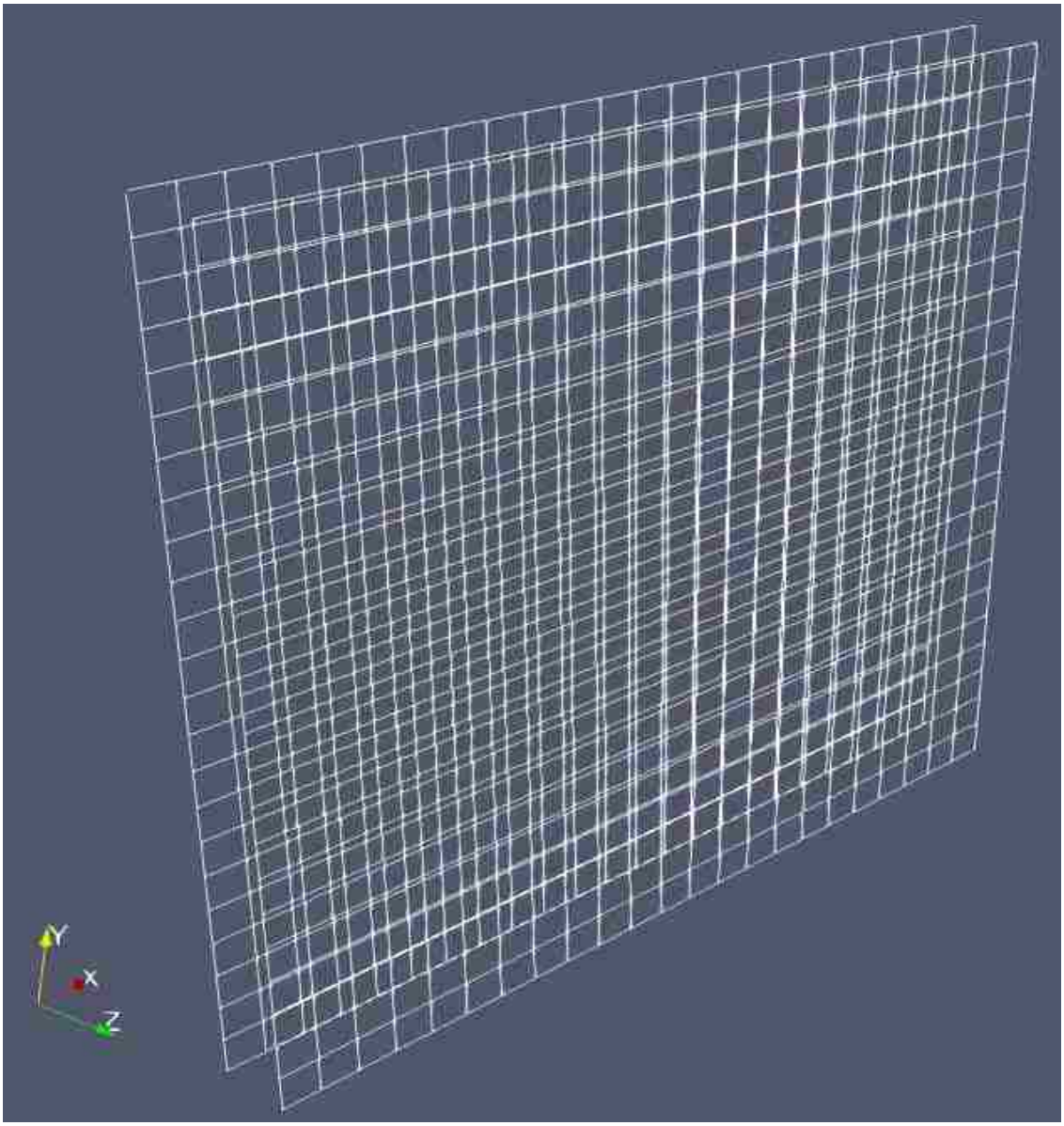

Figure 4.7: VTT Punching reinforcement

The final material model designation and element type/count for the VTT Punching simulation can be seen in Table 4.3 and Table 4.4 respectively.

Table 4.3: VTT Punching component material model

VTT Punching Component	Material Model
Concrete Target	HJC/JH2
Missile S. (Steel liner)	Multilinear Elastic Plastic
Missile C. (Concrete)	HJC/JH2
Rebar	Bilinear Elastic Plastic

Table 4.4: VTT Punching component element count

VTT Punching Component	Element Count
Concrete Target (8-noded Hex Elements)	677376
Missile S. (4-noded Tet Elements) Missile S. (8-noded Hex Elements)	816 2319
Missile C. (8-noded Hex Elements)	8901
Rebar (2-noded Beam Elements)	19776

CAHPTER 5

COMPARISON OF NUMERICAL RESULTS

5.1 Introduction

The calibration process and results, from all numerical simulations, presented in this chapter are used to evaluate the effectiveness of the Johnson-Holmquist series material models in their ability to represent the behavior concrete undergoes during ballistic impacts. All the finite element models developed for the IRSN VTT tests were conducted using an explicit dynamics analysis since nonlinearities introduced during loading conditions can cause instability issues for implicit solvers. Three main series of computational runs were compared to experimental data to investigate the effectiveness of the Johnson-Holmquist material model's ability to simulate concrete in dynamic loading conditions. The first series of computational runs looked at the uniaxial behavior of concrete cylinders subjected to compression and their dependency on confinement pressures. The second series of runs investigated the global flexural response of a concrete structure impacted by a soft missile. The last series of runs explored the localized damage outputted by impacting a thicker concrete slab with a solid missile. The final material properties for all constitutive components for every model were obtained from experimental data. Those parameters not specifically obtained from experimental data were derived from a comprehensive literature search in conjunction with a calibration process.

5.2 Concrete Compression

Similar to the standard cylindrical concrete specimens tested by the ISRN, five numerical simulations were run for both the JHC and JH2 material models in Sierra. All concrete cylinder compression simulations were ran using a course and fine mesh and no significant difference was observed in the output between the two meshes used.Although some material data was directly attained from test results such as crushing strength, density, and young's modulus, other parameters that control the damage behavior of the models needed to be inferred through literature review and experimental results. Figure 5.1 shows the calibrated results for both material models from the unconfined compression test simulation on the concrete cylinder versus the experimental results.

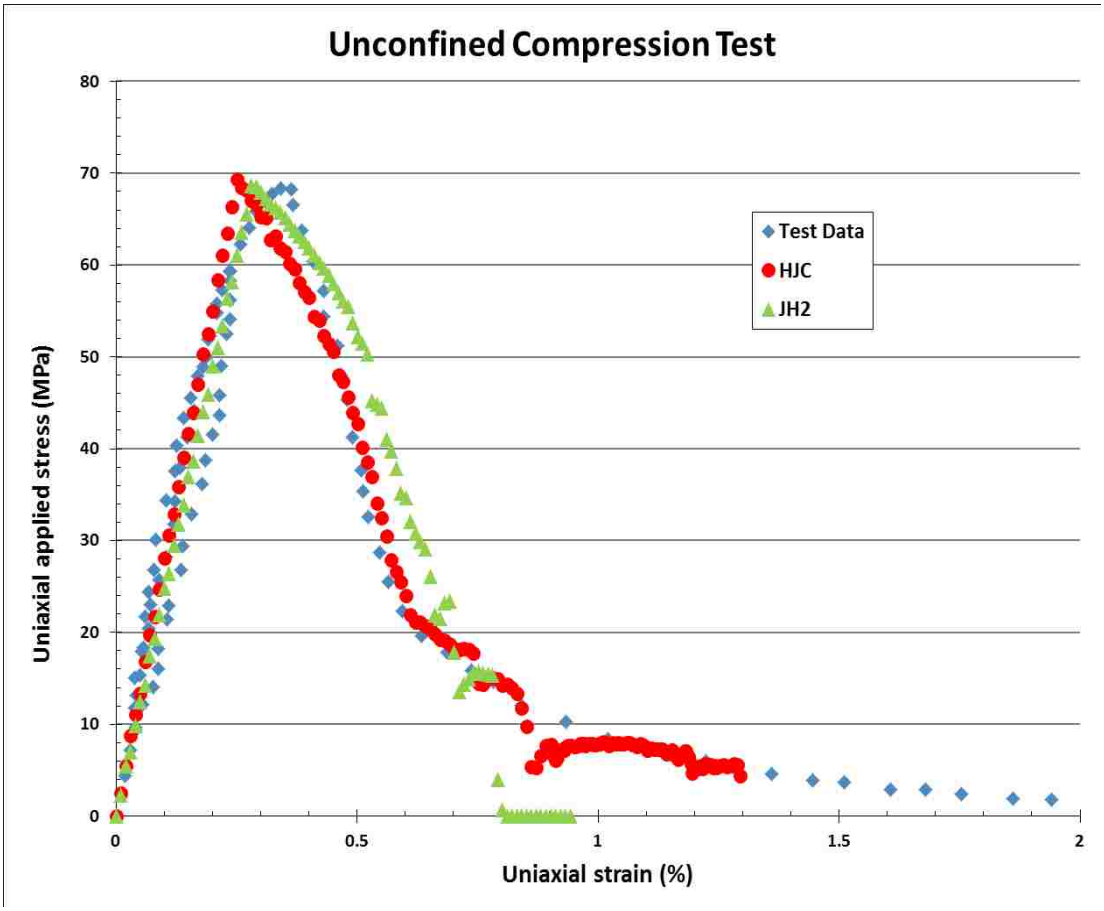

Figure 5.1: Concrete unconfined compression

For the unconfined compression test simulation, both material models were able to capture the material response fairly adequately. However, this changes for the confined compression tests which rely on the confining pressure to generate the uniaxial stress-strain relationship. The HJC material model shows more precision than the JH2 material model when simulating the triaxial compression test at various confining pressures. This difference can be attributed to the HJC's pressure-volumetric relationship that encompasses a bilinear elastic-crushing region with a cubic locking region. While the HJC has more variability in defining the pressure-volumetric relationship, the JH2 solely has a cubic function to describe the same relationship with recoverable volumetric deformation. This subtle difference is the underlying reason why the HJC is able to simulate the triaxial compression data better than the JH2 model. Figure 5.2 through Figure 5.5 display the simulation results of both material models in comparison to the experimental triaxial compression data for increasing confinement pressures.

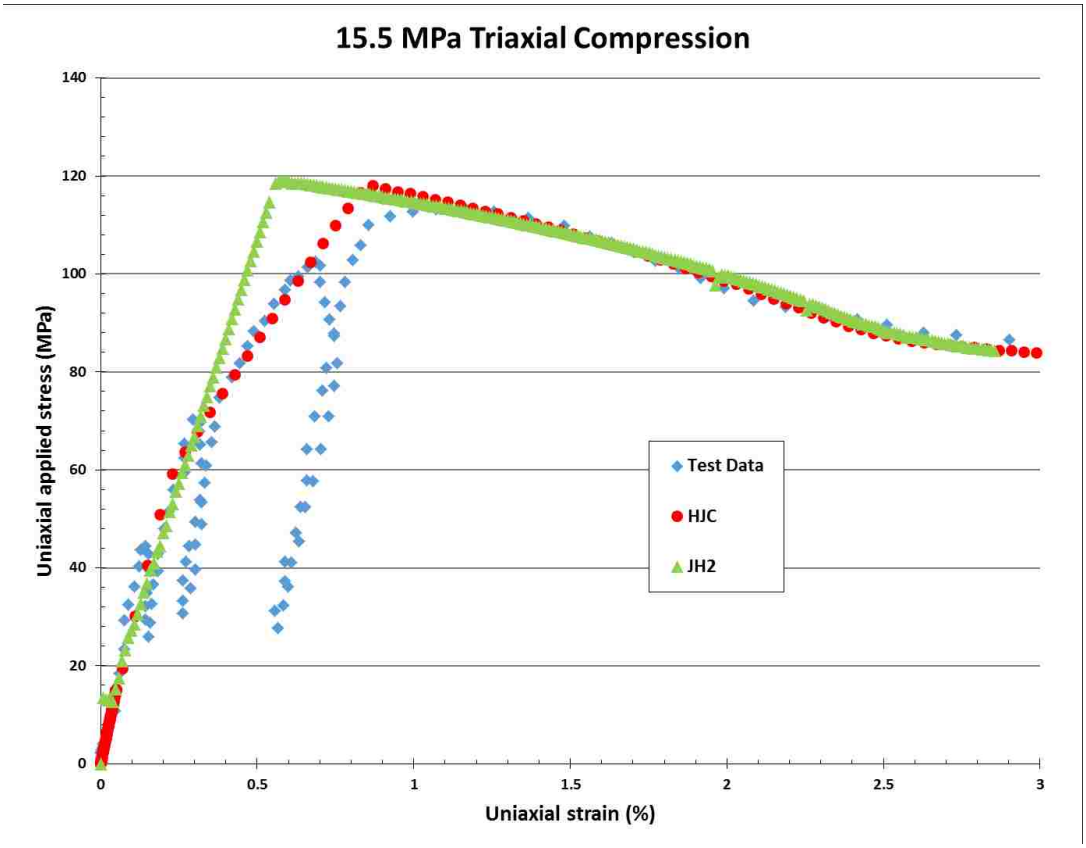

Figure 5.2: Concrete triaxial compression (15.5 MPa)

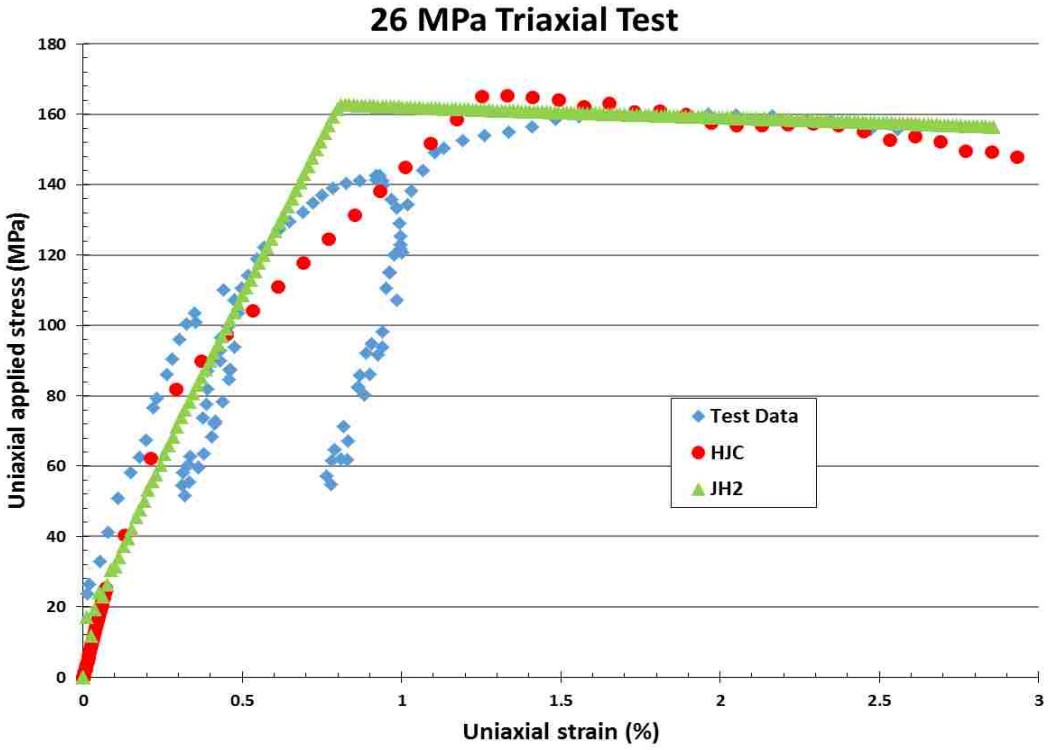

Figure 5.3: Concrete triaxial compression (26 MPa)

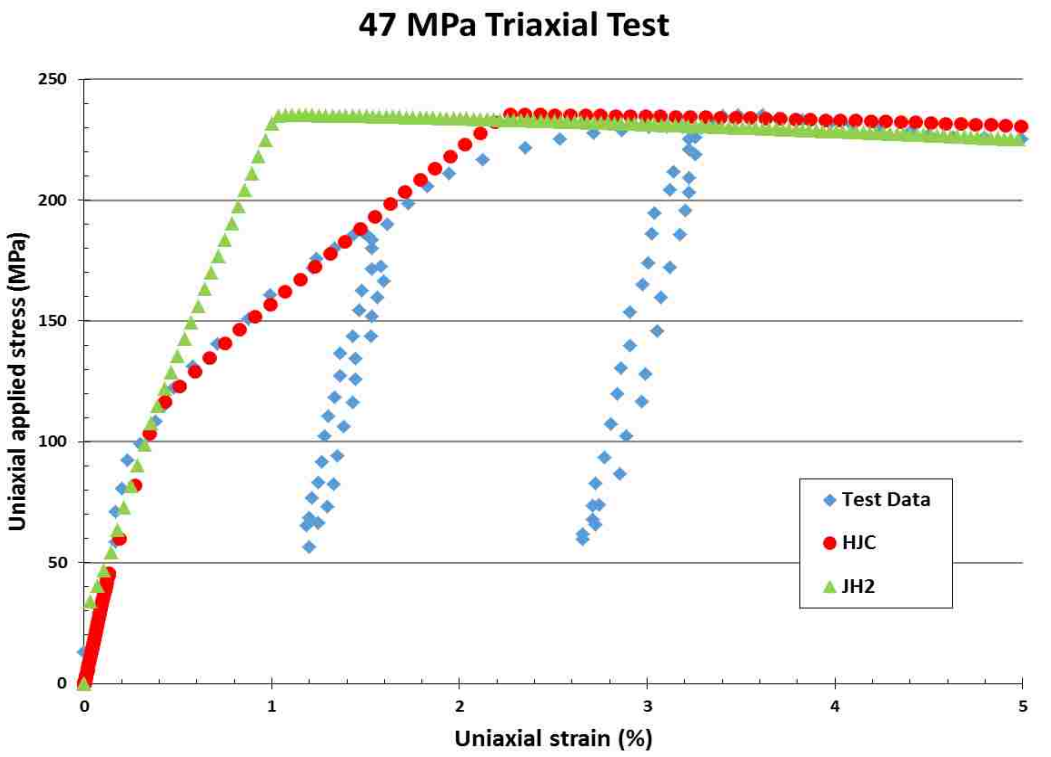

Figure 5.4: Concrete triaxial compression (47 MPa)

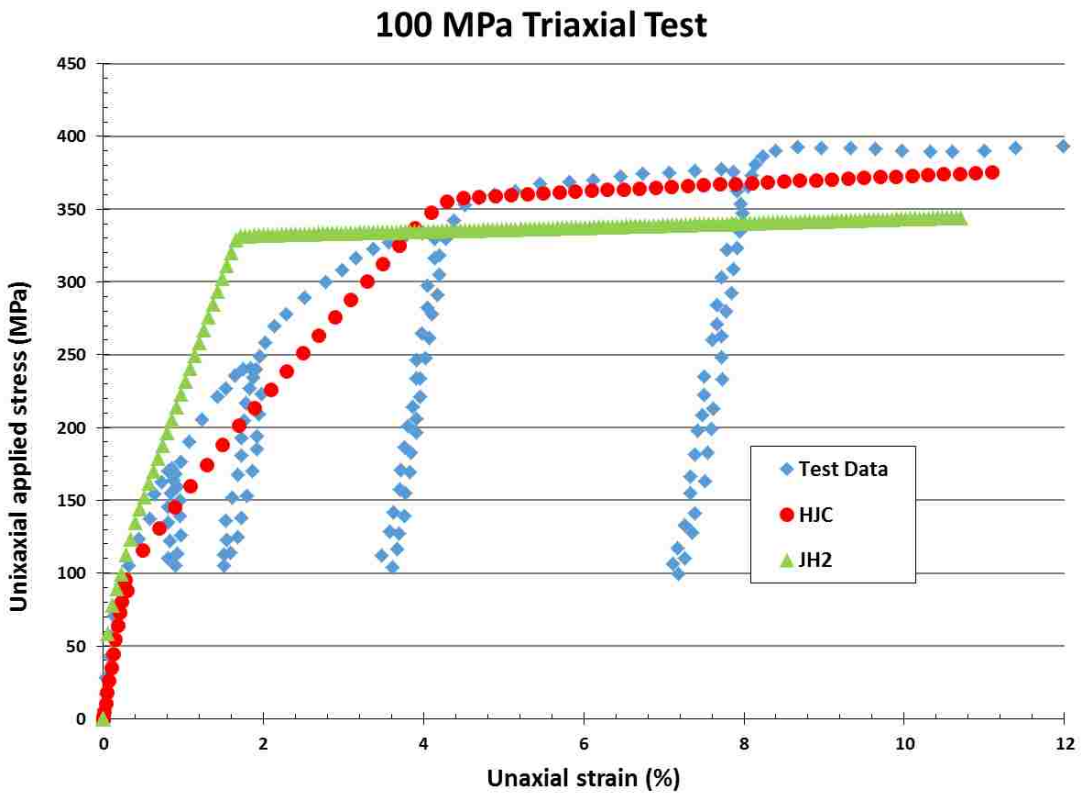

Figure 5.5: Concrete triaxial compression (100 MPa)

Some of the calibrated parameters derived from the concrete compression test simulation for the HJC and JH2 material models are listed in Table 5.1 and Table 5.2 respectively.

Table 5.1: HJC material parameters

Material Property	Unit	Value
Initial density	kg/m^3	2255.6
Modulus of elasticity	GPa	29.67
Poisson's ratio		0.223
Cohesive strength coeff.		.053
Pressure hardening coeff.		1.45
Compressive strength	MPa	66.93
Tensile strength	MPa	4.04
Damage constant 1		0.07
Damage constant 2		1
Crush pressure	MPa	35
Crush volumetric strain		0.002885
Lock pressure	GPa	1
Lock volumetric strain		0.1881
Bulk modulus	GPa	17
Pressure constant 1	GPa	17.85
Minimum fracture strain		0.01

Table 5.2: JH2 material parameters

Material Property	Unit	Value
Initial density	kg/m^3	2255.6
Modulus of elasticity	GPa	29.67
Poisson's ratio		0.223
Intact strength coeff.		1.06
Strength exponent coeff.		0.0001
Fracture strength coeff.		0.7
Frac. strength exponent coeff.		0.65
Damage constant 1		.05
Damage constant 2		1
HEL	MPa	90
Bulk modulus	GPa	17
Max tensile pressure	MPa	4.04
Minimum fracture strain		.01

Overall, both material models were able to effectively represent the concrete compression data for the unconfined compression case as well as for the numerous confined compression cases. This indicates the material model's ability to successfully simulate the mechanistic behavior of a quasi-statically loaded concrete specimen.

5.3 VTT Flexural

The second stage in the validation process of the material models was observing the dynamic response generated by the reinforced concrete structure. Since the material models

were calibrated using cylindrical concrete compression data, the flexural simulation was conducted in order to examine the models behavior during impulse loading conditions. During a soft missile impact, the kinetic energy from a flying projectile produces a pressurized wave onto the structure it impacts, ultimately inducing global damage on the structure. The VTT Flexural simulation aimed to capture the material models ability to characterize the global damage and flexural response produced in the actual experiment.

5.3.1 Governing Parameters

After the concrete calibration, the VTT Flexural model was formed to geometrically represent the VTT experiment. The reinforced concrete structure and embedded reinforcement were finely meshed to capture bending of the slab and rebar. Since the deflection of the concrete slab is reliant on the rate at which energy is transferred from the missile, a mesh sensitivity study was conducted. This was done to ensure mesh convergence is acquired and that deformation of the hollow missile is controlled by the material model and not poor resolution at the site of deformation when the hollow missile begins to buckle.

Four missiles with different mesh densities were impacted on a rigid surface made of shell elements and the sum of the resulting reaction forces at the nodes of the rigid surface were plotted against time. All missiles were prescribed the same multilinear elastic plastic material model that was calibrated for the material EN 1.4432. The mesh densities chosen were 1000, 4000, 20000, and 85000 shell elements per missile. Figure 5.6 and Figure 5.7 portray the missile with lowest and highest mesh densities respectively.

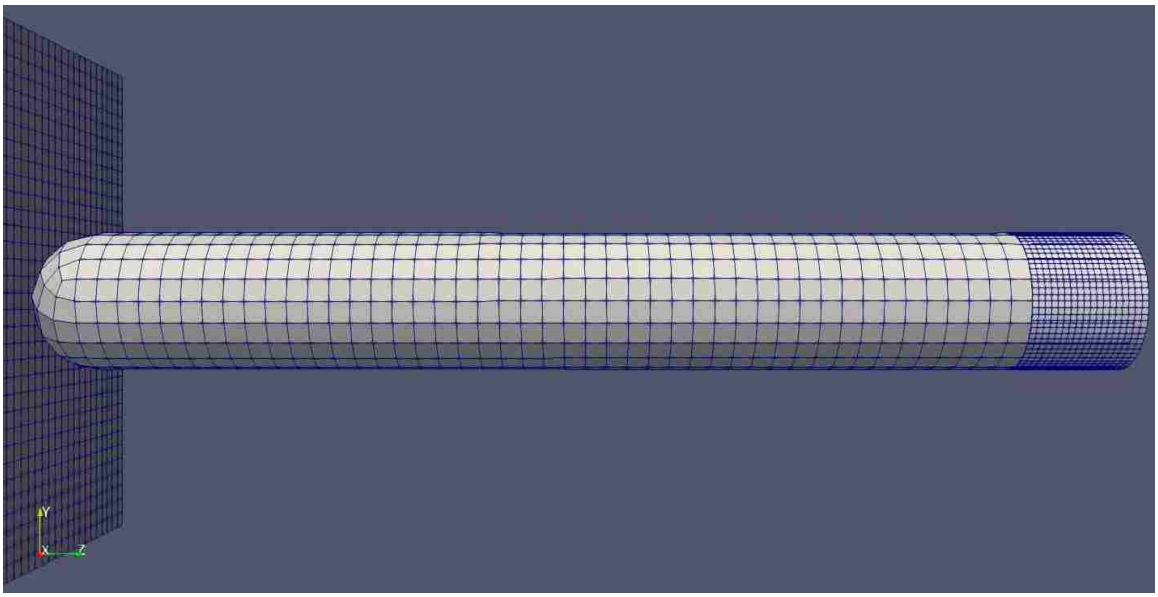

Figure 5.6: Coarse missile mesh (1000 elements)

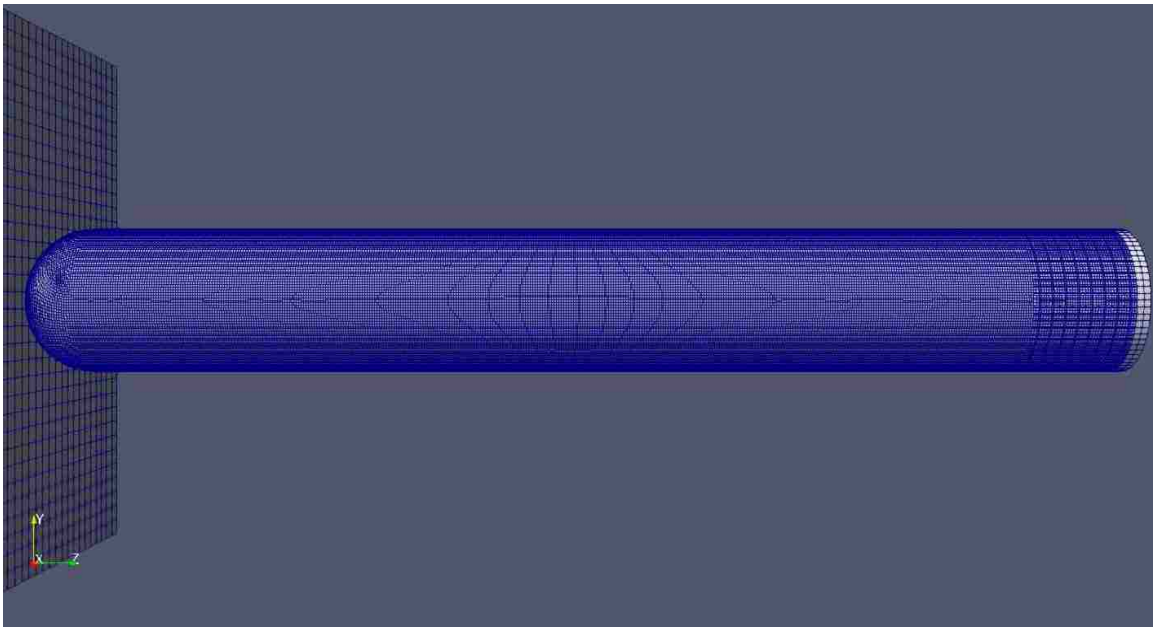

Figure 5.7: Fine missile mesh (85,000 elements)

The outputs collected from each run show a general trend of convergence with increasing mesh refinement of the missile and can be seen in Figure 5.8. However, Figure 5.9 displays the computational cost associated with having a higher mesh refinement.

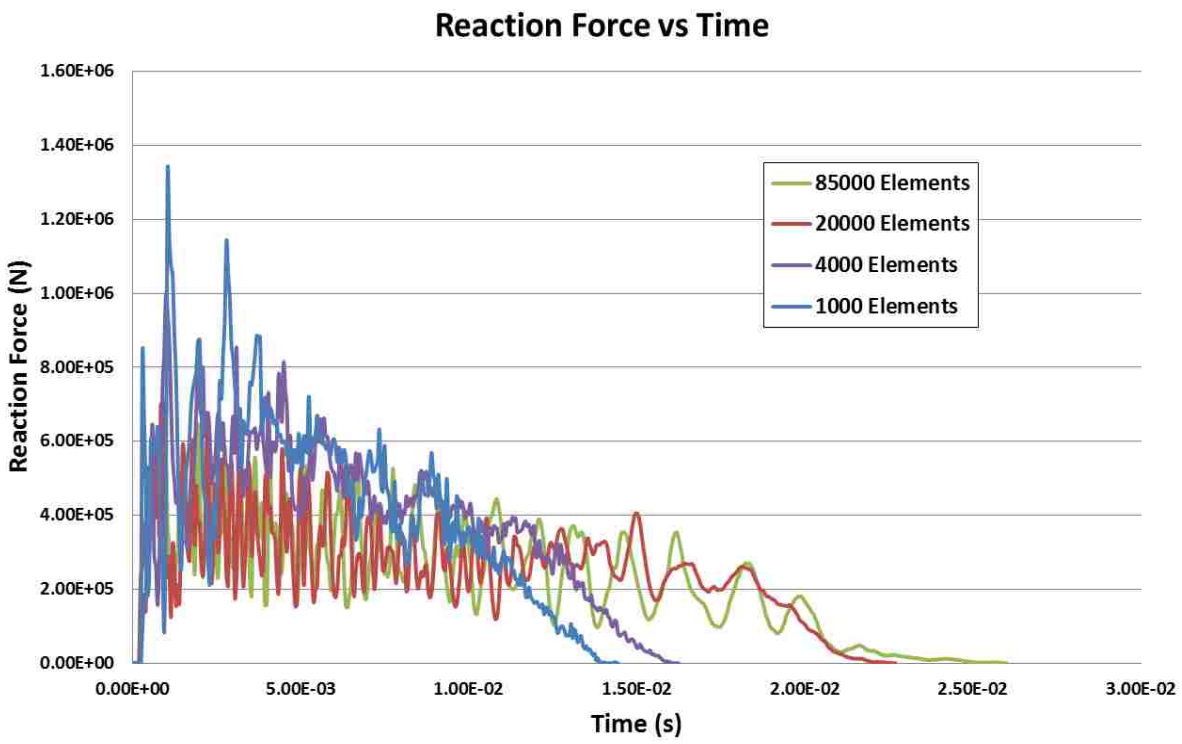

Figure 5.8: Nodal reaction force caused by missile with different mesh densities

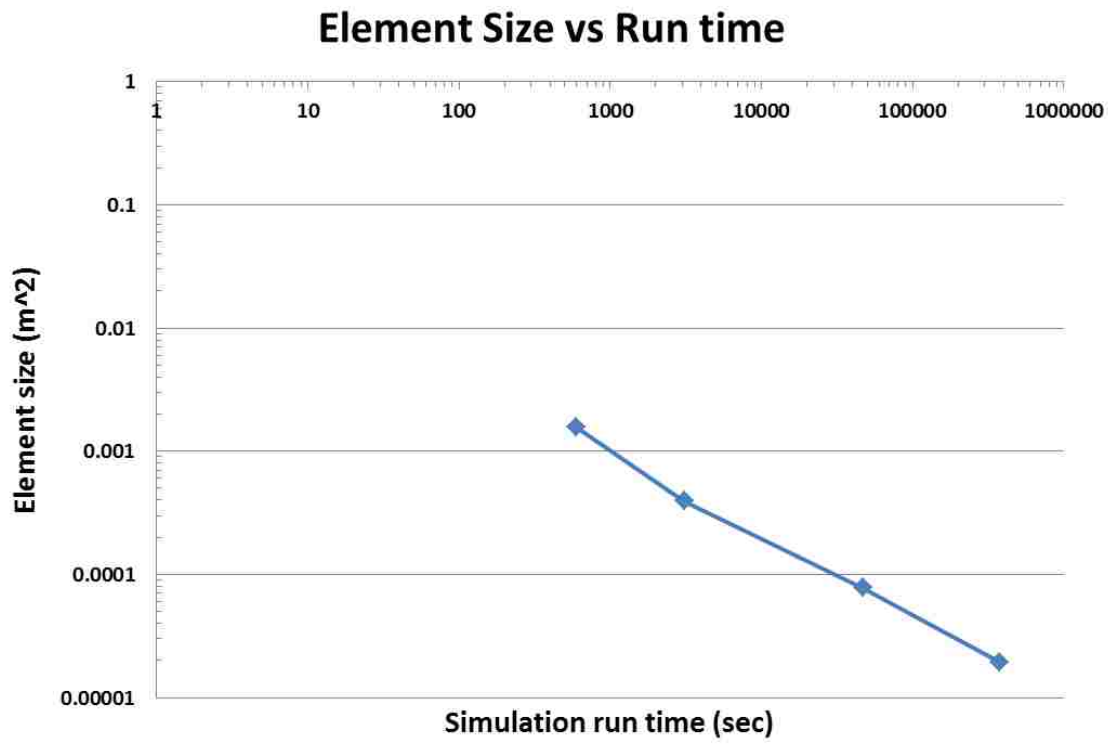

Figure 5.9: Simulation run time for missile with different element sizes

Since the mesh sensitivity study showed mesh convergence for a mesh density around 20000 elements with little benefit for higher densities with considerably longer run times, 20000 elements was chosen as the final mesh density to run the VTT flexural simulation. Mesh convergence was determined by analyzing the average reaction force versus time and the duration for which the reaction force approaches zero.

Along with deformable hollow missile, the second most important parameter that governs the response of the structure is the boundary condition. The simply supported boundary condition applied on the VTT Flexural model was developed to mimic the behavior of the mounting apparatus used to hold the reinforced concrete slab. Several model iterations were made with varying simply supported boundary conditions. These iterations consisted of explicitly modeled rollers with different contact formulations and node set movement restriction on the front and rear surface of the concrete slab. The final boundary condition can be seen highlighted around the concrete perimeter in Figure 5.10.

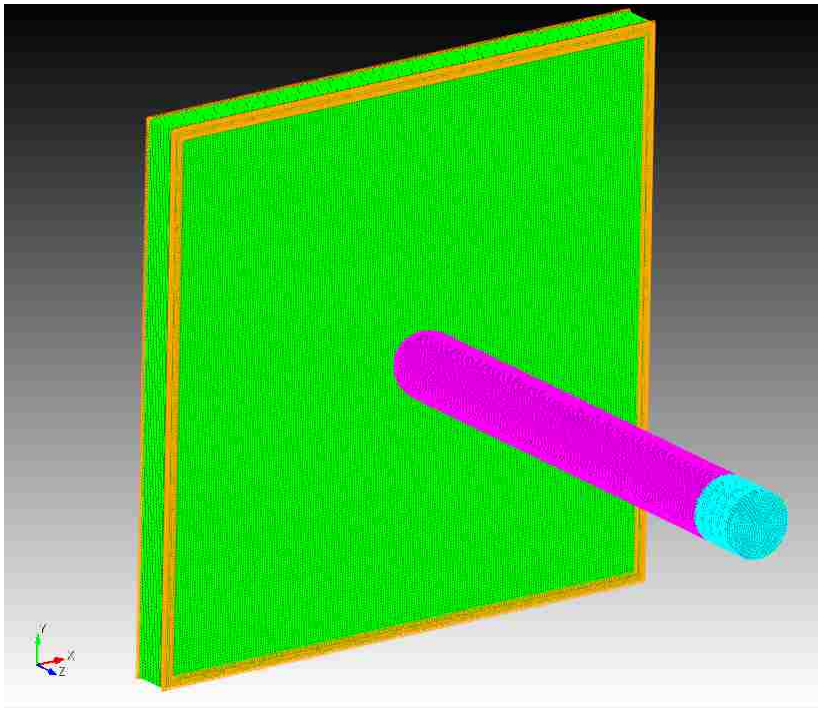

Figure 5.10: VTT Flexural simply supported boundary condition

The boundary conditions tested were deemed realistic or unrealistic from the amount of damage the hollow missile imparted on the structure and the flexural response of the structure. The boundary condition selected is representative of a contact patch on both the front and rear surface of the concrete slab made with a node set. A span of four nodes in from the edges around the entire perimeter of the slab was placed in a node set and translation in the z-direction was restricted. The number of nodes that span from the edge was fairly important since the inclusion of too many nodes yielded a structure that was too stiff and too few nodes would produce a soft mid-region that would allow penetration from the soft missile.

5.3.2 Numerical Dynamic response

During the VTT Flexural experiment, displacement transducers and strain gauges were utilized to collect data to quantify the dynamic behavior of the structure imparted by the soft missile impact. The data compiled from the VTT Flexural experiment included the displacements on the rear surface of the reinforced concrete slab and rebar strains from the embedded reinforcement which were shown in Figure 3.9 and Figure 3.10, respectively. The final VTT Flexural model, with calibrated material models for all the constitutive components, was run using an explicit analysis for both concrete models. The input deck created to run the simulation also incorporated an output section which would accumulate information of elements at specified locations. This was used to amass time dependent numerical data that would be compared with the experimental data for the soft missile impact scenario. Figure 5.11 through Figure 5.15 present the comparison of numerical and experimental data of the out of plane displacement for the rear wall locations W1 through W5, respectively.

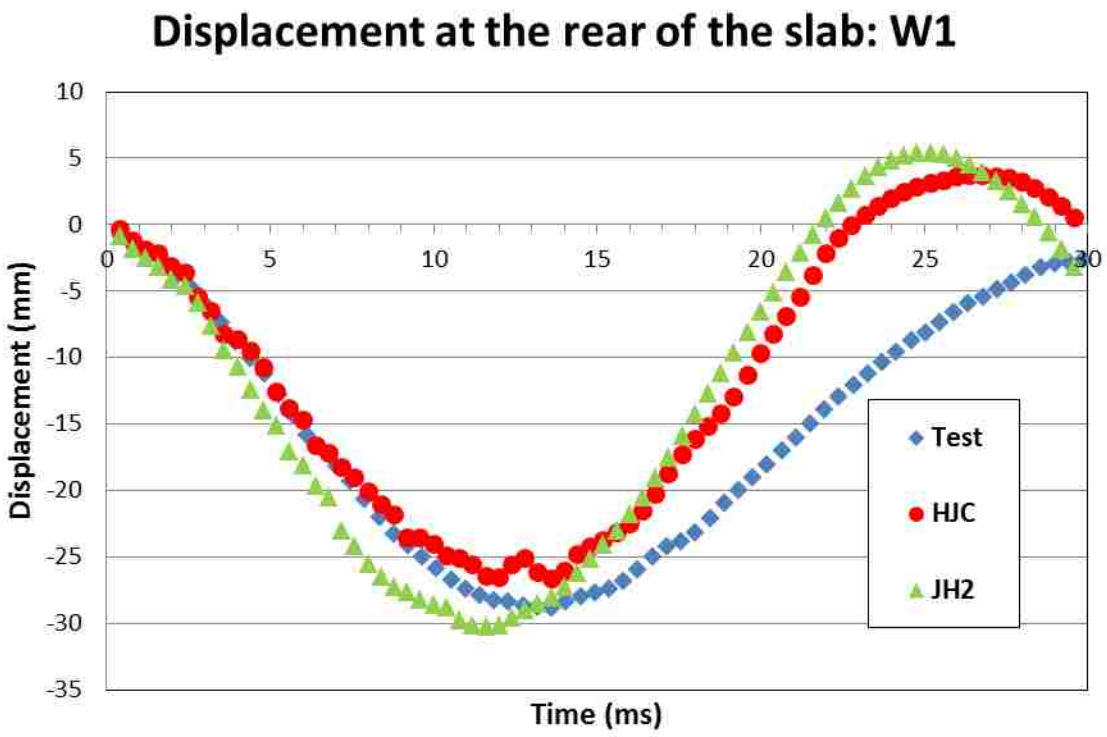

Figure 5.11: Displacement of location W1

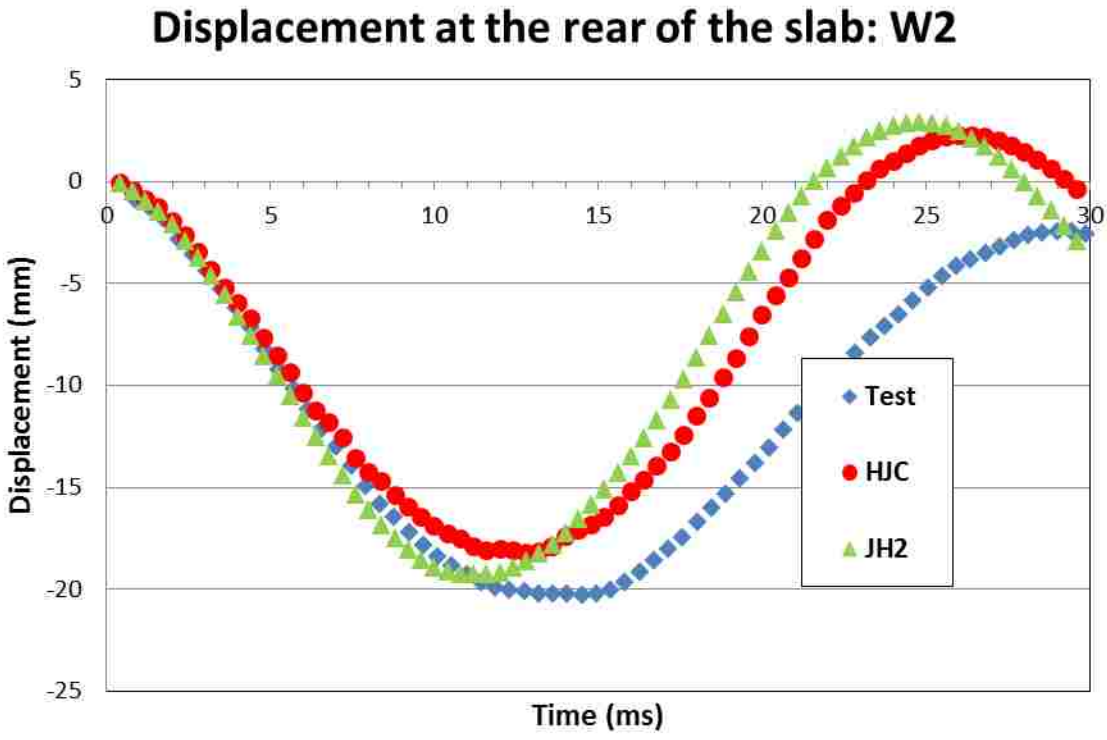

Figure 5.12: Displacement of location W2

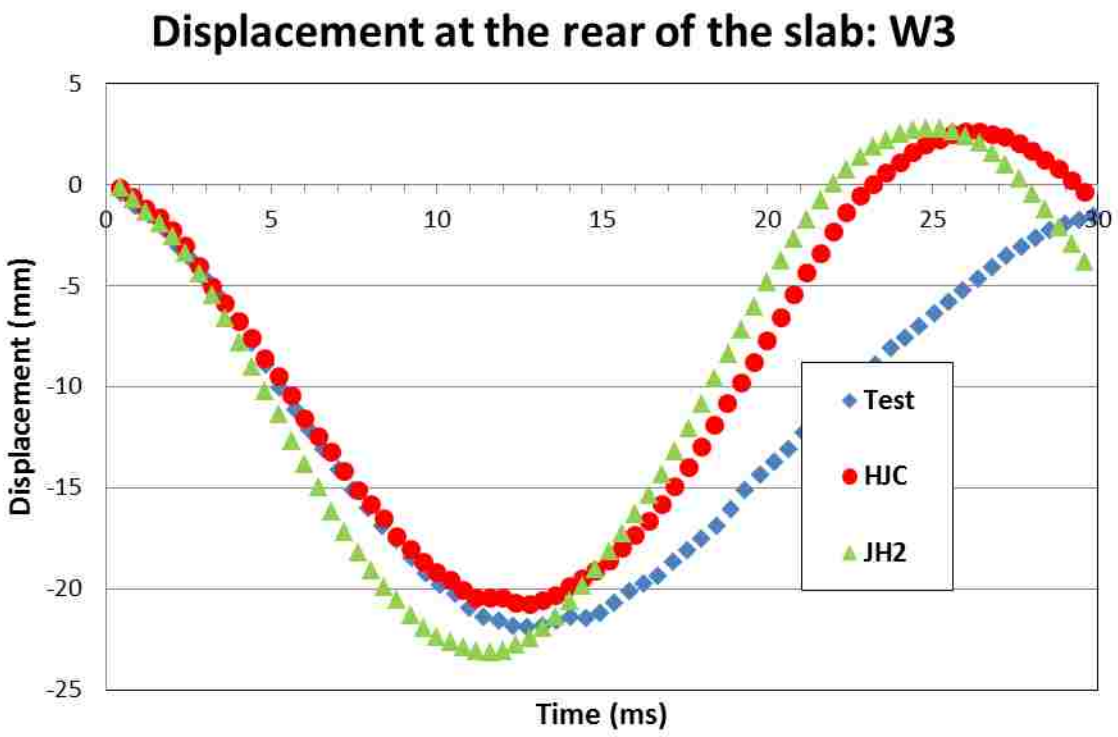

Figure 5.13: Displacement of location W3

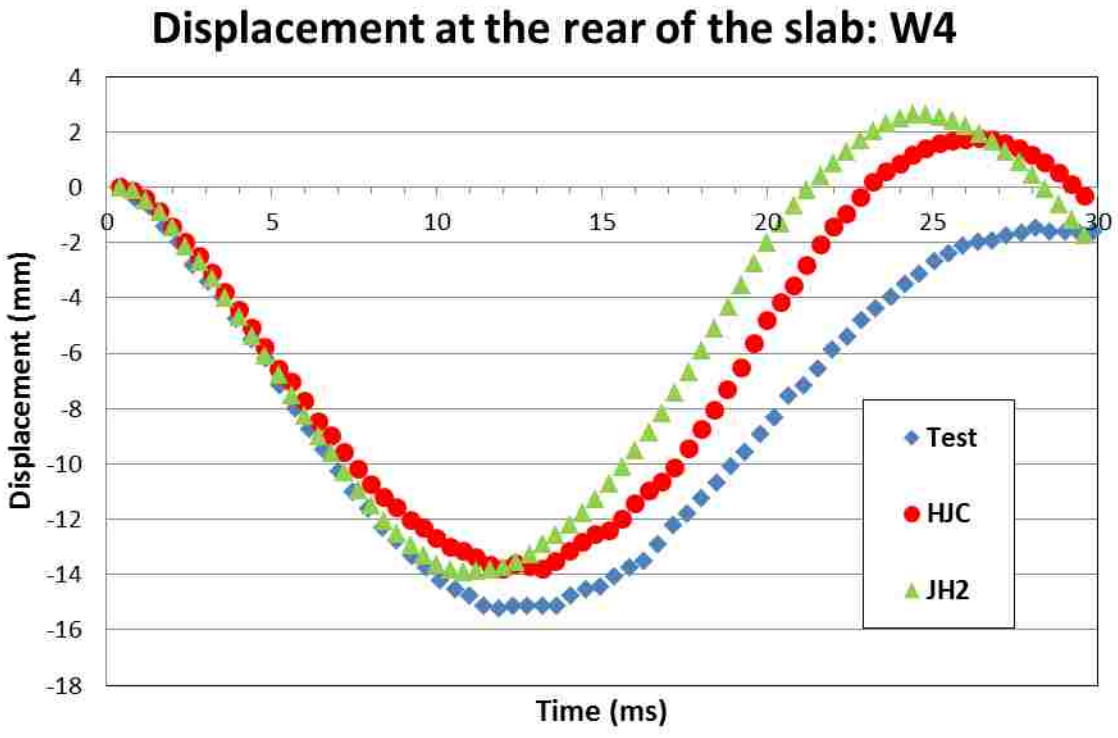

Figure 5.14: Displacement of location W4

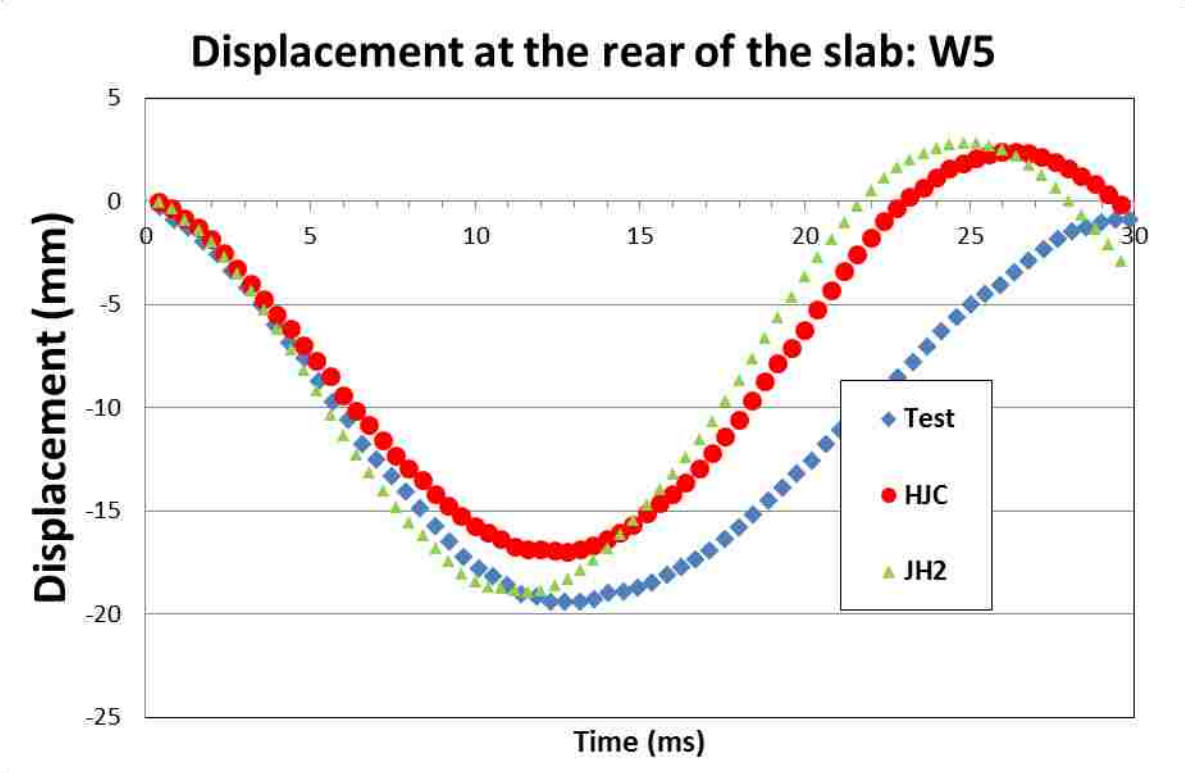

Figure 5.15: Displacement of location W5

The VTT Flexural numerical simulation, for both concrete material models, was able to approximate the general bending nature of the reinforced concrete slab. The offset of peak deflections and rapid post recovery are potentially byproducts of the simplified boundary condition and elastic recovery formulation of the material models. Another possibility for the slight discrepancy between the numerical simulations and the experimental data could be the lack of viscous damping in the simulations. Viscous damping can be implemented when the dynamic effects of a structure can't be completely quantified. In this case, the simply supported boundary condition is unrepresentative of the actual experiment which dissipates energy from the reinforced concrete slab into the supporting structure.

Figure 5.16 through Figure 5.22 displays the comparison of numerical and experimental data for various rebar axial strain locations.

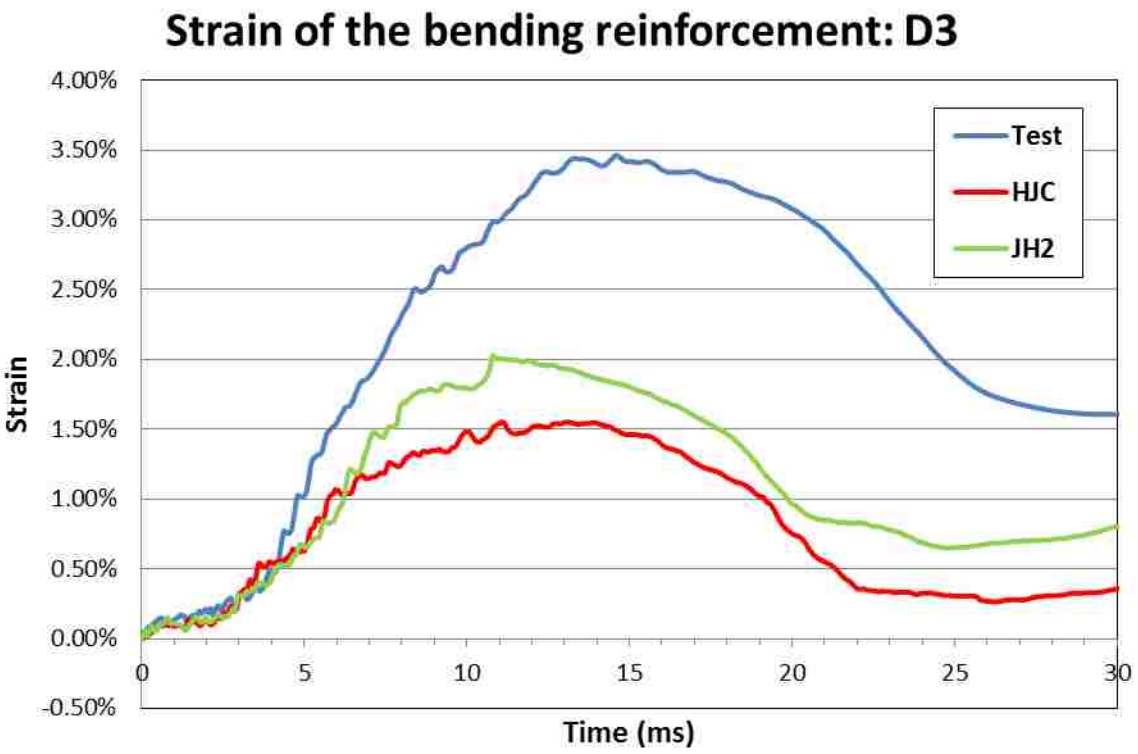

Figure 5.16: Rebar axial strain location D3

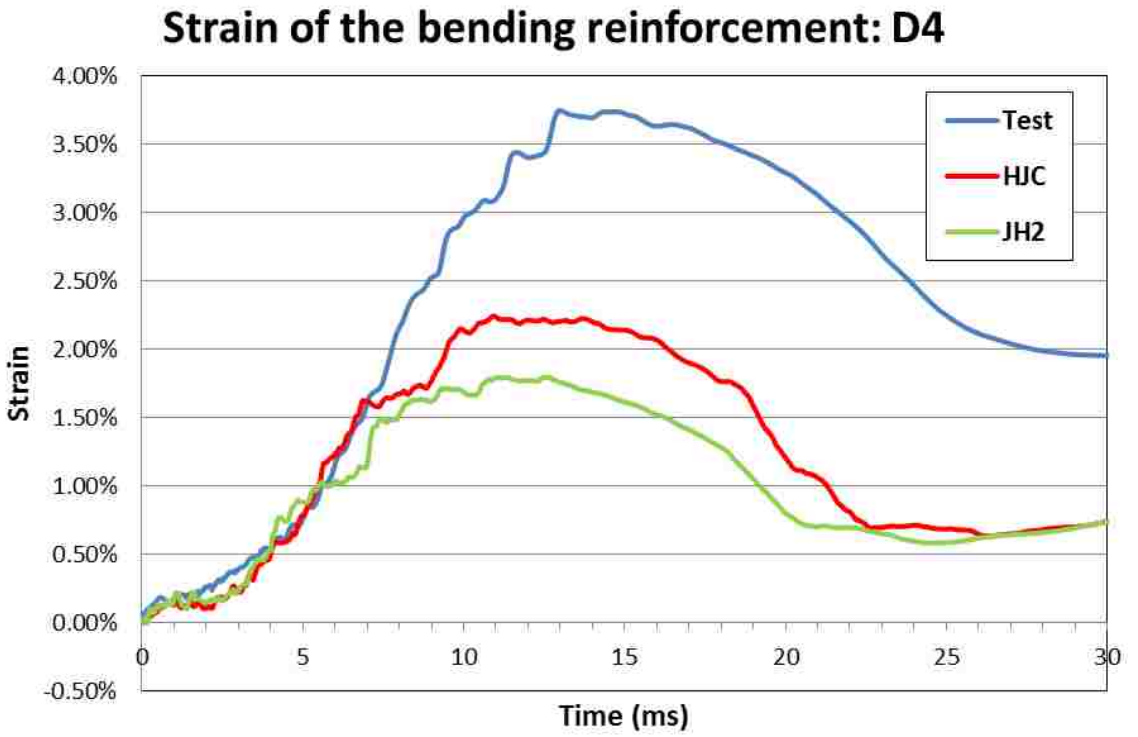

Figure 5.17: Rebar axial strain location D4

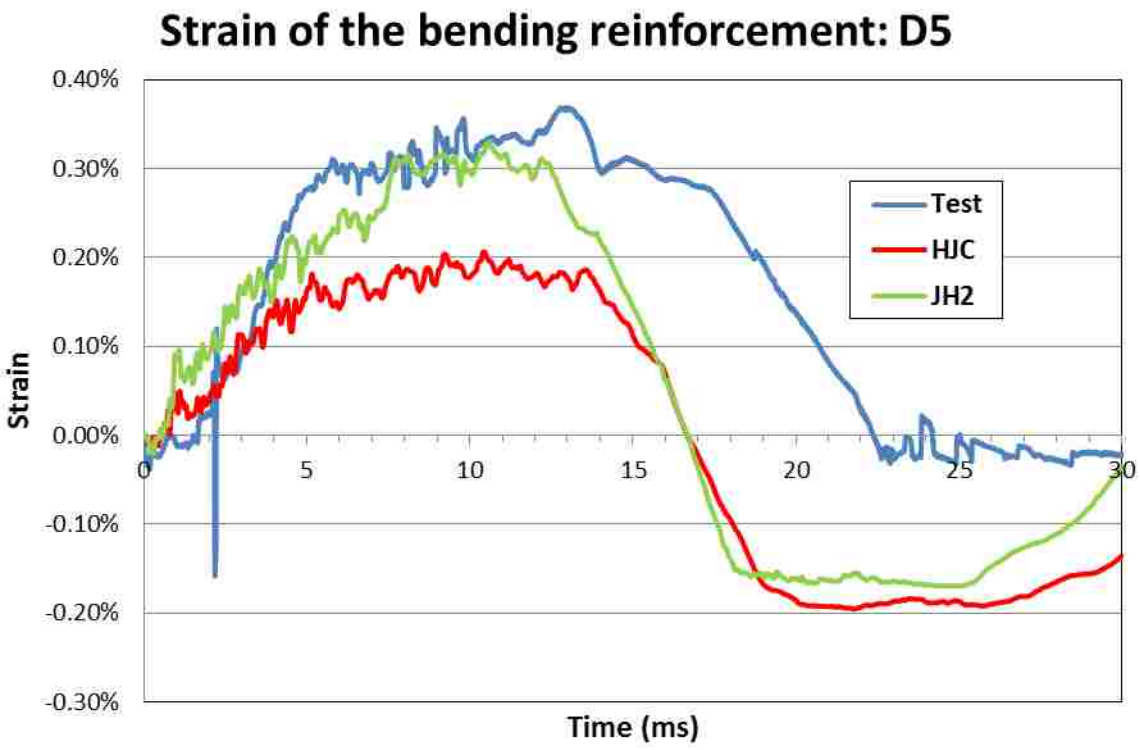

Figure 5.18: Rebar axial strain location D5

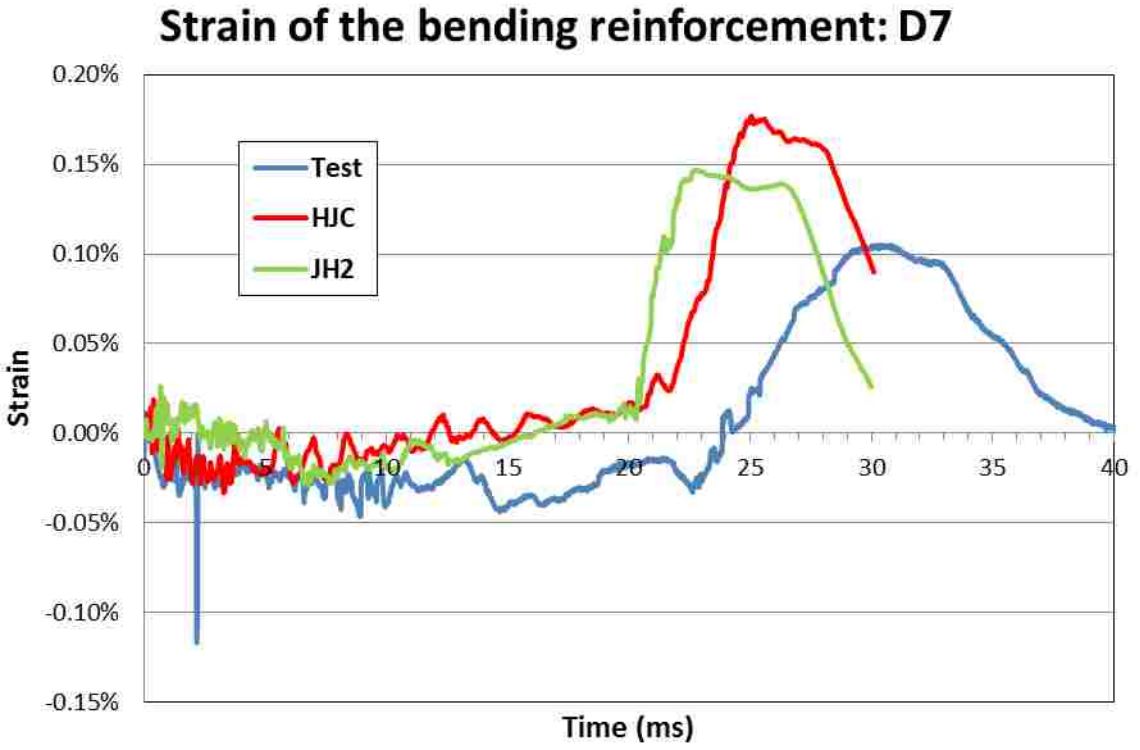

Figure 5.19: Rebar axial strain location D7

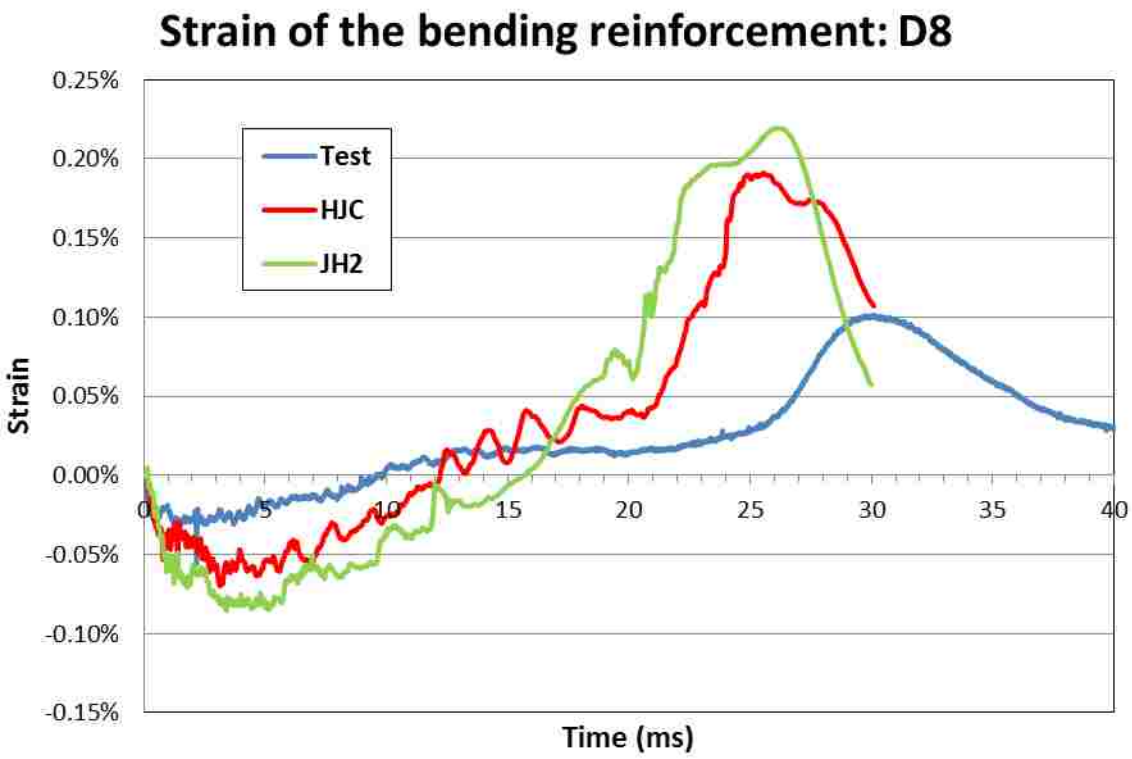

Figure 5.20: Rebar axial strain location D8

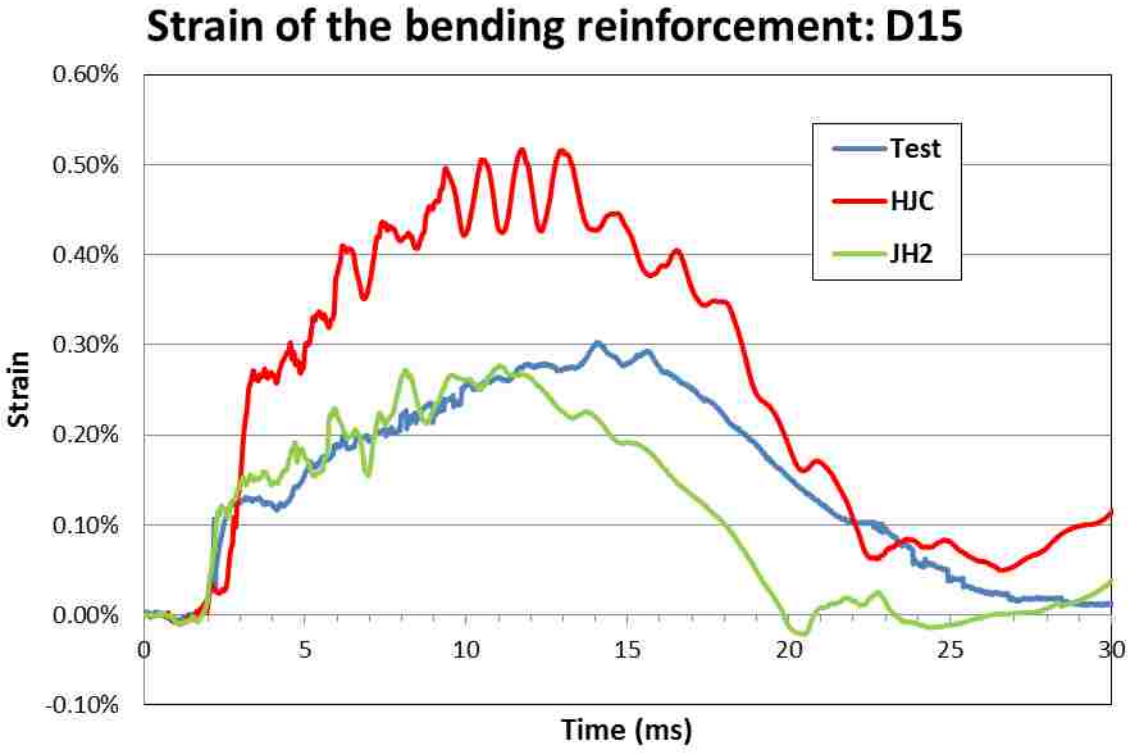

Figure 5.21: Rebar axial strain location D15

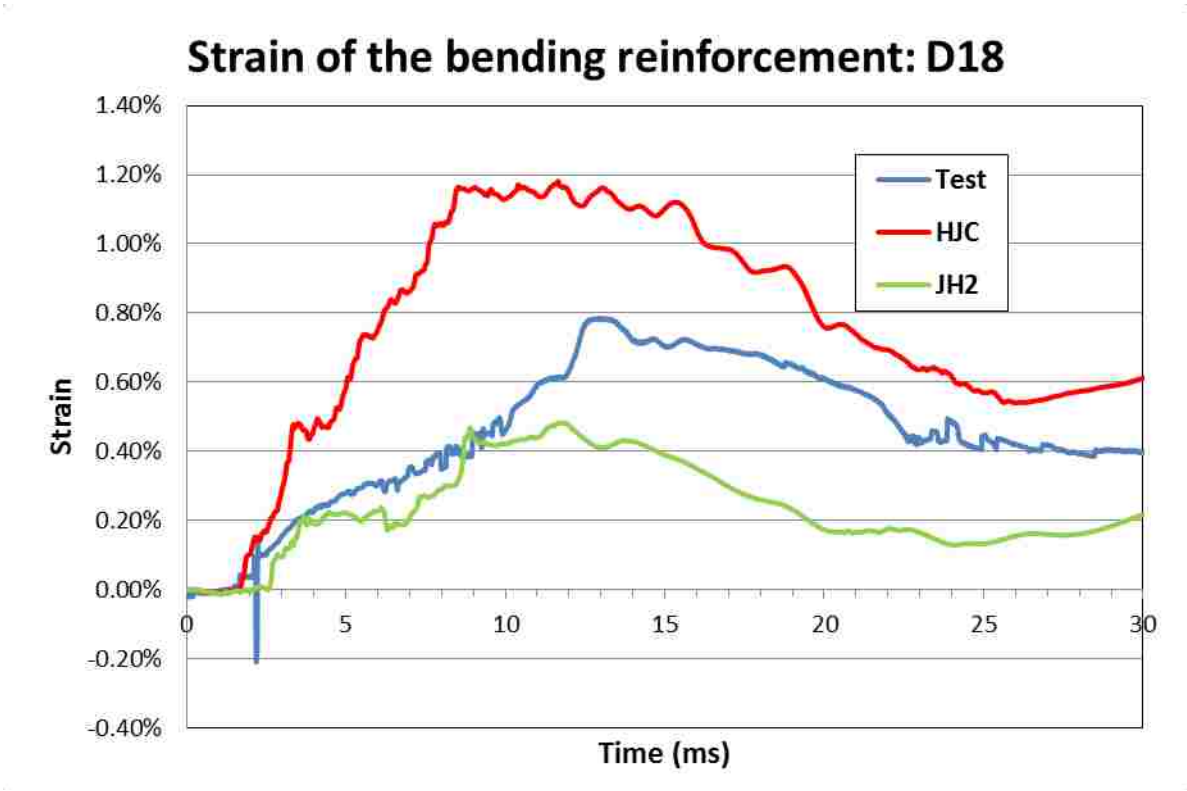

Figure 5.22: Rebar axial strain location D18

Similar to the displacements of the reinforced concrete simulation, the general behavior of the numerical data depicts a trend analogous of the experimental data. The strain periods of the reinforcement rebar for the numerical simulations are moderately in agreement with the experimental data. However, some divergence is present between the magnitude of peak strain for numerical and experimental data. This variance could be caused by several factors within the simulation. Inadequate coupling between the embedded and host elements could induce error as well as the bilinear elastic-plastic material models inability to capture ideal hardening behavior for the beams used to model the rebar reinforcement. The embedded modeling approach itself is an approximation since the nodes of the submodel (beams) are tied to the host elements (hexs) and the delamination process that typically occurs between the concrete and steel rebar, while bending, does not occur. Also

the quality of the strain test data could have been misleading since debonding of concrete from rebar could affect strain gage readings that are attached to the rebar.

5.3.3 Global Damage

For the VTT Flexural experiment, post impact damage on the reinforced concrete slab and missile was attained. The hollow missile was measured to quantify the crushed and undamaged regions of the missile post impact. Figure 5.23 provides a reference schematic for the measured regions on the missile.

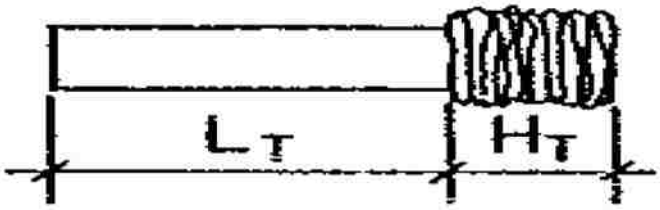

Figure 5.23: Post impact measured missile regions

Figure 5.24, Figure 5.25, and Figure 5.26 provide the final state of the 2 meter hollow steel tube for the experimental data, HJC based numerical simulation, and JH2 numerical simulation. Table 5.3 compares the measured regions for all three data sets.

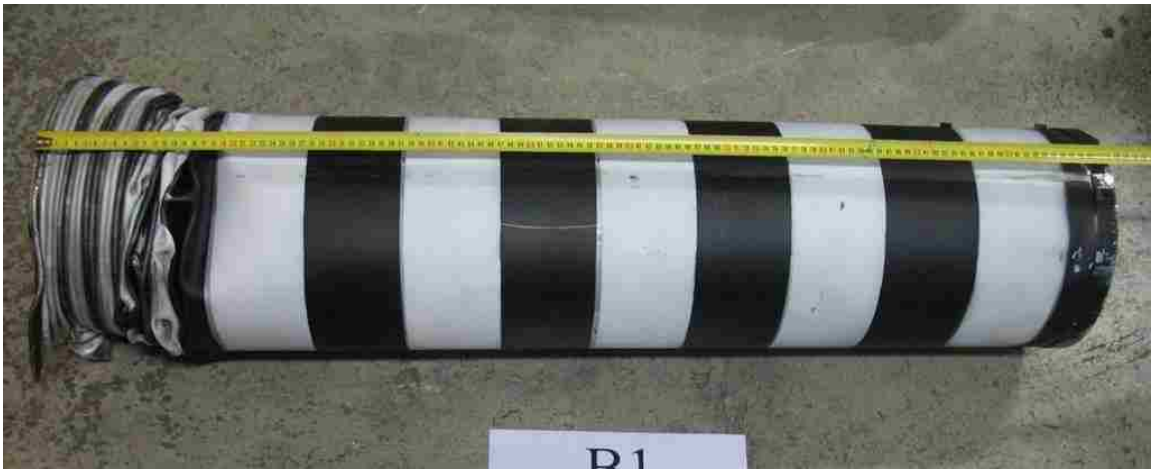

Figure 5.24: Deformed hollow missile from VTT experiment

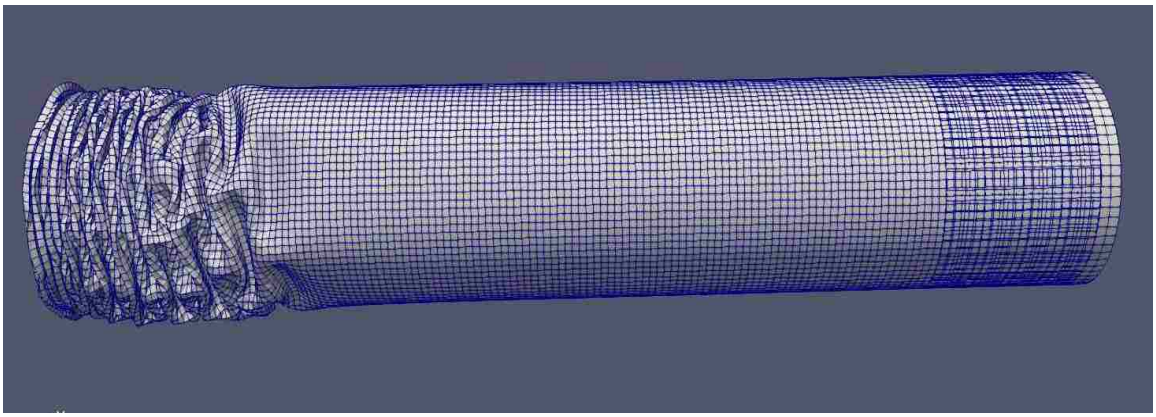

Figure 5.25: Deformed hollow missile from numerical simulation (HJC)

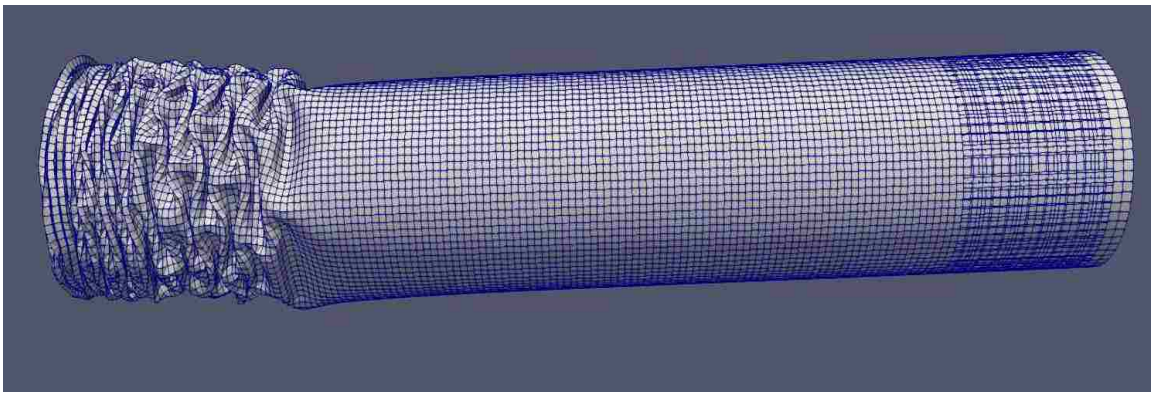

Figure 5.26: Deformed hollow missile from numerical simulation (JH2)

Table 5.3: Measured regions on damaged hollow missile

Data Set	$\boldsymbol{L_T}$ – intact (mm)	$\boldsymbol{H_T}$ – crushed (mm)
VTT Test	955	200
HJC (sim)	1005	312
JH2 (sim)	1003	340

The numerical simulations predicted accurate measurements for the non-crushed region of the hollow missile while over predicting the size of the crushed region. The miscalculation of the crushed region can be linked to the loading conditions applied. Upon further inspection, the VTT test missile buckles and forms neat folds for the majority of the crushed

region while the numerical models do not. This is common for thin tube metals undergoing compressive uniaxial deformation and can actually be seen on the impacting region of the numerical models. However, the majority of the crushed regions on the numerical models contain a different buckling mode observed in thin tube metals experiencing both compressive and torsional loads. Since shell elements with 5 integration points were used in the simulation and high distortions were present, shear locked elements could be the culprit for the strange buckling mode seen in the numerical models.

Along with the damaged missile, damage on the concrete slab was observed post impact. Figure 5.27 shows the damage the front surface of the slab received from the soft missile impact. Little to no damage was suffered by the front surface of the concrete structure excluding the site of impact where a visible blemish can be seen. The HJC material model captured a superior damage profile on the front surface versus the JH2 material model. Both material models however predicted excessive damage. Figure 5.28 and Figure 5.29 display concentric and lattice damage profiles on the front face produced by the HJC and JH2 models, respectively.

Figure 5.27: Concrete damage on front surface of VTT experiment

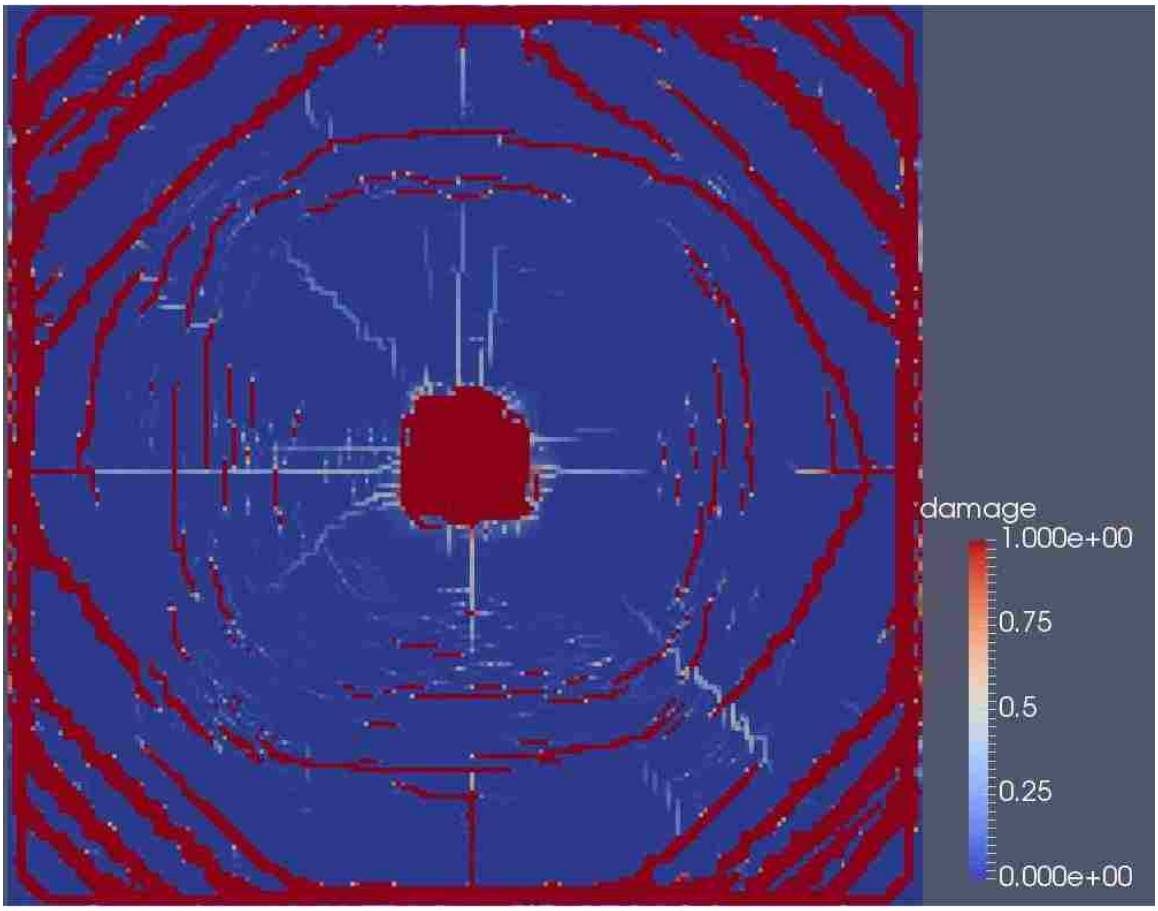

Figure 5.28: Concrete damage on front surface of numerical model (HJC)

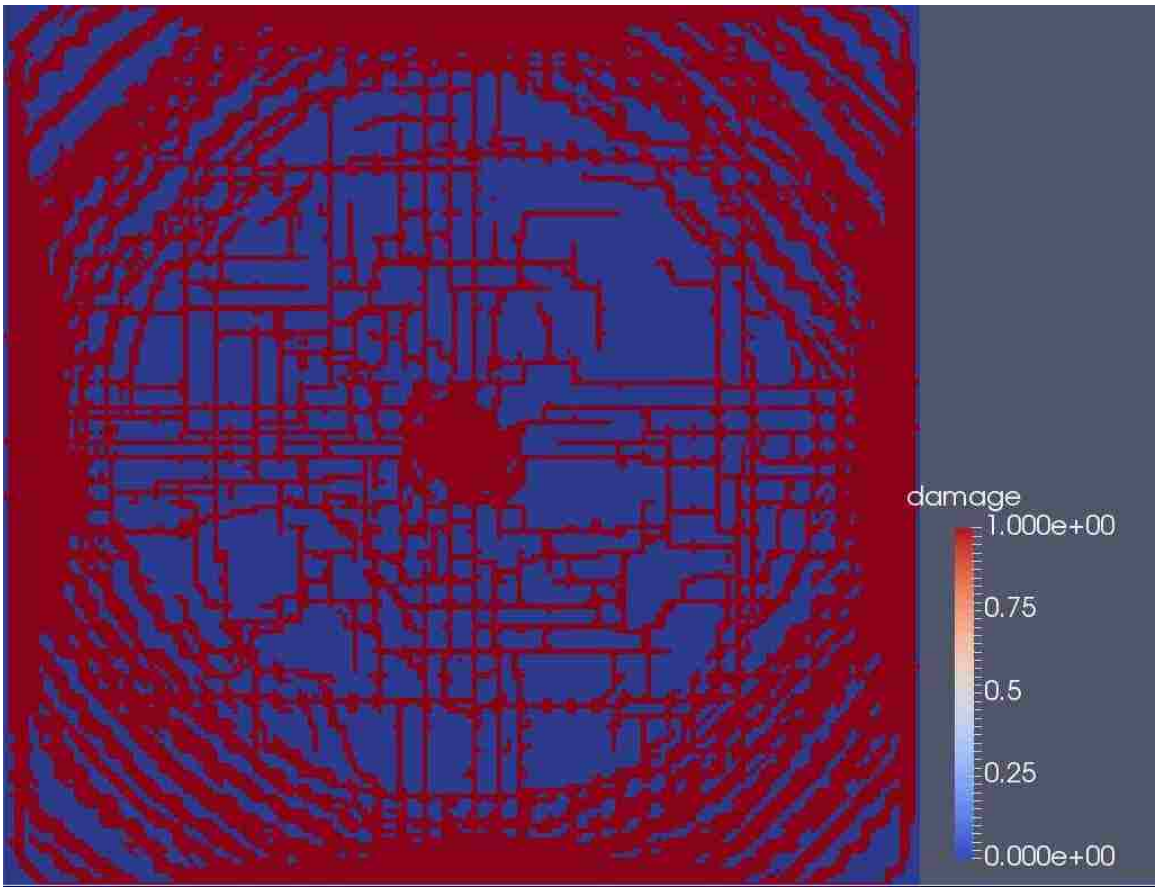

Figure 5.29: Concrete damage on front surface of numerical model (JH2)

The damage caused on the rear surface of the VTT test can be seen in Figure 5.30. Unlike the front surface of the concrete slab, the rear surface suffered more noticeable damage depicted by surface cracks. A circular patch of cracks on the center of the rear surface can be seen connected to diagonal cracks radiating outwards. Figure 5.31 and Figure 5.32 portray the damage profiles produced by the HJC and JH2 material model on the rear surface, respectively.

Figure 5.30: Concrete damage on rear surface of VTT experiment

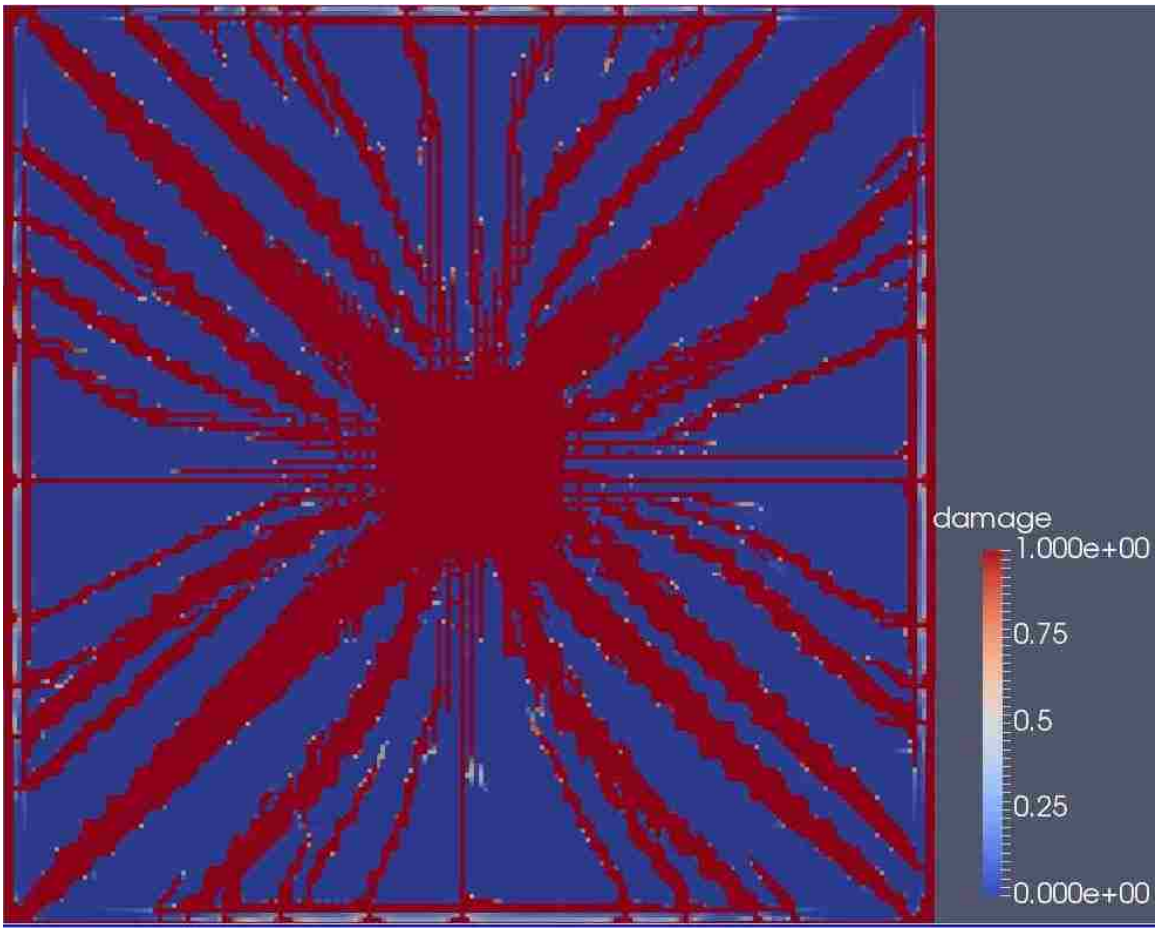

Figure 5.31: Concrete damage on rear surface of numerical model (HJC)

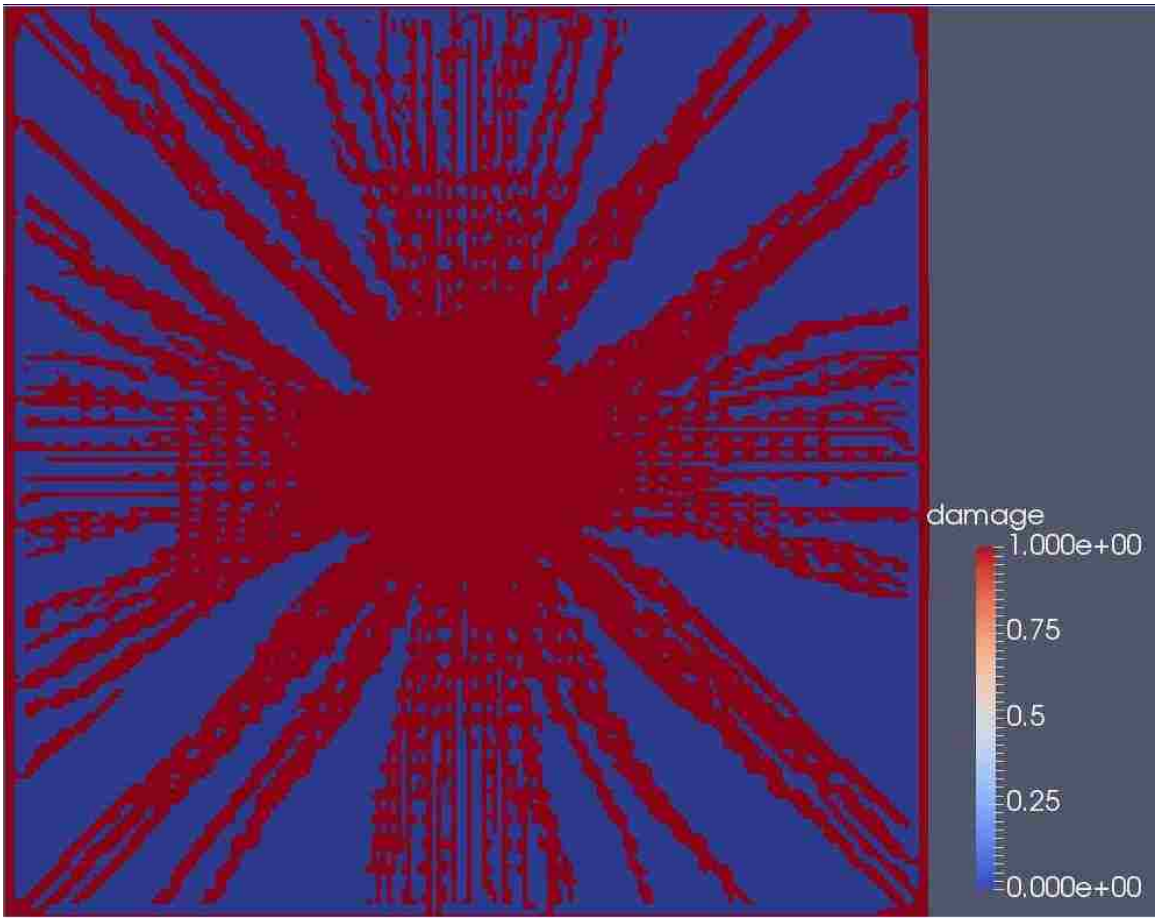

Figure 5.32: Concrete damage on rear surface of numerical model (JH2)

5.4 VTT Punching

The third step in the validation process of the material model was observing the localized damage produced by the solid missile impact. During the VTT Punching test, the solid missile perforated the concrete slab while leaving scabbed contours on both sides of the concrete slab. The mechanical drawings of the punching solid missile indicate low curvature on the impacting region of the missile. Consequently, a uniform hex mesh was not implemented because the geometry of hex elements could not capture the adequate geometry of the missile without producing inverted elements. For this reason, two different missiles were tested: a solely hex meshed missile with a flat impacting region and a mainly

hex meshed missile with a tet meshed impacting region. Figure 5.33 and Figure 5.34 display the numerical model solid missile using only hex elements, and the numerical model solid missile using hex and tet elements respectively.

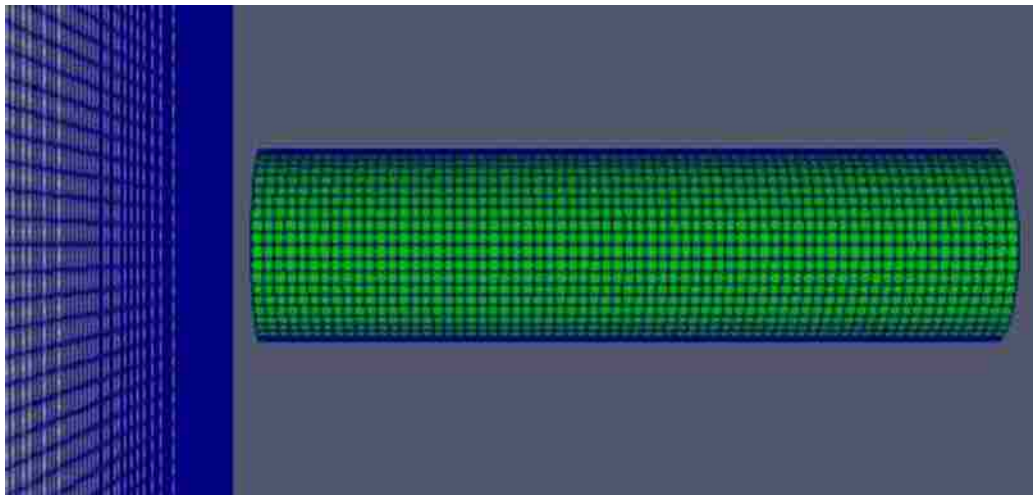

Figure 5.33: Hex element solid punching missile

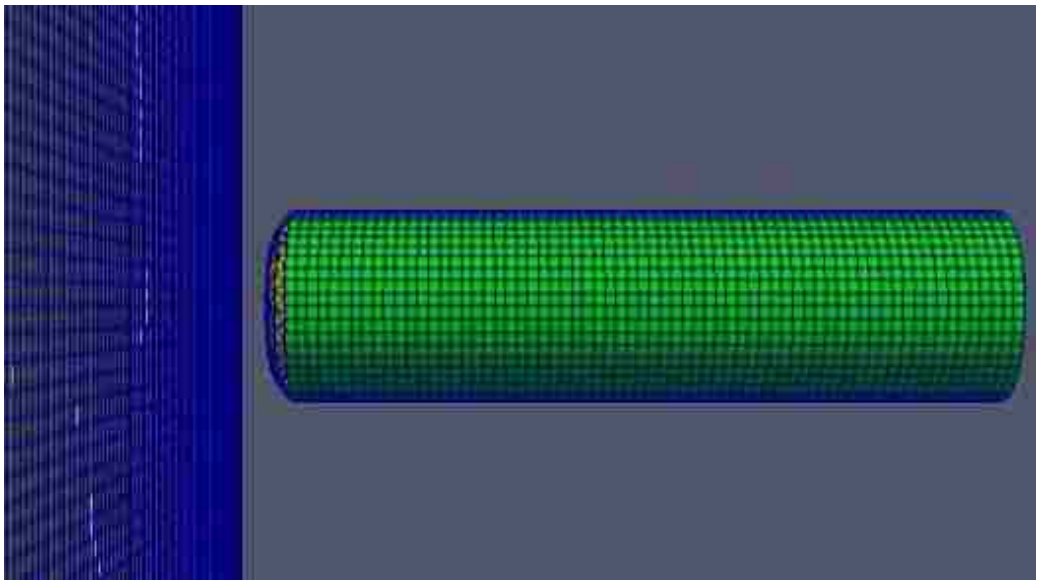

Figure 5.34: Hex and tet element solid punching missile

Figure 5.35, Figure 5.36 and Figure 5.37 display the post impact solid missile of the VTT Punching experiment, hex only numerical model and hex/tet numerical model respectively. The numerical models were ran with both constitutive concrete models and both models

produced similar missile distortions in localized areas around the steel/concrete interface of the missile along the sides.

Figure 5.35: VTT Punching solid missile post impact

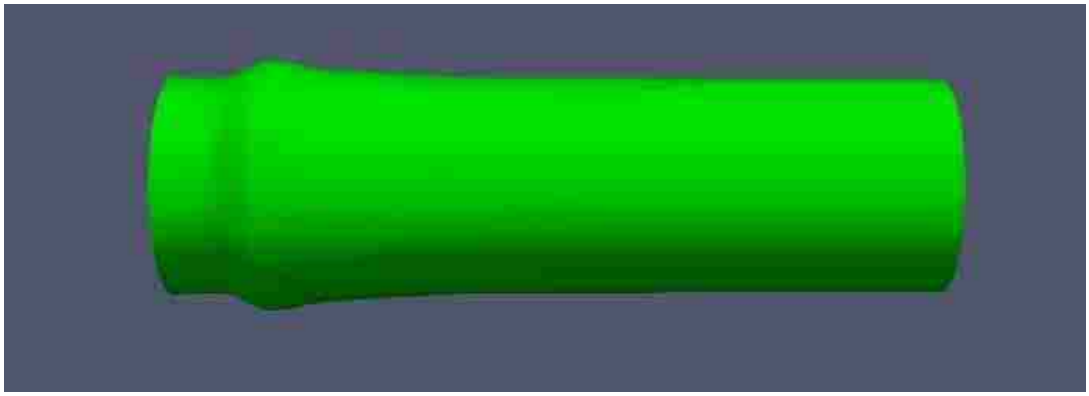

Figure 5.36: Hex solid missile numerical model post impact

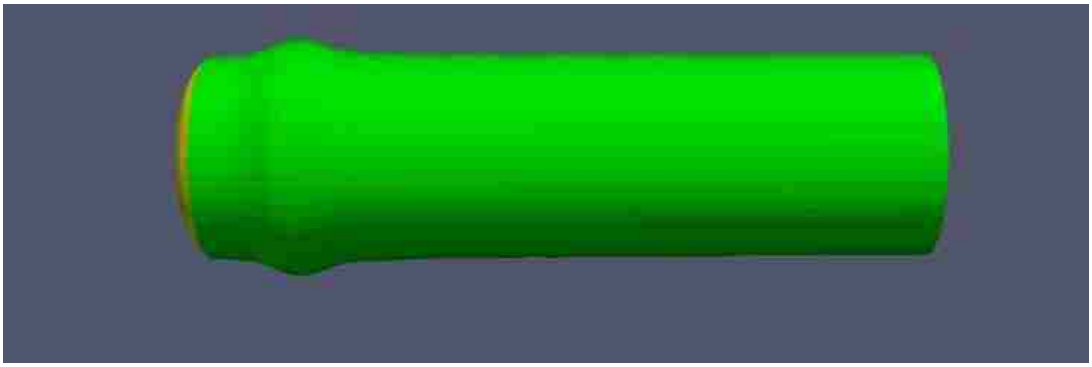

Figure 5.37: Hex and tet solid missile numerical model post impact

Since the geometrical differences between the solid missiles numerical models are relatively small, the imparted damage patterns the two models created on the thick concrete slab were considered indistinguishable from one another. Although the damage patterns produced on the concrete were similar, the hex an tet meshed missile was used in the final simulations because of its ability to capture the deformation of the solid missile better on the impacting face.

The biggest tribulation encountered in modeling the VTT Punching simulation was assigning adequate element death criteria. Unlike the VTT Flexural simulation, the VTT Punching simulation required fractured elements to be removed which is not truly representative of what occurs during testing. Once an element is deleted, everything associated with that element including its mass is deleted. The HJC and JH2 material models both contain a damage parameter which denotes a gradient fractured state from 0 (intact) to 1 (fully fractured) for an element. This parameter however, was unusable to determine element death because even though an element may be fully fractured, it can still carry a compressive load. This meant that areas where penetration or perforation did not occur, but where crack formation could be present, would be deleted. Since concrete is weakest in tension, an identical element death criteria was set for both punching simulations that were tensile strain dependent that was achieved through an iterative process. Figure 5.38, Figure 5.39, and Figure 5.40 depict the rear surface of the concrete slab for the VTT Punching test, HJC numerical simulation, and JH2 numerical simulation respectively.

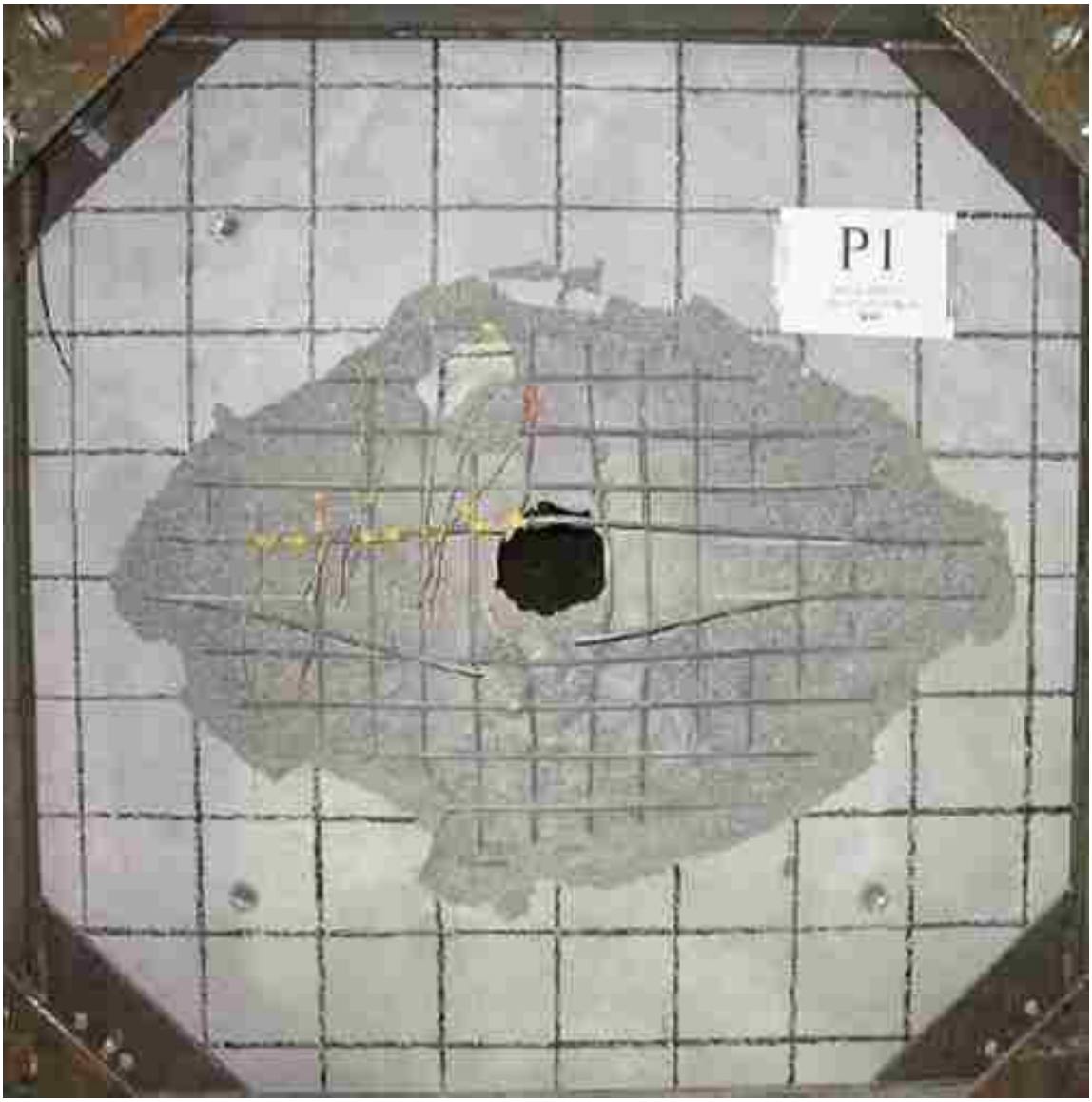

Figure 5.38: VTT Punching test post impact on rear surface

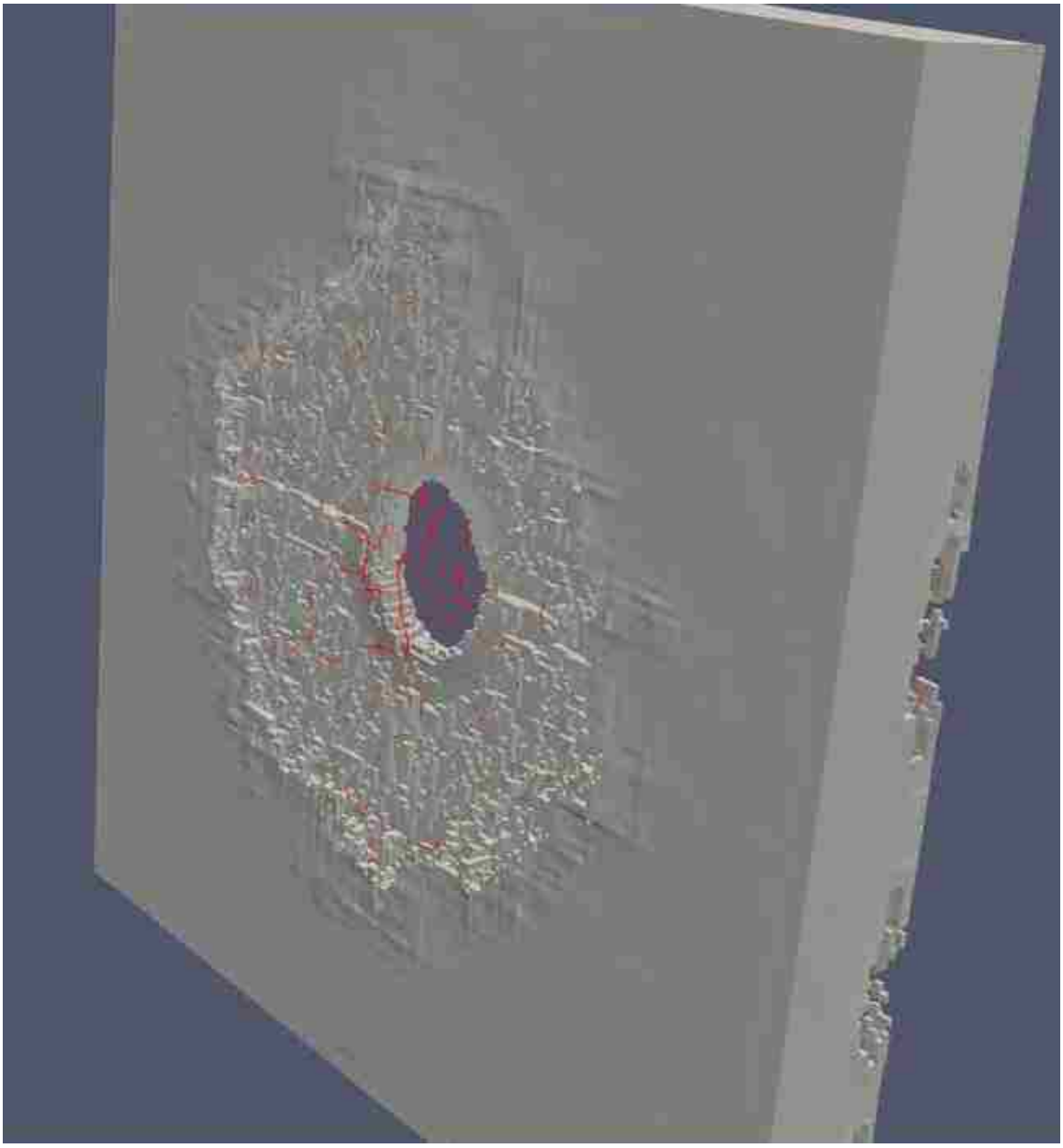

Figure 5.39: VTT Punching simulation post impact on rear surface (HJC)

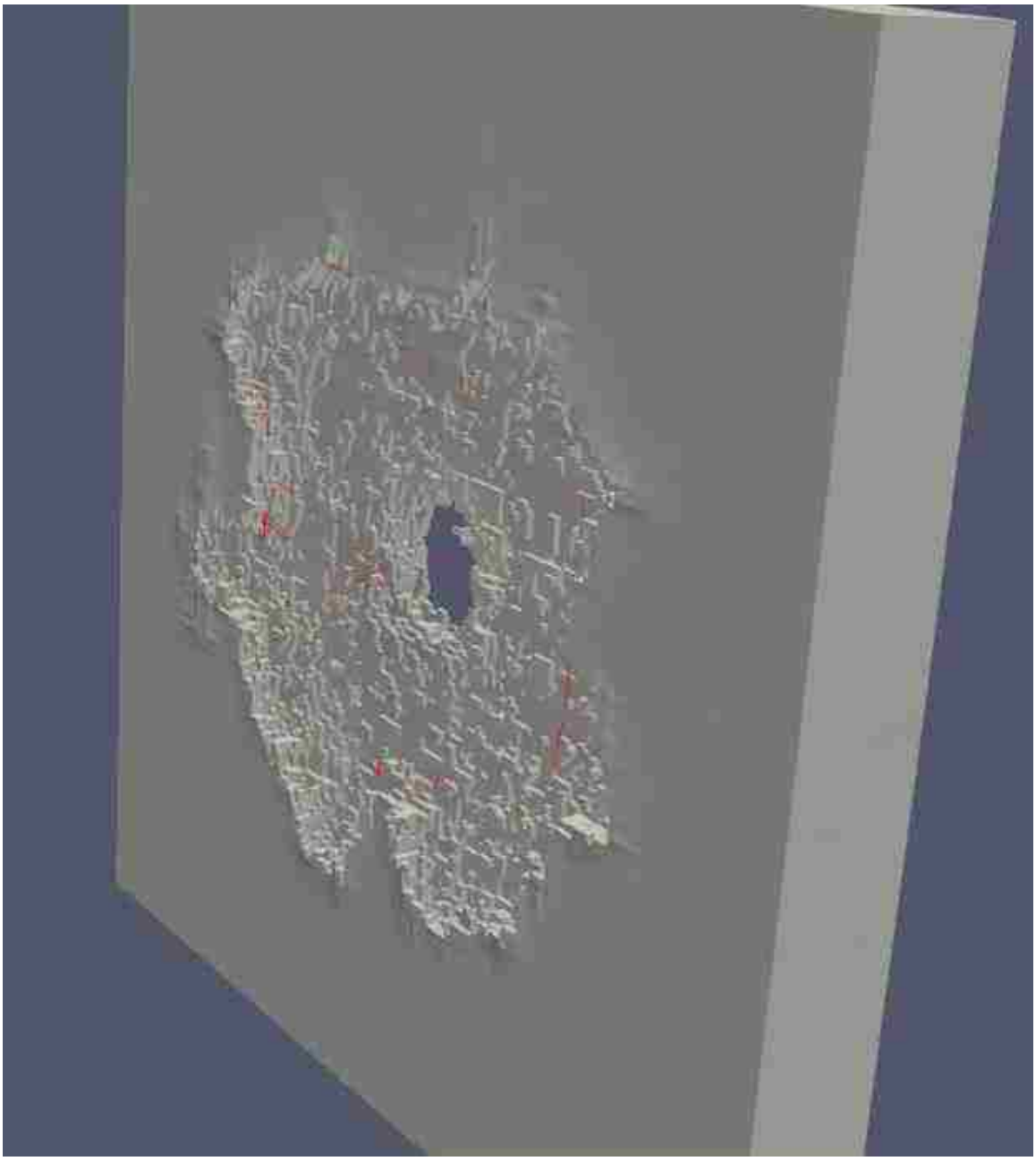

Figure 5.40: VTT Punching simulation post impact on rear surface (JH2)

For the numerical simulations, both material models produced unique scabbing patterns with different perforation radii using the same element death criteria. The HJC material model produced a larger perforated radius on the slab with a circular scabbing pattern while the JH2 material model produced a smaller perforated radius with a more square scabbing pattern. Both material models were able to reproduce the shear plug effects that join the

scabbed and perforated regions together. Neither model was able to capture the elliptical damage pattern from the original VTT Punching experiment. The elliptical pattern seen in the experiment could have been caused by the different rebar reinforcement placement as compared to the numerical models. In the numerical simulations, the rebar that travels longitudinally in two different directions (vertical and horizontal) was placed on the same plane where as in the experiment, an offset exists between the vertical and horizontal running rebar since they can't physically be placed in the same plane. Table 5.4 and Table 5.5 lists the final approximate scabbing and perforation areas produced in the experiment and numerical simulations.

Table 5.4: Scabbing area comparison

DATA SET	Scabbing Area (m^2)
VTT Test	~1.209
HJC	~1.418
JH2	~1.356

Table 5.5: Perforation area comparison

DATA SET	Area (m^2)
VTT Test	~.1018
HJC	~.2290
JH2	~.1412

5.5 IRIS Material Modeling Comparison

Lastly, the final validation process of the HJC and JH2 material models was conducted by comparing the results obtained from the VTT Flexural simulations to other material model results submitted to NEA for the IRIS Phase II program. Over 20 teams used a variety of different computational software, modeling techniques, and constitutive concrete models. All simulation results were submitted to the NEA and a generalized grading metric was used to compare different simulations submitted by different participating organizations. Table 5: Material Models used in IRIS Phase II lists some material models that were used, along with the HJC and JH2 material model used in this paper.

Table 5: Material Models used in IRIS Phase II

Designated Number	Material Model
1	ANACAP-U
2	Continuous Surface Cap Model
3	Winfrith Concrete Model
4	Hoshikuma et al.
5	Eurocode 2
6	RHT Concrete Model
7	Continuous Surface Cap Model (2)
8	Radioss/Ottosen
9	Drucker-Prager
10	Winfrith Concrete Model (2)
11 (this work)	Holmquist-Johnson-Cook Concrete (HJC)
12 (this work)	Johnson-Holmquist Ceramic (JH2)

Although many groups participated in the program, many used similar material models and modeling techniques. The previous table sheds light on the variety of material models used and how some material models can give you different results by changing the modeling approach. 1 through 10 were randomly picked results to compare to the HJC (11) and JH2 (12) material models. The first grading metric was the unconfined compression test and the strain at which compressive strength is achieved. Almost all material models achieved the compressive strength, however many were unsuccessful at achieving the strain at which compressive strength is achieved. Figure 5.41 and Figure 5.42 display the comparison between material models for compressive strength and uniaxial strain at peak strength respectively.

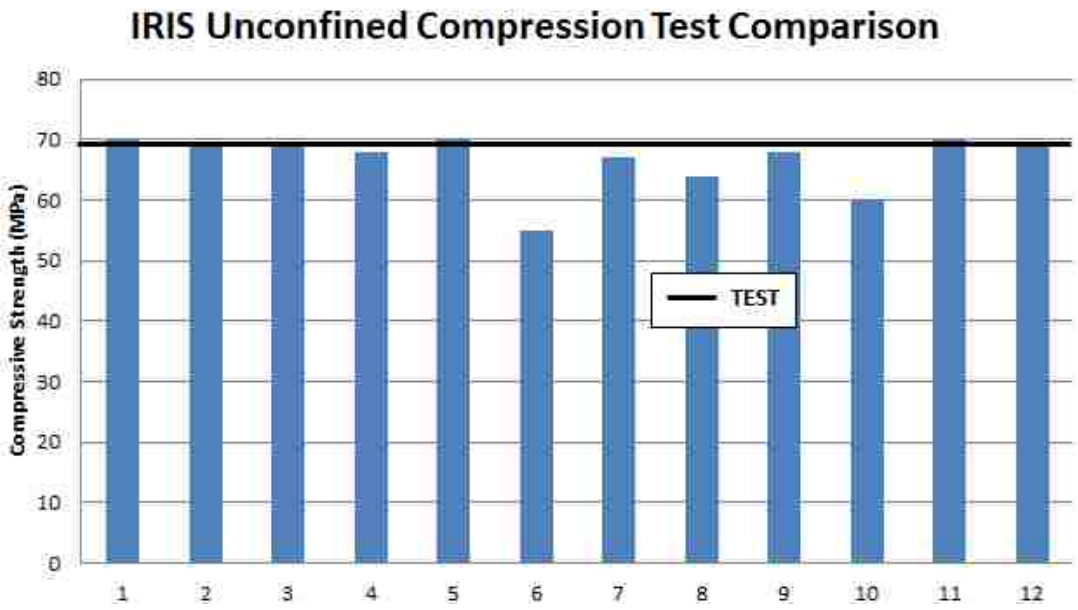

Figure 5.41: Material model unconfined compression test compressive strength comparison

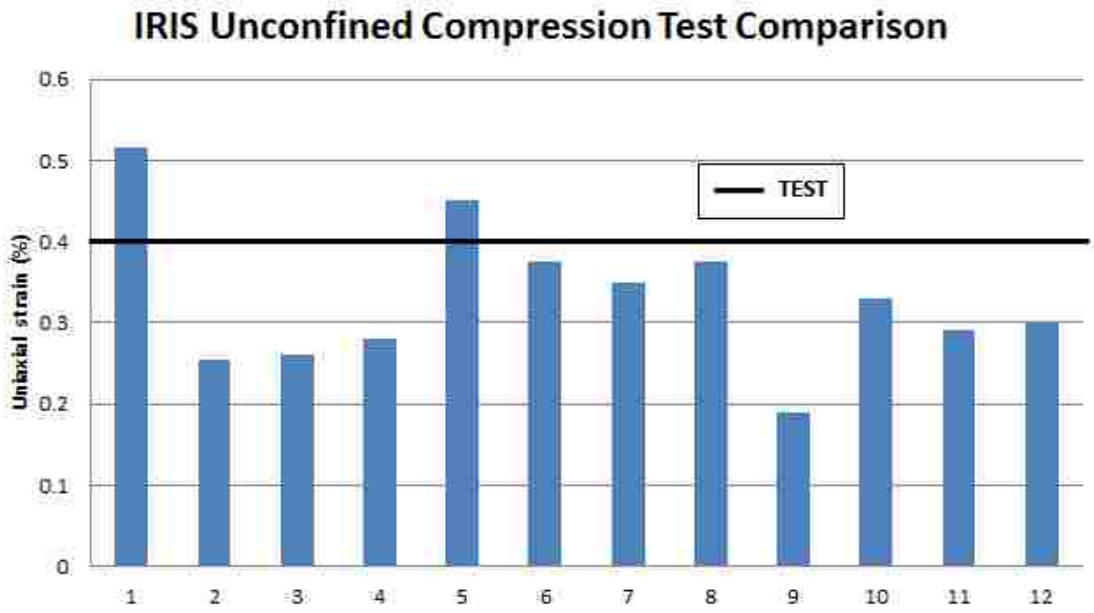

Figure 5.42: Material model unconfined compression test strain at peak compressive strength comparison

The second grading metric was the maximum and residual out-of-plane displacement achieved on the rear surface of the slab for the flexural simulation. Unlike the first grading metric, more disparity amongst results from the material models was seen. Figure 5.43 and Figure 5.44 display maximum and residual displacement comparisons respectively.

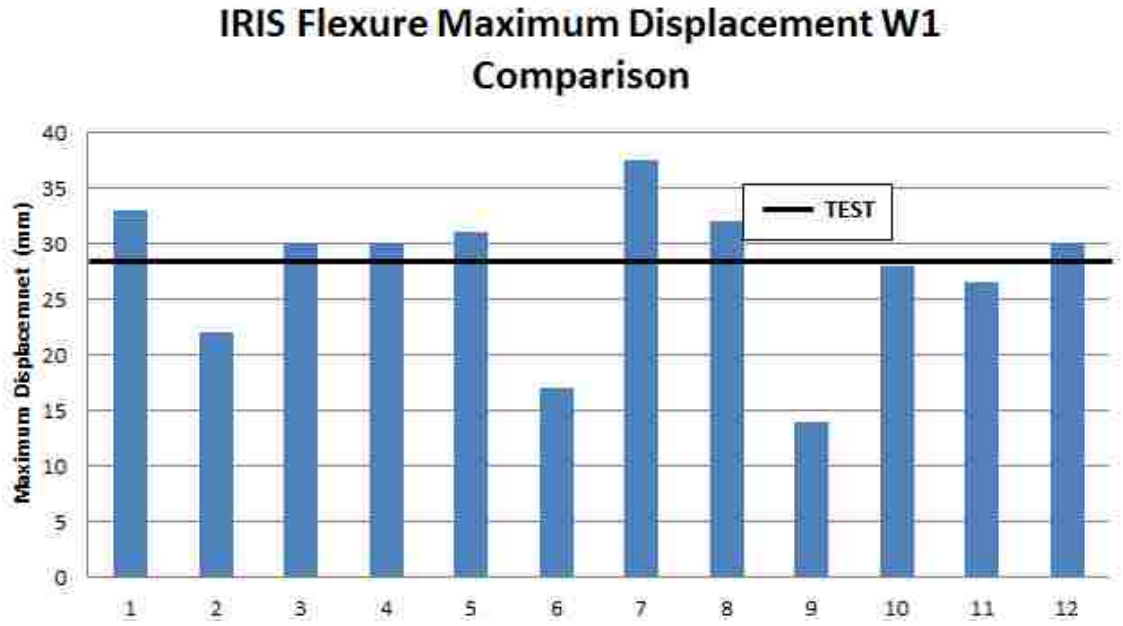

Figure 5.43: Material model comparison for maximum displacement on rear surface of slab

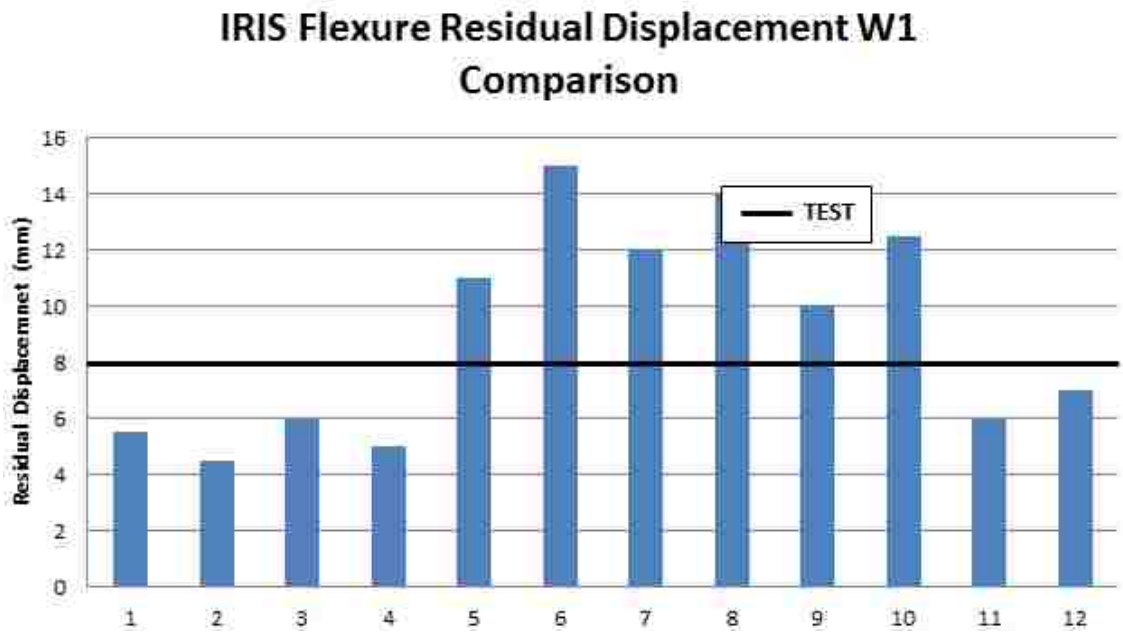

Figure 5.44: Material model comparison for residual displacement on rear surface of slab

The last grading metric was the bending strain for reinforcement D3. Unlike the previous grading metrics, most numerical simulations conducted under predicted the bending strain of the D3 reinforcement location. This implied that most numerical simulations conducted, with the varying material models, predicted an overly stiff flexural response of the impacted concrete slab. Figure 5.45 displays the bending strain comparison for various material models.

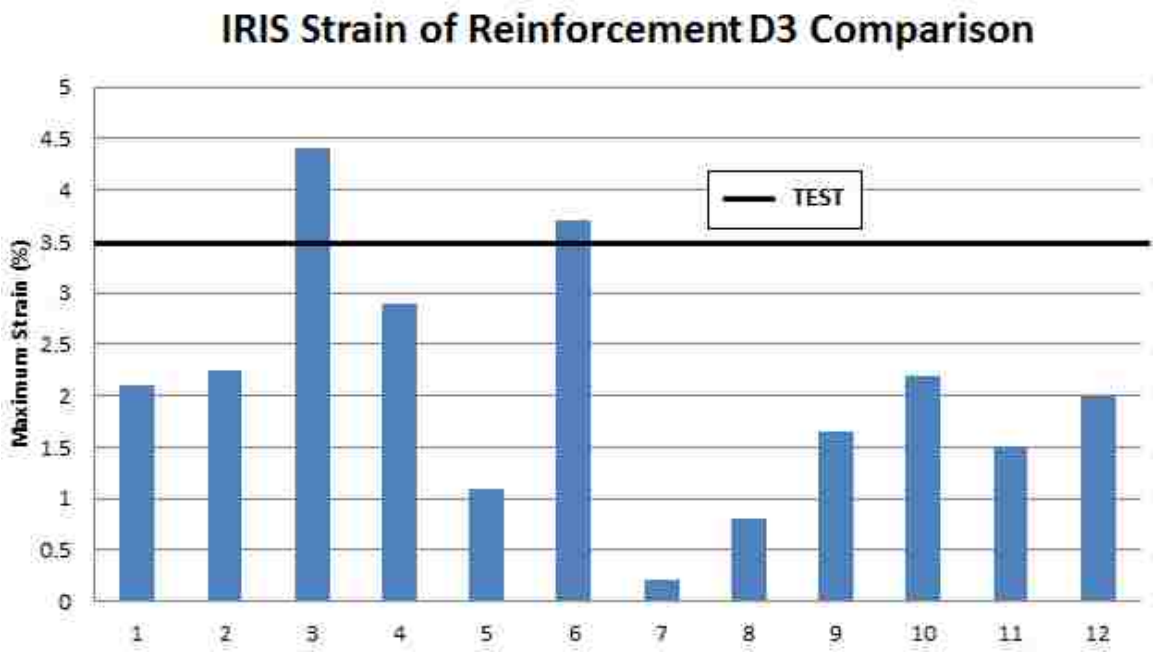

Figure 5.45: Material model comparison for bending strain D3

CHAPTER 6

CONCLUSION AND RECOMMENDATIONS

6.1 Conclusion

The increasing concern to acquire a numerical approach with the capability to quantity reinforced concrete damage subjected to impact loads has become more evident in the recent decades. This notion was driven heavily as the nuclear industry became more prominent. If an accurate modeling approach could be developed, running large scale simulations could help mitigate accident scenarios by providing design solutions to reinforced concrete structures, thus allowing them to withstand various impact loads. Many constitutive concrete models have thus been developed to replicate the complex mechanistic behavior of cementitious materials. The intricacy of many different material models has given rise to a wide spectrum of numerical approaches that could be taken to model concrete subjected to missile impacts. These various approaches all have different degrees of uncertainty, some more than others, when compared to experimental test data. The literature review touched on the dynamic environment involved in simulating concrete impacts and the need to further improve and develop the precision of numerical approaches to better quantify the phenomenological response in such an event.

The primary objective of this study was achieved through the development of a FEM to simulate the VTT-IRSN Flexural/Punching experiments orchestrated by the NEA and CSNI within SIERRA Solid Mechanics. Two similar material models, the Holmquist-Johnson-Cook (HJC) concrete and Johnson-Holmquist II (JH2) ceramic model, were compared and evaluated in their ability to capture the flexural response of a reinforced

concrete slab impacted by a hollow steel missile and localized damage patterns from a solid steel covered concrete missile. The HJC and JH2 were able to capture the quasi-static cylinder compression test with relative ease. Both material models showed increasing strength with increasing confinement pressure; however the HJC displayed a greater ability to capture the cylindrical compression tests because of its bilinear region for pressure-volumetric strain dependence which provides better crushing behavior along with a permanent volumetric deformation. For the VTT Flexural simulation both material models provided similar displacements of the rear surface of the slab and similar strain measurements of the embedded rebar. The main difference between the two material models for the VTT Flexural simulation was the damage pattern created on the impacted surface of the concrete slab. The HJC material model produced a concentric damage pattern while the JH2 material model produced a cross-hatch damage pattern. Although surface cracks were not present on the front face of the concrete slab post impact in the VTT Flexural experiment, both material models could represent present underlying damage that is not cosmetic. For the VTT Punching experiment, using the same tensile strain based material death criteria for the concrete, both material models yielded similar yet different results. The HJC material model produced a larger circular scabbed region on the rear surface with a larger perforated hole while the JH2 material model produced a slightly smaller square scabbed region with a smaller perforated hole. When compared to other constitutive concrete models and codes used in the IRIS Phase II, both the HJC and JH2 material models are on par or better than some of the simulations submitted to the NEA and CSNI.

As a final conclusion, both the HJC and JH2 were able to model a non-homogenous material with great complexities when considering its plastic and fracture behavior. This study concludes that the two material models are highly suitable in capturing the mechanistic behavior of reinforced concrete impacted by missiles with some degree of uncertainty. For this reason, more studies must still be conducted to further investigate modeling approaches and develop better constitutive concrete models that are more precise in determining flexural and damage responses.

6.2 Recommendations

The modelling approach taken in this thesis focused on acquiring and using the most common techniques, element type, and integration schemes/points that work best for dynamic impact simulations. It is recommended that in order to fully investigate a material model, different modeling techniques, element types, and integration schemes/points should be used to make a comparison.

REFERENCES

ACI 318 Committee *Building Code Requirements for Reinforced Concrete (ACI 318-77)*. Detroit, MI: American Concrete Institute, 1982. Print.

ACI 349 Committee. *Code Requirements for Nuclear Safety Related Concrete Structures (ACI 349-01) and Commentary (ACOI 349R-01): An ACI Standard*. Farmington Hills, MI: American Concrete Institute, 2001. Print.

Adeli, H., and A.m. Amin. "Local effects of impactors on concrete structures." *Nuclear Engineering and Design* 88.3 (1985): 301-17.

Alexander, K. M., and J. Wardlaw. "Dependence of Cement-Aggregate Bond-Strength on Size of Aggregate." *Nature* 187.4733 (1960): 230-31.

Ancon. "All Ancon Building Products Catalogues and Technical Brochures." *All Ancon Building Products Catalogues and Technical Brochures - PDF Catalogues | Documentation | Brochures*. N.p., n.d. Web. 03 June 2017.

Bari, M. "A finite element study of shell and solid element study of shell and solid element performance in crash-box simulations." Thesis, presented to University West in Sweden in partial fulfillment of the requirements for the degree of Bachelors of Science. (2015).

Bensted, J. "Hydration of Portland Cement." *Advances in Cement Technology* (1983): 307-47. Web.

Chelapati C.V., Kennedy R. P. "Wall IB. Probabilistic assessment of hazard for nuclear structures." *Nuclear Engineering and Design* (1972): 19:333-64.

Gazonas, G. A., "Implementation of the Johnson-Holmquist II (JH-2) Constitutive Model into DYNA3D." *Army Research Laboratory* ARL-TR-2699 (2002).

Gupta, Y.m., and L. Seaman. "Local response of reinforced concrete to missile impacts." *Nuclear Engineering and Design* 45.2 (1978): 507-14.

Gu, X., Xianyu, J., Yong, Z. "Basic Principles of Concrete structures." *Springer* (2016)

Hughes, G. "Hard missile impact on reinforced concrete." *Nuclear Engineering and Design* 77.1 (1984): 23-35.

Holmquist, T. J.; Johnson, G. R.; Cook, W. H. A Computational Constitutive Model For Concrete Subjected To Large Strains, High Strain Rates, and High Pressures. *Intl Symp on Ballistics* 1993, 14, 591–600.

Johnson, G. R., Holmquist, T. J., "A computational constitutive model for brittle materials subjected to large strains, high strain rates and high pressures", *Shock-wave and High-strain Rate Phenomena in Materials*, (1992): 1075-1081.

Johnson, G. R., and T. J. Holmquist. "An Improved Computational Constitutive Model for Brittle Materials." *High Pressure Science and Technology*, New York: AIP Press, 1993.

Jones, Denny A. (1996). *Principles and Prevention of Corrosion*, Second Edition, Prentice Hall, Upper Saddle River, New Jersey, 572 pp.

Kennedy, R. P. "A review of procedures for the analysis and design of concrete structures to resist missile impact effects." *Nuclear Engineering and Design* 37.2 (1976): 183-203.

Kennedy RP. "Effects of an aircraft crash into a concrete reactor containment building." Anaheim, CA: *Holmes & Narver Inc.*; (1966).

Kojima, Isao. "An experimental study on local behavior of reinforced concrete slabs to missile impact." *Nuclear Engineering and Design* 130.2 (1991): 121-32.

Lamond, Joseph F. *Significance of tests and properties of concrete and concrete-making materials*. West Conshohocken, PA: ASTM, 2006. Print.

Li, Q.m., S.r. Reid, H.m. Wen, and A.r. Telford. "Local impact effects of hard missiles on concrete targets." *International Journal of Impact Engineering* 32.1-4 (2005): 224-84.

Martin, Oliver, Vincent Centro, and Thierry Schwoertzig. "Finite element analysis on the Meppen-II-4 Slab Test." *Nuclear Engineering and Design* 247 (2012): 1-10.

Meyer, C. S., "Development of Geomaterial Parameters for Numerical Simulations Using the Holmquist-Johnson-Cook Constitutive Model for Concrete." *Army Research Laboratory* ARL-TR-5556 (2011).

Moftah, S. O., Wriggers, P. "Mesoscale models for concrete: Homogenisation and damage behavior." *Finite Elements in Analysis and Design* 42-7 (2006): 623-636.

Nordendale, N. A., "Modeling and Simulating of Brittle Armors Under Impact and Blast Effects." Dissertation, presented to Vanderbilt University in Tennessee in partial fulfillment of the requirements for the degree of Doctor of Philosophy. (2013).

OECD-NEA. "Improving Robustness Assesment Methodologies for Structures Impacted by Missiles (IRIS_2012)." NEA/CSNI/R(2014)5 (2014).

Panasyuk, V.v., V.i. Marukha, and V.p. Sylovanyuk. "General Characteristics of Concretes and Reinforced Concretes." *Injection Technologies for the Repair of Damaged Concrete Structures* (2013): 11-34.

Riedel, Werner, Markus Nöldgen, Elmar Straßburger, Klaus Thoma, and Ekkehard Fehling. "Local damage to Ultra High Performance Concrete structures caused by an impact of aircraft engine missiles." *Nuclear Engineering and Design* 240.10 (2010): 2633-642.

Salas, M. D., “The Curious Events Leading to the Theory of Shock Waves.” *17th Shock Interaction Symposium* (2006).

Sanji, A. J., “Reinforced Concrete Structures Under Impact Loads.” Dissertation, presented to Heriot-Watt University in Scotland in partial fulfillment of the requirements for the degree of Doctor of Philosophy. (2011).

Sawamoto, Yoshikazu, Haruji Tsubota, Yoshiyuki Kasai, Norihide Koshika, and Hiroshi Morikawa. "Analytical studies on local damage to reinforced concrete structures under impact loading by discrete element method." *Nuclear Engineering and Design* 179.2 (1998): 157-77

Shishkin AA, Fizicheskaya khimiya kontaktnoy zony betonov ‘Physical chemistry of contact zone in concretes”. Mineral, Krivoy Rog (2001)

SIERRA Solid Mechanics Team. “Sierra/SolidMechanics 4.22 User’s Guide.”SANDIA REPORT SAND2011-7597 Unlimited Release (2011)

Sjaardama, G., Benzley, S., Perry, E., Merkley, K., Clark, B., “A Comparison of All Hexagonal and All Tetrahedral Finite Element Meshes for Elastic and Elasto-plastic Analysis.” 4th *International Meshing Roundtable*, Sandia National Laboratories (1995): 179-191

Stephenson, Alan E., George E. Sliter, and Edwin G. Burdette. "Full-scale tornado-missile impact tests." *Nuclear Engineering and Design* 46.1 (1978): 123-43

Wriggers, P., and M. Hain. "Micro-Meso-Macro Modelling of Composite Materials." *III European Conference on Computational Mechanics* (2007): 37

Zukas, J. “Introduction to Hydrocodes.” Elsevier (2004)